RADC-TR-77-142
Scientific Report
January 1977

STUDY OF THE PHYSICS OF INSULATING FILMS AS RELATED TO THE RELIABILITY OF METAL-OXIDE SEMICONDUCTOR (MOS) DEVICES

IBM T. J. WATSON RESEARCH CENTER
YORKTOWN HEIGHTS NY 10598

Approved for public release, distribution unlimited.

Sponsored by the Defense Advanced Research Projects Agency (DoD) DARPA Order No. 2180

ROME AIR DEVELOPMENT CENTER
AIR FORCE SYSTEMS COMMAND
GRIFFISS AIR FORCE BASE, NEW YORK 13441

DARPA Order No. 2180

Program Code No. 7010

Contractor: IBM Corporation

Effective Date of Contract:
17 May 1976

Contract No. F19628-76-C-0249

Principal Investigator
Dr. D. R. Young

RADC/ETS Project Scientist
Dr. John C. Garth, Tel. 617-861-2360

Contract Expiration Date:
16 May 1978

This report has been reviewed by the RADC Information Office (OI) and is releasable to the National Technical Information Service (NTIS). At NTIS it will be releasable to the General Public, including foreign nations.

This technical report has been reviewed and is approved.

John C. Garth

JOHN C. GARTH

UNCLASSIFIED

SECURITY CLASSIFICATION OF THIS PAGE (When Data Entered)

REPORT DOCUMENTATION PAGE

READ INSTRUCTIONS BEFORE COMPLETING FORM

1. REPORT NUMBER: RADC-TR-77-142
2. GOVT ACCESSION NO:
3. RECIPIENT'S CATALOG NUMBER:

4. TITLE (and Subtitle): Study of the Physics of Insulating Films as RElated to the Reliability of Metal-Oxide-Semiconductor (MOS) Devices.

5. TYPE OF REPORT & PERIOD COVERED: Semi-Annual Technical Report for period 5/17/76-11/16/76

6. PERFORMING ORG. REPORT NUMBER: Scientific Report #1

7. AUTHOR(s): T./DiStefano, D.R./Young, D.J./Dimaria, J.M.Aitken Z.A.Weinberg, K.Pan, W.R.Hunter, C.M.Serrano, E.A.Irene, B.Fischer, R.A.Pollak, W.Grobman

8. CONTRACT OR GRANT NUMBER(s): F19628-76-C-0249, DARPA Order-2180

9. PERFORMING ORGANIZATION NAME AND ADDRESS:
IBM T.J.Watson Research Center
P.O.Box 218
Yorktown Heights, NY 10598

10. PROGRAM ELEMENT, PROJECT, TASK AREA & WORK UNIT NUMBERS:
61101E 2180ARAE 16
Related In-House 2306J301

11. CONTROLLING OFFICE NAME AND ADDRESS:
Advanced Research Projects Agency
1400 Wilson Blvd.
Arlington, Va 22209

12. REPORT DATE: January 1977

13. NUMBER OF PAGES: 107

14. MONITORING AGENCY NAME & ADDRESS(if different from Controlling Office):
Deputy for Electronic Technology (RADC)
Hanscom AFB Massachusetts 01731
Monitor/John Garth / ETSR

15. SECURITY CLASS. (of this report): Unclassified

15a. DECLASSIFICATION/DOWNGRADING SCHEDULE:

16. DISTRIBUTION STATEMENT (of this Report):
Approved for public release; distribution unlimited

17. DISTRIBUTION STATEMENT (of the abstract entered in Block 20, if different from Report):

18. SUPPLEMENTARY NOTES:
Sponsored by the Defense Advanced Research Projects Agency (DoD) ARPA Order No. 2180

19. KEY WORDS (Continue on reverse side if necessary and identify by block number):
MOS Structures, Hole Trapping, Electron Trapping, Al Implantation, $Si_xGe_{1-x}O_2$ alloys.

20. ABSTRACT (Continue on reverse side if necessary and identify by block number):
The enclosed papers discuss the trapped hole location and annihilation in Si, current and C-V instabilities in SiO_2 at high fields, annealing of neutral electron traps in irradiated oxides, Al implanted into the SiO_2 layer of MOS structures, electron trapping as a result of Al implantation, the initial oxidation regime of silicon oxidation and the electronic structure of SiO_2, $Si_xGe_{1-x}O_2$, GeO_2.

DD FORM 1 JAN 73 1473 EDITION OF 1 NOV 65 IS OBSOLETE

UNCLASSIFIED

SECURITY CLASSIFICATION OF THIS PAGE (When Data Entered)

TABLE OF CONTENTS

INTRODUCTION

It has been recognized since the early days of simiconductor device development that an external electric field can have a major effect on the behavior of a device. This led to the work of Garrett and Brattain (1), Kingston and Neustadter (2), and others in the 1950's on the theory of the semiconductor surface. The use of a SiO_2 passivation layer has significantly reduced these problems due to the effects of external fields. However, fields due to charges within this layer have become a major reliability concern in modern Si device technology.

MOS FET's are particularly sensitive since charges within the thin SiO_2 layer used (500 - 1000 Å) have a first order effect on the device characteristics. Voltage applied to a PN junction that intersects the Si-SiO_2 interface results in an electric field in the SiO_2. Charges in the SiO_2 change this field and change the junction characteristics. Planar integrated circuit technology results in many junctions of this type. In the case of bipolar transisters this can affect the current gain, the junction breakdown voltage and the junction leakage. In the case of MOS FET's, charges in the insulator affect the threshold voltage and the transconductance as well as the junction characteristics mentioned above.

SOURCES FOR CHARGE IN THE SiO_2 ARE AS FOLLOWS:

1. Na^+ Ions

In 1965 Snow, Grove, Deal and Sah (3) showed that Na^+ ions moving through SiO_2 were a major cause of instability in devices with SiO_2 passivating layers. At the present time this is largely under control by the use of ultra clean processing facilities to eliminate Na contamination.

2. *Positive Charge Resulting From Radiation*

It has been known for some time that radiation of various kinds results in the buildup of positive charge in the SiO_2. This was shown by Zaininger (4) for electrons, by Collins and Sah for x-rays (5), and by Snow, Grove and Fitzgerald for x-rays (6). It is generally understood that radiation creates electron-hole pairs. The electrons move readily through the oxide with a low trapping probability. A large percentage of the holes on the other hand are trapped which results in a net positive charge. This positive charge effect was originally of concern in the case of devices for use in space environments. However it remains an important consideration in modern technology since various types of radiation are used for the construction of devices. One important consideration has to do with the annealing out of this charge with subsequent device processing steps. Results will be given in subsequent sections of this report showing that some of this charge can be readily eliminated by annealing whereas other effects resulting from radiation are persistent and are not readily removed by annealing. Another important consideration has to do with the effect of the device processing conditions. Studies are underway concerning the effect of process-treatments on hole trapping. The work of DiMaria discussed in later sections of this report indicates positive charge is located near the interfaces and not in the bulk of the SiO_2. Another interesting result concerns the annihilation of the trapped positive charge by electron current (8, 9). This shows that the cross section for electron capture by holes depends on the nature of the interface. In addition, it has been observed in work that will be described later that radiation also generates neutral traps that can be filled by electron current. These neutral traps are difficult to eliminate by annealing treatments.

3. *Positive Charge Generated by High Electric Fields*

Several authors have discussed the generation of positive charge in SiO_2 as a result of the application of high electric fields. ($\sim 10^7$V/cm) including DiStefano and Shatzkes (10, 22), Klein and Solomon (12), and Shatzkes and Av-Ron (13). This effect is important since positive charge plays a major role in the electric breakdown process.

One interesting aspect concerns the location of the charge. Shatzkes and Av-Ron (12) interpret their results, based on MOS-C-V measurements and high field (I-V) measurements, as indicating that the positive charge is located in the bulk of the SiO_2. DiMaria has found using the photo I-V technique that the charge is not in the bulk of the SiO_2. The reason for the discrepancy in results is probably due to the fact that Shatzkes and Av-Ron work at large electric field strengths and DiMaria works at low field strengths. High field measurements are particularly sensitive to the behavior of local high stress points, but DiMaria's technique depends on an average behavior and is not sensitive to these high stress effects.

Another interesting result is the work of Solomon and Aitken for negative gate voltages, indicating that the threshold gate voltage required to produce a C-V shift decreases slightly with decreasing temperature; whereas, the threshold voltage for current run-away decreases rapidly for decreasing temperatures. This result is most likely due to the fact that the high field I-V characteristic for negative gate voltage is largely determined by effects associated with the Al-SiO_2 interface and the C-V shifts are associated with the Si-SiO_2 interface. These observations are inconsistent with the model of Shatzkes and Av-Ron (13) since a space charge located in the bulk of the insulator would be expected to have a comparable (although not identical) effect on the electric fields at both interfaces.

Further work is required to clarify our understanding of the positive charge generated by high electric fields and we will continue to place a major emphasis on this work due to the importance of SiO_2 breakdown in the reliability of devices.

4. Electrons and Holes Injected From the Si and Trapped in the SiO_2

Electrons and holes can gain sufficient energy as a result of the electric fields applied to semiconductor devices to surmount the Si-SiO_2 barrier and flow through the oxide. If a portion of these electrons are trapped in the oxide then a space charge is developed that applies an electric field to the semiconductor and changes the device characteristics. There are two aspects to this problem; a study of the Si to SiO_2 emission current for various device structures and for various operating voltages, and a study of the electron and hole trapping characteristics of SiO_2.

Nicollian, Goetzberger, and Berglund (14) have used an avalanche plasma in Si to inject electrons and holes into SiO_2 and as a result have observed trapping effects in the SiO_2. The main advantage of their technique is the relatively simple structure (MOS capacitor) that is required. Another advantage is the uniform and known current density that flows through the SiO_2. They suggest the importance of the water content in the SiO_2 in determining the trapping characteristics. This work has been further extended as discussed in a paper by Nicollian and Berglund (15). More recently Gdula (16) has used the same technique to study the effect of processing conditions on the electron trapping characteristics of SiO_2.

Verwey (17), Ning and Yu (18), and Young (19) have used MOS FET structures to study electron injection into SiO_2 as a result of electrons accelerated by the field of a surface depletion layer in p-type Si. These results can be described using a Schottky-emission model as suggested by Ning (18), if corrections are made for oxide scattering (19). This indicates a Maxwell-Boltzman like energy distribtuion for the hot electrons in the energy range 2.6-3.1

eV. The advantages of using this structure are the known SiO_2 current density and also the known Si surface potential. Ning, Osburn, and Yu (2) have used this structure to study electron trapping of positive charged centers in SiO_2 introduced by various annealing treatments and they observe a capture cross section of $3 \times 10^{-13} cm^2$.

Bosselaar (21) and Pepper (22) have studied injection into SiO_2 from reverse biased PN junctions and have observed trapping as a result. Trapping due to electron injection from the channel region of N channel MOS FET's has been observed by Abbas and Dockerty (23) and by Ning (24). These papers discuss the effect of this trapping on the operating characteristics of these devices.

The papers cited clearly demonstrate the practical importance of electron and hole injection and trapping and show the importance of considering these effects in device designs.

The main emphasis of our program is concerned with studies of trapping of holes and electrons in SiO_2. We use the Si avalanche technique of Nicollian, Goetzberger, and Bergland (14) and apparatus which has been developed that enables us to take the data automatically and analyze the results using computer programs to give trap densities and cross sections. We are using two general approaches for this work:

A. Studies of trapping in SiO_2 as a function of processing conditions.

B. Use of ion implantation to introduce impurities and study the trapping that results.

We have studied electron trapping in SiO_2 at room temperature and at 77°K for various processing conditions. We find less trapping in ultra dry SiO_2, and we find the post oxidation heat treatment to be crucial; however, the optimum heat treatments seems to be different for minimizing room temperature trapping as compared to trapping at 77°K. We also find a different thickness dependence for room temperature and for 77°K. This work is being assessed and will be reported in detail in the next report.

Our work on hole trapping is just beginning. However, preliminary results indicate that the heat treatment for minimum hole trapping at room temperature is similar to the heat treatment to minimize 77°K electron trapping. In both of these cases, our results indicate that the trapping is associated with the Si-SiO_2 interface. We will be using the photo I-V technique of DiMaria to investigate this further.

The work with ion implanted impurities has been largely concerned with Al. Al was selected for our initial emphasis due to the published work describing the use of Al for radiation hardening and due to the extensive use of Al metallurgy. Previous work on electron trapping in Al implanted SiO_2 has been done by Johnson, Johnson, and Lampert (25). Their results indicated that the trapping was due to displacement damage remaining after the 600°C annealing temperature they used. In our work, we used an annealing temperature of 1050°C with the hope of eliminating this damage, and this temperature certainly did reduce the trapping significantly. However, the observation that the trapping varies as the (implantation energy)^2 instead of (implantation energy)^1 as expected on the basis of the charge centroid effect suggests that damage is still involved. We have also measured the centroid of the trapped charge and found agreement with the centroid of the implanted Al as measured by SIMS, and reasonably good agreement with the profiles using L.S.S. theory. The actual profiles are broader than the theory predicts. We are now extending this work to other implanted species.

5. *Structure of Thin SiO_2 Films*

Electric breakdown theory indicates an increase in the breakdown field strength for thin SiO_2 films. The use of thinner films in the gate region of MOS FET's result in technological improvements. This would reduce the operating voltages which would also make it possible to also reduce the thickness of the thick-field oxide. The result of this would be to increase the resolution of some of the photo-lithography steps, improve edge coverage on thick to thin

steps, and decrease the high temperature processing time. Shorter times would reduce unwanted diffusions, etc.

The main limitation in reducing the thickness of the gate SiO_2 is due to defects. Our results indicate a reduction in these defect densities if the thin oxide is grown in an environment containing trace amounts of H_2O.

6. *The Electronic Structure of SiO_2, $Si_xGe_{1-x}O_2$, and GeO_2 from Photoemission Spectroscopy.*

The important electronic properties of SiO_2 are controlled by the band structure. One means for increasing our understanding of the nature of the band structure of SiO_2 is to study the system $Si_xGe_{1-x}O_2$ as the germanium content is varied. The results of this work give added insights concerning the importance of the O-O bond length in determining the nature of the valence band. This is also o interest for use in fiber optics.

SUMMARY OF IMPORTANT RESULTS

- I. The photo I-V technique has been used to determine the location of the positive charge in SiO_2 that results from exposure to radiation or from the application of large electric fields. This charge has been found to be located at the Si-SiO_2 or the Al-SiO_2 interfaces and not in the bulk of the SiO_2.
- II It has been observed that neutral traps are generated in SiO_2 as a result of x-ray or electron beam irradiation.
- III Al implanted into SiO_2 results in broader profiles than predicted using L.S.S. theory. The enhanced electron trapping resulting from Al implantation varies as the (implantation energy)^2.
- IV Trace amounts of H_2O during SiO_2 growth reduce defect density (as measured by electric breakdown) in thin films.

- V Studies of the $Si_xGe_{1-x}O_2$ system indicate that the electronic structure of the valence band is primarily determined by the O-O bond length.

REFERENCES

1. C. G. B. Garrett and W. H. Brattain, Phys. Rev. *99*, 375 (1955).
2. R. H. Kingston and S. F. Neustadter, J. Appl. Phys. *26*, 718 (1955).
3. E. H. Snow, A. S. Grove, B. E. Deal and C. T. Sah, J. Appl. Phys. *36*, 1664 (1965).
4. K. H. Zaininger, Appl. Phys. Letters *8*, 140 (1966).
5. D. R. Collins and C. T. Sah, Appl. Phys. Letters *8*, 124 (1966).
6. E. H. Snow, A. S. Grove and D. J. Fitzgerald, Proc. IEEE *55*, 1168 (1967).
7. G. F. Derbenwick and B. L. Gregory, IEEE Annual Conference on Nuclear and Space Radiation Effects, July 14, 1975.
8. J. M. Aitken and D. R. Young, J. Appl. Phys. *47*, 1196 (1976).
9. J. M. Aitken, D. J. DiMaria and D. R. Young, to be published in IEEE Trans. Nuc. Sci., NS-23 (1976).
10. T. H. DiStefano and M. Shatzkes, Appl. Phys. Lett. *25*, 685 (1974).
11. T. H. DiStefano and M. Shatzkes, J. Vac. Sci. Technol. *13*, 50 (1976).
12. N. Klein and P. Solomon, J. of Appl. Phys. *47*, 4364 (1976).
13. W. Shatzkes and M. AV-Ron, J. of Appl. Phys. *47*, 3192 (1976).
14. E. H. Nicollian, A. Goetzberger and C. N. Berglund, Appl. Phys. Lett. *15*, 174 (1969).
15. E. H. Nicollian and C. N. Berglund, J. of Appl. Phys. *42*, 5654 (1971).
16. R. A. Gdula, J. Electrochem. Soc. *123*, 42 (1976).
17. J. F. Verwey, J. Appl. Phys. *44*, 2681 (1973).
18. T. H. Ning and H. N. Yu, J. Appl. Phys. *45*, 5373 (1974).
19. D. R. Young, J. Appl. Phys. *47*, 1098 (1976).

TRAPPED HOLE LOCATION AND ANNIHILATION IN SiO_2 FILMS ON Si

D. J. DiMaria, J. M. Aitken, and Z. A. Weinberg

Positive charge has been introduced into the dry grown SiO_2 layer of MOS strcutures using either 20 keV x-rays, 16.85 eV light or a high negative gate voltage. We have used the photo I-V technique (1, 2) to determine the location of this charge. In all cases, our observations indicate that this charge is located at or near the interfaces ($\leq$50 Å from the interface) and not in the bulk of the SiO_2. This observation is in direct conflict with models of SiO_2 breakdown which rely on a *stationary* trapped hole distribution in the bulk of the oxide layer (3, 4).

The location of the trapped charge in the oxide layer is determined by the change in the photocurrent voltage characteristics of both interfaces after irradiation or high field stressing. For charge located near just one interface (as is the case here), the photo I-V characteristic for the charged interface is distorted as compared to that for the uncharged sample. The photo I-V characteristic for the other interface shows only a slight parallel shift with respect to that for the uncharged sample. These measurements are discussed in detail in recent publications (1, 2).

Trapped holes are predominantly distributed near the interface towards which they are driven by the field during irradiation, although some may be trapped near the other interface. Most of the holes trapped near the Si-SiO_2 interface can be annihilated very easily by electrons injected from either the Si or the Al by internal photoemission or by avalanche injection from the Si. This electron capture process has a coulombic capture cross section (10^{-12}-10^{-13}cm^2) at low average fields ($\leq$ 1 MV/cm) which decreases rapidly at higher average fields ($\approx 10^{-15}$cm^2 at 6 MV/cm). Figure 1a shows the effect on the photocurrent for positive gate bias (Si injecting), before and after irradiation, and after hole annihilation with electrons. As seen in this figure all the holes distributed near the Si-SiO_2 interface are annihilated except for possibly some approximately at the Si-SiO_2 interface which cannot be sensed by the photo I-V techni-

que (5). Similarly, capacitance-voltage measurements show almost a complete recovery of the flat-band voltage except for $\leq$ -1 V of surface states. However, most of the holes trapped near the Al-SiO_2 interface are difficult to remove under any type of electron injection. The effective electron capture cross section for these trapped positive charges determined to be less than $10^{-14}cm^2$, assuming all detrapping mechanisms (photo, thermal and field) are negligible during photocurrent injection. Figure 1b shows the effect on the photocurrent for negative gate bias (Al injecting) before and after irradiation, and after various attempts to annihilate these trapped holes with photoinjected electrons from either interface with different field conditions. As seen in this figure only a small fraction ($\approx$ 20%) of the holes were annihilated and the photo I-V characteristic never returned to its pre-irradiation state.

REFERENCES

1. D. J. DiMaria, Z. A. Weingerg, and J. M. Aitken, J. Appl. Phys. *48*, 898 (1977).
2. J. M. Aitken, D. J. DiMaria, and D. R. Young, IEEE Trans. Nuc. Sci. (Dec. 1976).
3. T. H. DiStefano and M. Shatzkes, Appl. Phys. Lett. *25*, 685 (1974); J. Vac. Sci. Technol. *13*, 50 (1976).
4. M. Shatzkes and M. Av-Ron, J. Appl. Phys. *47*, 3192 (1976).
5. R. J. Powell and C. N. Berglund, J. Appl. Phys. *42*, 4390 (1971).

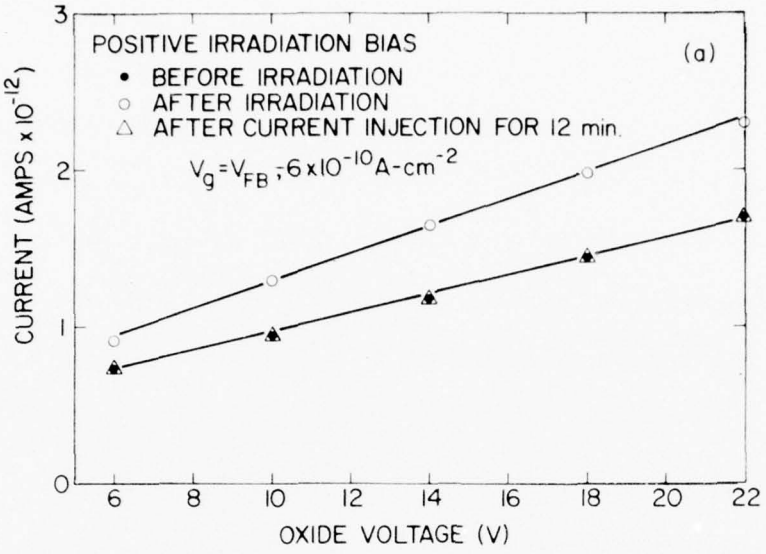
POSITIVE IRRADIATION BIAS
(a)
• BEFORE IRRADIATION
○ AFTER IRRADIATION
△ AFTER CURRENT INJECTION FOR 12 min.
$V_g = V_{FB}$; 6×10^{-10} A-cm^{-2}
CURRENT (AMPS x 10^{-12})
OXIDE VOLTAGE (V)
0
1
2
3
6
8
10
12
14
16
18
20
22

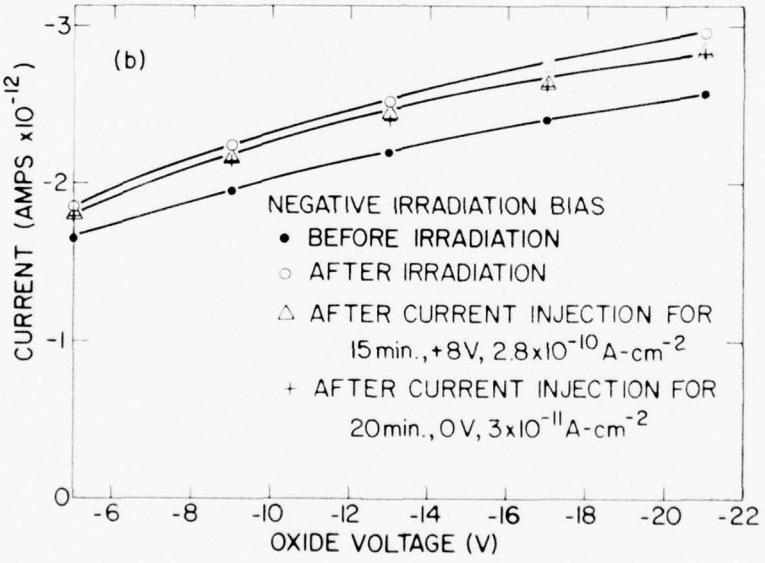
(b)
NEGATIVE IRRADIATION BIAS
• BEFORE IRRADIATION
○ AFTER IRRADIATION
△ AFTER CURRENT INJECTION FOR
15 min., +8V, 2.8×10^{-10} A-cm^{-2}
+ AFTER CURRENT INJECTION FOR
20 min., 0V, 3×10^{-11} A-cm^{-2}
CURRENT (AMPS x 10^{-12})
OXIDE VOLTAGE (V)
0
-1
-2
-3
-6
-8
-10
-12
-14
-16
-18
-20
-22

FIGURE CAPTIONS

Figure 1

Photo I-V characteristics for MOS capacitors subjected to irradiation and then photoinjection. The upper figure (a) shows the change in characteristic caused by charge induced near the Si-SiO_2 interface by irradiation under positive bias (20 KeV, 25 ma, 13 min, + 9V). Electrons injected at a rate of ~ -6 x 10^{-10}A-cm^{-2} while the gate voltage was maintained at the flat-band voltage ($V_g = V_{FB}$) annihilate this charge within a period of 12 minutes. In the lower figure (b) the change in characteristic caused by charge induced near the Al-SiO_2 interface by irradiation under negative bias (20 KeV, 25 ma, 40 min., -15 V). The relaxation of this charge under various injection conditions are displayed as follows:

open triangles: +8V, +2.8 x10^{-10}A-cm^{-2}, 15 minutes

crosses: +0V, ~ + 3 x10^{-11}A-cm^{-2}, 20 minutes

+0V, + 3.6 x 10^{-11}A-cm^{-2}, 20 minutes

+8V, + 2.6 x 10^{-10}A-cm^2, 285 minutes

-6V, -6.0 x 10^{-10}A-cm^2, 554 minutes

CURRENT AND C-V INSTABILITIES IN SiO_2 AT HIGH FIELDS

P. M. Solomon and J. M. Aitken

ABSTRACT

Results have been obtained concerning the interrelation of current and C-V instabilities in MOS capacitors subjected to negative gate high field pulsing. Rising current transients and negative C-V shifts both show the formation of positive charge in the oxide. However, this charge appears to be situated close to the electrodes rather than in the bulk of the oxide and the temperature dependence of the rate of charge accumulation near the electrodes is different for the aluminum and silicon electrodes.

In their studies of Al-SiO_2-Si capacitors subjected to high field stressing many workers[1-4] have observed shifts to negative gate voltages in the capacitance vs voltage (C-V) curves corresponding to positive charge in the oxide. Rising current transients have also been observed and generally have been interpreted[1,3,5] as an increase in Fowler-Nordheim injection[6] due to holes remaining after impact ionization in the oxide.

There has been a tendency in the literature[1, 3] to couple the two phenomena together and postulate that a bulk positive charge exists which influences both emission currents from the aluminum and C-V shifts in proportion to the distance of the charge from the respective interface.[3] There were, however, some facts which refuted this simple picture, notably:

1. Solomon[2, 5] found that under suitable conditions the positive charge causing the current increase could reversibly be created or relaxed out of the insulator whereas in the same experiment the C-V shift continually increased.
2. DiMaria[7], using internal photoemission, has shown that the charge causing the C-V shift is confined near the Si-SiO_2 interface where it cannot influence the current injected from the gate.

The above facts prompted the present investigation and in this communication we shall show that two independent mechanisms exist for producing charge in the oxide at high fields, one producing charge which is trapped at the Si-SiO_2 interface (detected by C-V shifts) and the other at the Al-SiO_2 interface.

The samples consisted of 30 mil diamter 5000 Å thick Al dots evaporated from a resistance heated tungsten boat on a 715 Å thick SiO_2 film grown on a <100> 0.2 Ω-cm p-type silicon substrate. The oxide was grown at 1000°C in any oxygen ambient and a post-metallization anneal of 20 min in forming gas at 400°C were used. Mobile sodium concentrations measured using temperature bias method were less than $5 \times 10^{+10} cm^{-2}$.

A double pulse technique was used (see ref. 5 for more details) whereby the sample was prestressed at a relatively low field of 6.5 MV/cm (Al negative) and then a high field (8MV/cm) pulse of the same polarity was applied after which the sample was returned to the low field. Currents were monitored at both fields and C-V curves were taken before and after each pulse sequence. The experiment was repeated at room temperature, 195°K and 77°K. As expected, both negative C-V shifts and rising current transients were observed at high fields. The relative rates of current increase and increase in C-V shift with time increased extremely rapidly with applied field in a quasi-exponential manner. The current density is also a strong function of field according to the Fowler - Nordheim relation. However, the above two effects have even stronger field dependencies. This result, for the current, is in agreement with ref. 5. As is shown in the insert of Fig. 2, the current does not continue to increase at longer times, instead it saturates and eventually decreases slowly with time. This behaviour could be due to the combined effects of recombination and electron trapping[8, 9, 10]. In contrast to this, as seen in Fig. 1, the C-V shift increases monotonically with time.

Table I summarizes the temperature dependence of the voltage at which the C-V shifts or current increases became apparent. The threshold voltage for current increases drops rapidly as the temperature is lowered. The threshold voltage for the C-V shift is defined as the voltage at which .2V shift is observed in the first ten second stressing pulse. This voltage does not depend strongly on temperature. It was impossible to measure the threshold for C-V shifts at liquid nitrogen temperature because the current runaway was strong enough to cause breakdown in all the samples that were measured, before any trace of positive charging at the silicon interface was observed. The rate of C-V shift with time is seen to be temperature independent whereas the current increase phenomena is strongly enhanced at the lower temperatures. The differences are very striking when Figs. 1 and 2 are compared. The agreement in Fig. 1, in the rates of C-V shift at 300°K and 195°K is remarkable considering the steep voltage dependence of the effect. On the other hand, in agreement with ref. 5, there

are orders of magnitude difference in the rates of current increase (1:65:5500 from Fig. 2) when going from room through dry ice to liquid nitrogen temperatures.

The above results how differing temperature and time dependencies and offer strong proof that the C-V shifts and current increases are the result of independent processes. Indeed under suitable conditions it is possible to get C-V shifts without current increases (at room temperature) or vice-versa (at liquid nitrogen temperature). This supports the statements in the first paragraph where the charge causing the two effects is confined to the interface regions. In the case of radiation induced charge, photoemission work by Aitken et al[11] and hole transport measurements by Hughes[12] similarly led to the conclusion that charge is trapped near the interfaces with little remaining in the bulk. It is possible that current increases could be obtained without accompanying C-V shifts if the current was highly localized in current filaments. The reproducibility of the current increases from sample to sample argues against this. However, experiments are planned to resolve this point. It is important to note that charge localization near the electrodes only gives independence between C-V shifts and current increases for injection from the gate electrode. For the gate positive a close correlation between oxide current increases and C-V shifts should be observed. Such correlation has been observed in the past and further experiments are underway to confirm this.

The existence of two independent mechanisms for the formation of positive charge at the Al-SiO_2 and Si-SiO_2 interfaces under high field negative gate pulsing has been demonstrated. This opens a fruitful area of study as to the origin of these two effects and may enhance our understanding of the MOS system and possibly lead to improvements in field effect transistor technology.

REFERENCES

1. C. M. Osburn and E. J. Weitzman, J. Electrochem. Soc., *119*, 603 (1972).
2. P. M. Solomon, D. Sc. Thesis (Technion, Haifa, Israel 1974) Unpublished.
3. M. Shatzkes and M. Av-Ron, J. Appl. Phys., *47*, 3192 (1976).
4. D. J. Breed, Appl. Phys. Lett., *26*, 116 (1975).
5. P. Solomon and N. Klein, Solid State Comm., *17*, 1397 (1975).
6. M. Lenzlinger and E. H. Snow, J. Appl. Phys. *40*, 178 (1969).
7. D. S. DiMaria, Z. W. Weinberg, and J. M. Aitken, submitted to J. Appl. Phys.
8. N. Klein and P. Solomon, J. Appl. Phys., *47*, (4364) (1976).
9. P. Solomon, to be published.
10. E. H. Nicollian and C. N. Berglund, J. Appl. Phys. *41*, (3052) 1970.
11. J. M. Aitken, D. J. DiMaria, and D. R. Young, IEEE Trans. Nuc. Sci., Dec. 1976.
12. R. C. Hughes, Appl. Phys. Lett., *26*, 436 (1975).

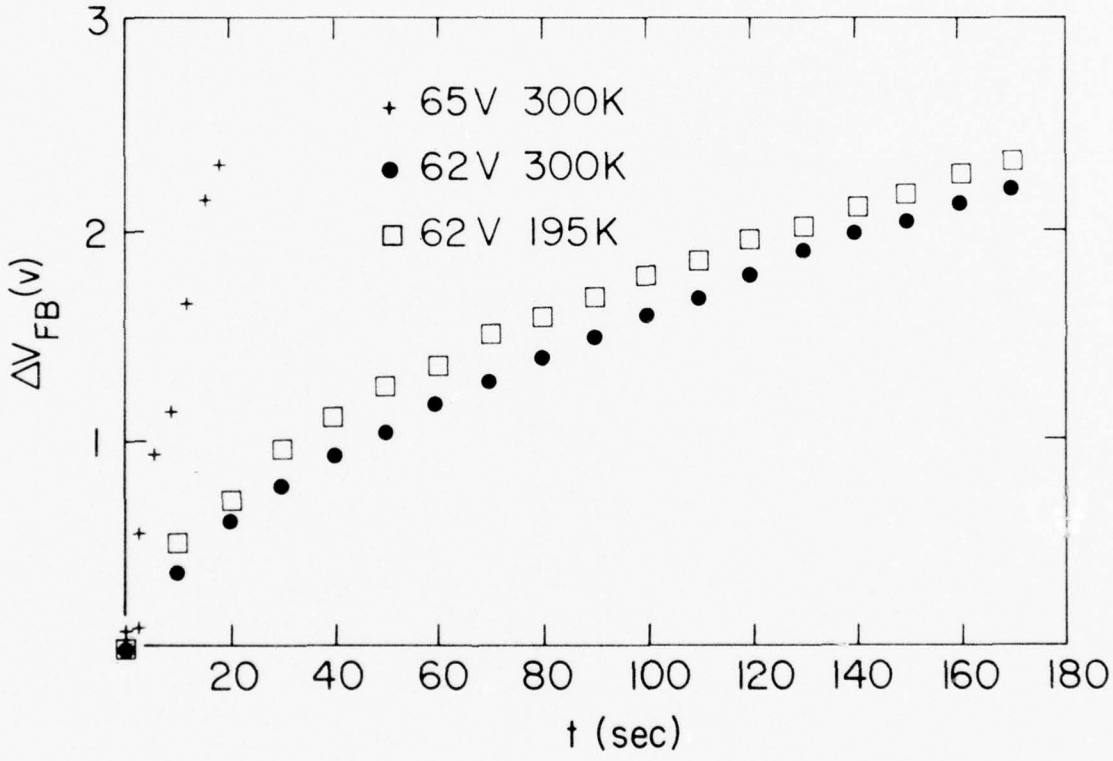

Figure 1 Flatband voltage shift as a function of time for successive pulses.

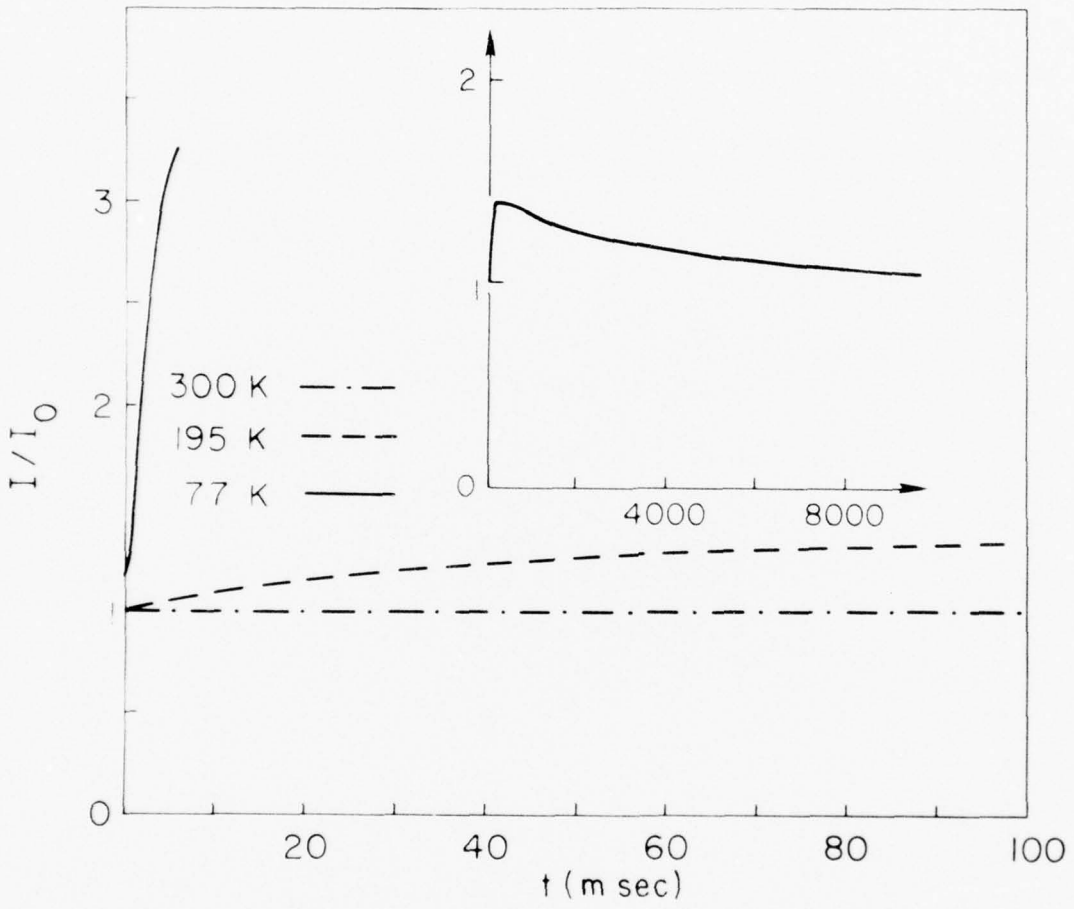

Figure 2 Current vs time at 300°K, 195°K and 77°K for a -62V gate voltage applied at t=0. Insert shows the 195°K pulse on an expanded time scale.

TABLE I

THRESHOLD VOLTAGE

Temperature	77 K	195 K	300 K
Threshold voltage for current increases	52	56	60
Voltage for .2V CV shift in 10 sec	Sample broke down	62	62

ANNEALING OF NEUTRAL ELECTRON TRAPS IN IRRADIATED OXIDES

J. M. Aitken, K. Pan, and D. R. Young

ABSTRACT

The generation of neutral trapping centers with cross-sections in the $10^{-17}cm^2$-$10^{-18}cm^2$ range in aluminum and poly-silicon gate capacitors is shown to result from electron beam irradiation of these capacitors. Unlike positively charged centers and surface states introduced by such a treatment, these centers are not reduced to their pre-irradiation levels by anneals at 400°C in forming gas. In fact, little change in the post-irradiation trapping efficiency is noted for forming gas anneals up to 500°C for extended times.

Damage caused by ionizing radiation severely limits the reliability of MOS field-effect devices. Metal-Oxide-Semiconductor devices exposed to radiation of this type exhibit increased levels of positive charge in the oxide and an increased surface state density.[1] In addition to these effects, which are obvious from a simple C-V measurement on a capacitor or from a conductance measurement in an FET structure, a significant number of neutral trapping centers are introduced by ionizing radiation into the oxide layer.[2] Although it has been shown that the positive charge and the surface states introduced into aluminum gate devices by ionizing radiation anneal out at temperatures below 400°C no work has been performed to study the annealing behavior of damage associated with neutral trapping centers. This question is addressed here. MOS capacitor structures have been subjected to a range of dosages of 25 keV electrons, annealed at various times and temperatures and then subjected to a current of hot electrons injected from the substrate to populate any residual neutral trapping sites. In general, it was found that the residual damage associated with neutral traps does not anneal out at temperatures up to 500°C and that the density of these traps increases with increasing dosage.

Because neutral traps are essentially uncharged they are expected to have a small ($<10^{-17}cm^2$) capture cross-section. Their presence in the oxide layer of unirradiated MOS capacitors has been reported by various authors. Aitken and Young[2] have shown increased density of neutral traps in MOS capacitors subjected to x-ray irradiation.

Aluminum gate capacitors used in this study consisted of a circular aluminum electrode 32 mils in diameter and 5000 Å thick evaporated onto a 500 Å thick SiO_2 film on a 0.1Ω-cm p-type (100) silicon substrate. The film was grown in dry O_2 at 1000°C. During the course of irradiation, annealing and measurement, this structure was left intact. The samples received a 400°C post-metal anneal for 30 minutes, in a forming gas ambient (90% N_2, 10% H_2) after r-f aluminum evaporation. Poly-silicon gate capacitors were dry-grown under similar conditions on similar substrate material. However, after oxide growth a 3500 Å layer of poly-silicon

was deposited by chemical vapor deposition at 650°C and doped with $POCL_3$ followed by a 1000°C drive in anneal for 30 minutes. An aluminum overlayer was used to define 32 mil dots, resulting in an Al-polysi-SiO_2-Si sandwich.

Before irradiation the trapping characteristic of the device as well as high frequency and quasi-static C-V curves were measured. The capacitors, their gates floating, were then individually irradiated with 25 keV electrons to the appropriate fluence which was measured after the irradiation and exhibited a negative flat-band shift which saturated at -2 volts for dosages above 2.5 x 10^{-4}coul-cm^{-2}, a distortion of the high frequency and quasi-static C-V curves and a large density of traps with cross-section between 10^{-13} and 10^{-18}cm^2. The samples were then annealed in forming gas at 400°C and remeasured. In the aluminum gate capacitors this anneal was effective in removing all the positive charge and surface states introduced by the irradiation and all the traps with cross-sections greater than 10^{-17}cm^2. Additional anneals on the same wafer were performed at 500°C. Because aluminum begins to react with and diffuse into bare silicon around this temperature, a practical upper limit exists for any annealing step with aluminum metallurgy. This is important in device structures where the radiation damage generated in a lithographic step to define aluminum gate metallurgy must be eliminated by an anneal. All the measurements were taken on the same 1 1/4" wafer for consistency but similar results were noted on other wafers.

Between the various steps of irradiation and annealing the neutral trap density and cross-section were determined by measurement in an apparatus which maintains a constant average dc current through the capacitor and periodically interrupts the injection to measure the shift in flat-band voltage. This technique has been discussed elsewhere[2, 6, 7] but involves injection of hot electrons from the silicon substrate over the field-lowered barrier at the Si-SiO_2 interface and into the oxide bulk. Experimentally, the devices are driven into deep depletion by an alternating positive voltage pulse at the gate with a frequency (500 KHz) too high to allow the formation of an inversion layer. A feed-back circuit automatically adjusts the

voltage at the gate to compensate for any variation in the field at the injecting silicon contact and maintains a constant average avalanche current. As electronic current is passed through the sample a certain fraction of this charge is trapped in the oxide and induces an image charge in the silicon resulting in a change of the flat-band voltage V_{FB}. Capacitors were irradiated with 25 keV electrons up to a maximum fluence of 1 x 10^{-4}coul-cm^2. This dosage is typical of those used in modern E-beam lithography. These were then annealed in a 90% N_2, 10% H_2 mixture at 400°C for 30 minutes and avalanche injected at a current of 2 x 10^{-17} A. The resulting change in flat-band voltage as a function of injection time is shown in Fig. 1. Note that the total flat-band shift increases with increasing dosage and that the 400°C anneal does not return the capacitor to its original state.

The effective trapping efficiency[8] is defined experimentally by the relation

$$\eta = \frac{Cox\Delta V_{FB}}{j \quad \Delta t}$$

where Cox is the oxide capacitance per unit area and j is the current density. Essentially it is the ratio of the rates of charge injection to charge trapping (as sensed at the silicon, injection at constant current). This quantity is particularly useful for comparisons of various cases because it measures the initial rate of threshold shift of the device through the derivative of the curves in Fig. 1. The effective trapping efficiency is given as a function of the irradiation dosage in Table I. It varies by a factor of 3.4 between the control oxide and the oxide irradiated to the highest dosage and then annealed. These curves were also fit by a least squares program to a sum of two exponentials from which the trapping cross-sections can be determined. This technique is described in detail elsewhere.[2] The best fit cross-sections grouped around an average of 1 x 10^{-17}cm^2 and 1 x 10^{-18}cm^2. These numbers are only reliable within a factor of two but are representative of the cross-sections quoted by others in unirradiated oxides. The trap densities are around 1 x 10^{11} cm^{-2} for the larger cross-section trap and 3 x 10^{11}cm^{-2} for the smaller. Since the effective trapping rate is given by the sum of the

products of the cross-sections and trap densities, the larger cross-section trap dominates the initial effective trapping efficiency.

The extent to which traps remain in the oxide after annealing seems to be independent of the initial numbers of traps present in the as-grown oxide. This point is illustrated in Fig. 2, where the shift in flat-band voltage is plotted against injection time at a constant current of 2 x 10^{-7} A for two 500 Å oxides, one with a poly-silicon gate, the other with an aluminum gate. Both these samples were given identical E-beam exposures (10^{-4} coul-cm^{-2} at 25 keV) and identical anneals (400°C, 30 min, in 90% N_2, 10% H_2) then compared with similar controls. Even though the poly-silicon gate capacitor started with a lower density of neutral traps than the aluminum gate in the initial oxide, little difference exists between it and the other after the irradiation and annealing steps. The trapping efficiency calculated from this figure is presented in Table II. Note that even though the irradiated and annealed capacitors have about the same initial effective trapping efficiency this quantity is much lower for the poly-silicon gate capacitor in the as-grown state than for the aluminum gate capacitor in the as-grown state. The reason for the reduced density in the poly-silicon gate devices is not understood at this time but perhaps the additional hot processing they receive (a drive-in step at 1000°C) eliminates the water-related centers usually associated with these traps.

The extent to which the traps are removed by annealing is shown in Fig. 3. The flat-band shift due to capture of electrons by traps with electron capture cross-sections in the range of 10^{-17}cm^{-2} to 10^{-18}cm^2 is shown as a function of injection time at a current of 2 x 10^{-7} A. The large number of these traps present after irradiation are reduced significantly by the first anneal (400°C, 30 min, 90% N_2, 10% H_2). The same sample was subjected to an additional 10 min. anneal at 500°C in forming gas. As seen in Fig. 3, there is a slight improvement in the long term trapping after this anneal. The initial trapping efficiency calculated from the initial slope of this curve is given in Table I and shows only about a 20% improvement. Most of the improvement is due to the reduction in levels of the smaller cross-section (10^{-18}cm^2)

trap.

An additional forming gas anneal at 500°C for 20 minutes was carried out and little improvement over the prior anneal was noted. The initial trapping rates for samples which receive a dosage of 7.5 x 10^{-5}coul-cm^{-2} and were annealed at 500°C for 30 minutes following a 400°C anneal for 30 minutes and a sample which received only a 500°C anneal for 30 minutes are compared in Table I and shown to be identical. In fact, the flat-band shifts as a function of tiem for these two cases were identical within 100 mV.

In conclusion we have shown that in addition to the trapped holes which are generated in the SiO_2 layer by ionizing radiation, additional neutral electron traps with cross-sections of 10^{-17}cm^2 to 10^{-18}cm^2 are also formed. The usual low temperature anneal which restores the positive charge and surface state densities to the pre-irradiation level, does not bring the neutral trap density to this level. Annealing at temperatures of 500°C for 30 minute periods is also ineffective in eliminating these traps completely. In conjunction with hot electron effects, these additional neutral centers introduced by irradiation steps in the fabrication of the device, can limit the useful lifetime of the device significantly.

REFERENCES

1. E. H. Snow, A. S. Grove and D. J. Fitzgerald, Proc. IEEE, *55*, 1168 (1967).
2. J. M. Aitken and D. R. Young, J. Appl. Phys. *47*, 1196 (1976).
3. K. H. Zaininger, Trans. IEEE PTGNS, NS-13, 237 (1966).
4. D. R. Young and E. A. Irene, unpublished.
5. D. J. DiMaria, J. M. Aitken and D. R. Young, J. Appl. Phys., *47*, 1740 (1976).
6. E. H. Nicollian, A. Goetzberger, and C. N. Berglund, Appl. Phys. Lett. *15*, 174 (1969).
7. E. H. Nicollian and C. N. Berglund, J. Appl. Phys., *41*, 3052 (1970).
8. T. H. Ning, C. M. Osburn, and H. N. Yu, Appl. Phys. Lett., *26*, 248 (1975).

TABLE I

DOSAGE (Coul-cm^{-2}	ANNEAL HISTORY	($\eta(0)$)
———	———	1.3×10^{-6}
1×10^{-5}	400°C, 30 min	1.7 "
2.5"	400°C, 30 min	2.3"
5.0"	400°C, 30 min	2.8"
7.5"	400°C, 30 min	3.2"
10"	400°C, 30 min	3.8"
10×10^{-5}	400°C, 30 min	3.1"
	500°C, 10 min	
7.5×10^{-5}	400°C, 30 min	3.1"
	500°C, 30 min	

TABLE II

Gate Material	Dosage (Coul-cm^{-2}	$\eta(0)$
Al	———	1.3×10^{-6}
Al	10^{-4}	3.8×10^{-6}
Poly-si	———	$.2 \times 10^{-6}$
Poly-si	10^{-4}	3.5×10^{-6}

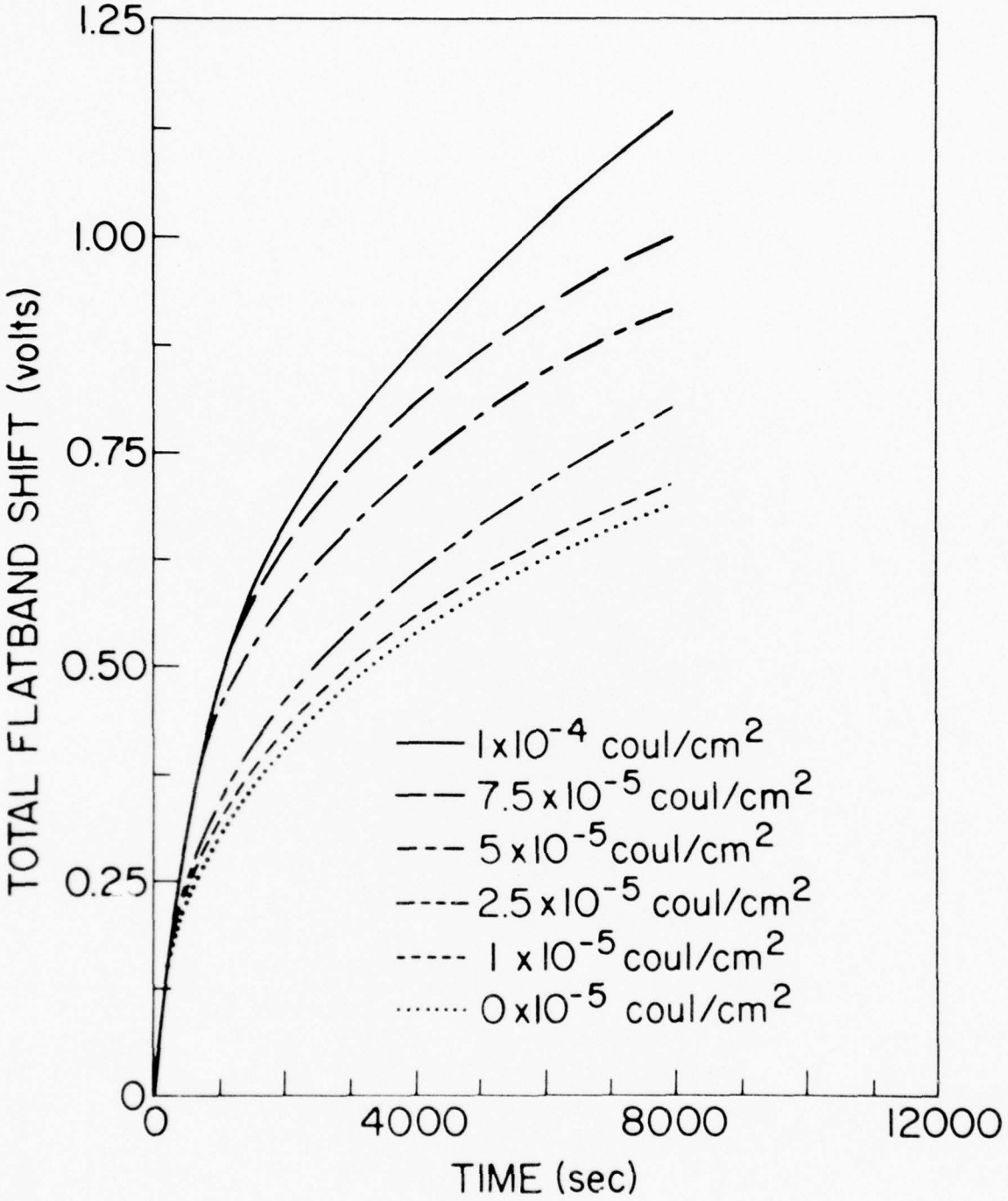

Figure 1 Shift in the flat-band voltage of aluminum gate capacitors as a function of time during avalanche injection at a current of 2×10^{-7} A. These capacitors were subjected to the indicated exposures of e-beam irradiation and then annealed for 30 minutes at 400°C in a forming gas (90% N_2, 10% H_2) ambient.

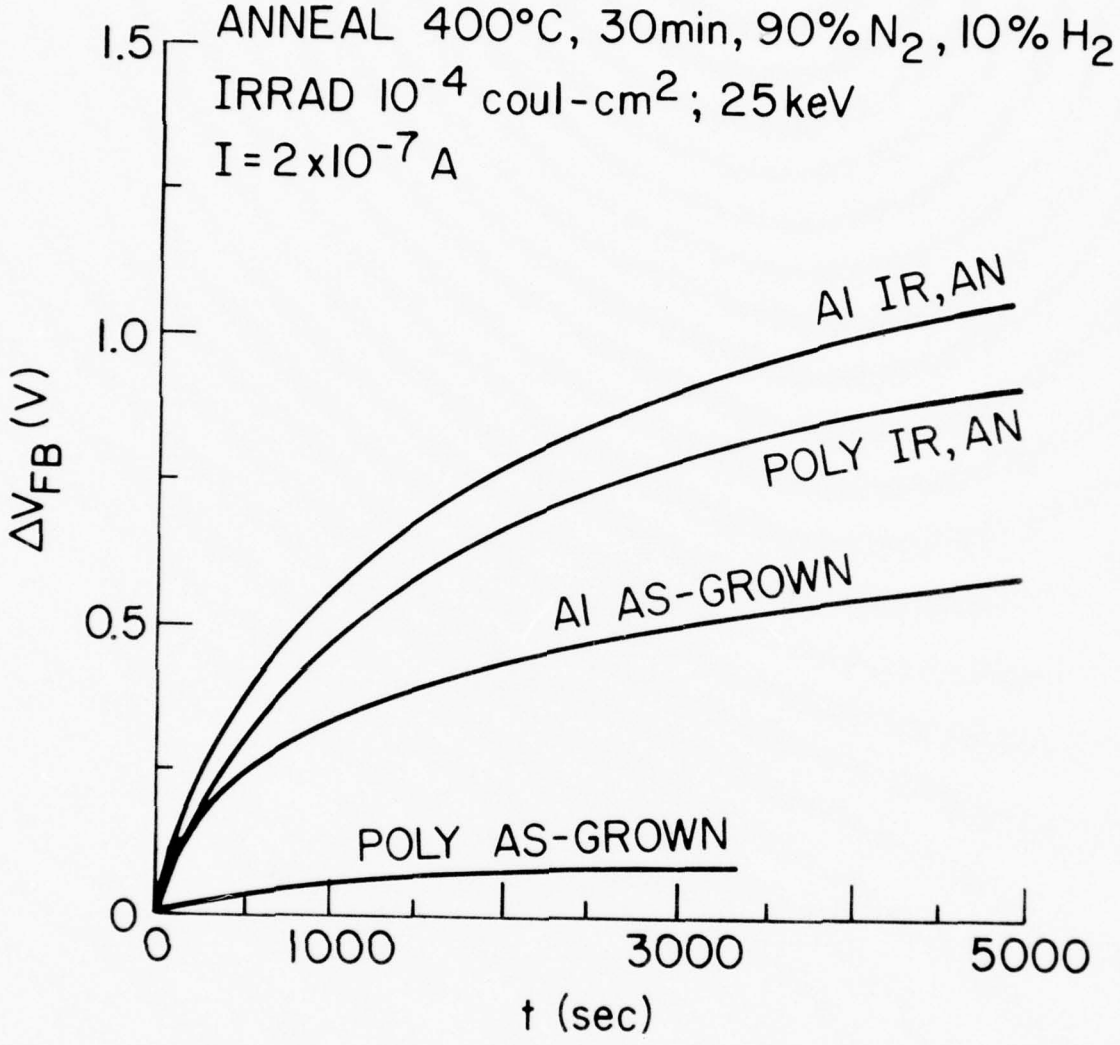

Figure 2 Comparison of the trapping behanior of poly-silicon gate and aluminum gate capacitors which were subjected to identical irradiation (10^{-4}coul-cm^2) and annealing (400°C, forming gas, 30 min) treatments. The flat-band shift is plotted as a function of time for an injection current of 2×10^{-7} A.

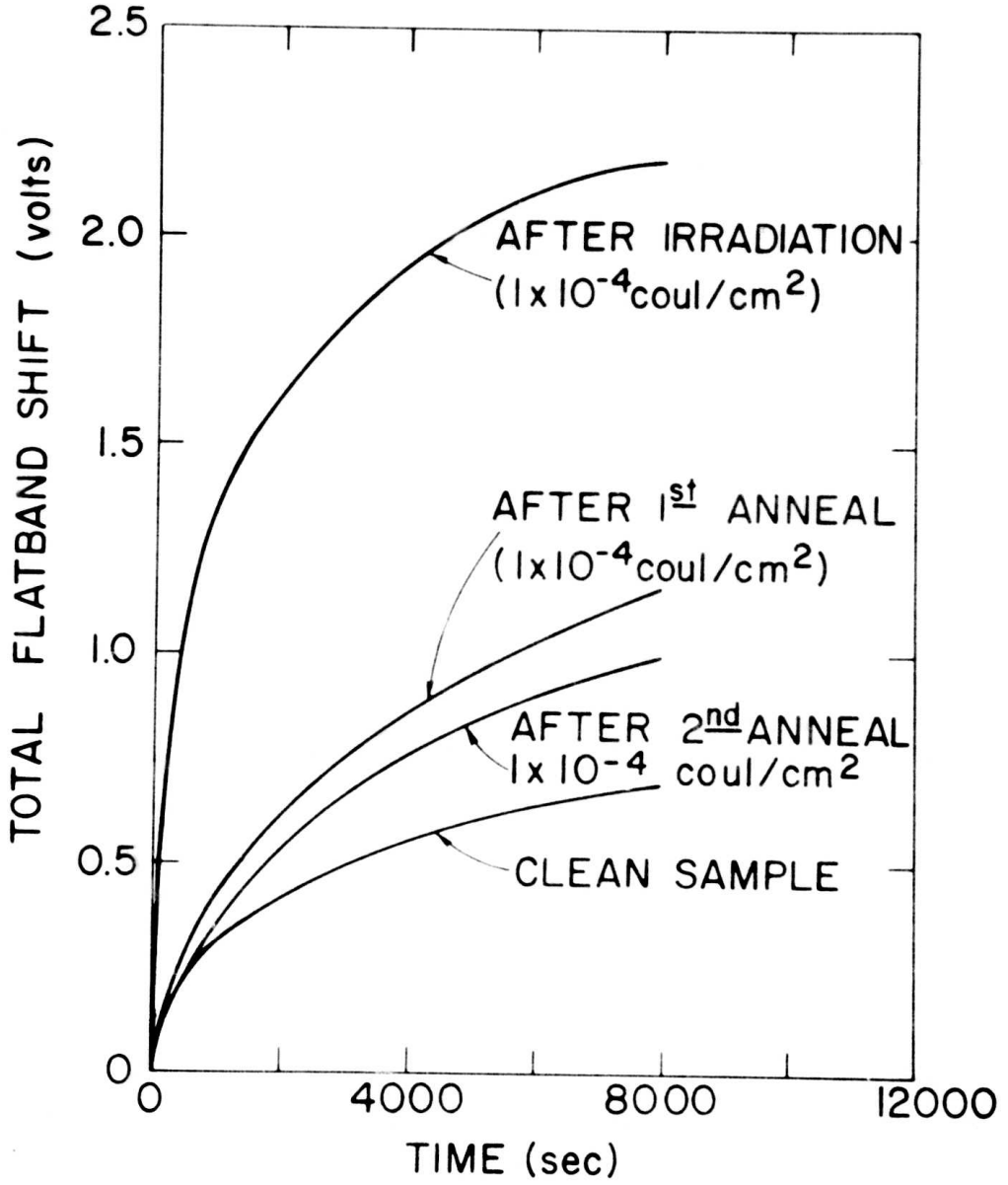

Figure 3 Comparison of the effect of various anneals on e-beam irradiated (10^{-4}coul-cm^{-2}) aluminum gate capacitors. The samples were irradiated and given the following successive anneals in forming gas.

400°C	30 min (1st anneal)
500°C	10 min (2nd anneal)
500°C	20 min (3rd anneal)

ELECTRON TRAPPING IN SiO_2 AS A RESULT OF AL IMPLANTATION

D. R. Young, W. R. Hunter, D. J. DiMaria, C. M. Serrano

I. INTRODUCTION

The effect of Al implantation on the electron trapping behavior of SiO_2 has been studied by Johnson, Johnson and Lampert (1) using MOS structures. They used a fluence of 1×10^{14} at/cm^2 at 20 keV with a SiO_2 thickness of 1400 Å. This work indicated that most of the traps were due to displacement damage. The maximum annealing temperature was 600°C. In a recent talk given by D. R. Young (2) some data were presented showing that annealing temperatures up to 1050°C result in a substantial reduction in the trapping rate. It was hoped that these high temperature anneals would eliminate the displacement damage and enable us to study the trapping associated with the Al sites. We have also varied the SiO_2 thickness from 490 to 1400 Å and the implantation energy from 15 keV to 40 keV. The location of the trapped charge has been studied on the sample samples by DiMaria, Young, Hunter and Serrano using the photo I-V technique and these results are given in a later section.

II. EXPERIMENTS

A. Sample Preparation

Silicon p-type wafers are used with a resistivity of 0.1 to 0.2 ohm-cm. The SiO_2 is grown at 1000°C in a dry oxygen environment. The samples are ion implanted and then cleaned. A heat treatment of 1050°C for 30 minutes is used. As soon as possible after the heat treatment, Al metallurgy is applied in the form of dots, .080 cm, in diameter, by evaporation followed by a post metallization annealing treatment of 400°C for 30 minutes in N_2.

B. Measurement Technique

The electron current is induced in the SiO_2 using avalanche injection from the Si (3, 4). A feedback circuit is used between the output of the electrometer and the 500 khz square wave

generator to control the amplitude of the square waves and keep the current in the SiO_2 constant at a value that is preset as desired. As trapping occurs, the square wave amplitude is automatically increased to compensate for the effect of the trapped charge. The square waves are interrupted periodically to measure automatically the flat band voltage as a means for monitoring the trapped charge build up in the SiO_2. In the course of a typical run 400 - 600 measurements are made. These data are fed into a computer and the results are analyzed to provide information concerning the trap cross sections and the trap densities. The computer program can resolve two different traps if their cross sections are separated by at least a factor of 2. The analysis of the results follows the same proceedure followed by DiMaria, Aitkin and Young (5). The SiO_2 current used depends on the cross sections of interest and in this particular experiment the range was 9×10^{-10} to 9×10^{-9} A. The largest current is used for the small cross section traps. The change in flat band voltage is given by

$$\Delta V_{FB} = \frac{Q_I \overline{X}}{C_{ox} D_{ox}} \tag{1}$$

where C_{ox} is the SiO_2 capacity D_{ox} is the SiO_2 thickness, Q_I is the trapped charge and $\overline{X}$ is the centroid of the trapped charge as measured with respect to the Al-SiO_2 interface. The flat band voltage measurement does not enable us to determine Q_I and $\overline{X}$ independently and as a result we refer to an effective charge given by

$$Q_F = \frac{Q_I \overline{X}}{D_{ox}} \tag{2}$$

Ning (6) has shown that these considerations do not effect our measurements of the trap cross sections.

We obtain the cross sections and the effective trap densities by fitting exponentials to our data. The cross section is given by

$$\delta = \frac{q}{\tau I} \tag{3}$$

where τ is the time constant of the exponential, I is the current density and q is the charge on the electron.

The magnitude of the exponentials gives us the effective density of the traps. The charge centroid correction must be used to obtain the actual density.

The implanted Al profiles have been calculated using the LSS range statistics of Gibbons, Johnson and Mybroie (7). Their data have been corrected for the lower density of our SiO_2 as compared with fused silica. The factor used is .84. These profile calculations are shown in fig. 1. It can be seen that for our thinnest sample (D_{ox}=490 Å) penetration of the Al into the Si should be appreciable for an implantation energy of 20 keV. Results are presented indicating that substantial penetration actually occurs even for the 15 keV implantation.

If we substitute the expression for the SiO_2 capacity into eq. 1 we obtain for the flat band voltage shift

$$V_{FB} = \frac{Q_I \overline{X}}{\varepsilon_{ox}} \tag{4}$$

where ε_{ox} is the dielectric constant of SiO_2. This relationship is independent of D_{ox} and thus we see that V_{FB} should not depend on D_{ox} if Q_I and $\overline{X}$ are independent of D_{ox}. We assume that this is the case if the implanted Al does not reach the Si-SiO_2 interface.

C. *Experimental Results*

We have compared our trapping results on implanted samples with non implanted, but otherwise identical, samples and we find a large increase in the trapping rate, indicating that we can neglect the graps present in the non-implanted SiO_2.

The experimental results are given in fig. 2 for D_{ox} = 1400 Å, fig. 3 for D_{ox} = 730 Å and fig. 4 for D_{ox} = 490 Å. In the case of fig. 2 (1400 Å) we see a large increase in the trapping (ΔV_{FB}) as the implantation energy increases, a significant but smaller increase is noted in fig. 3

(730 Å) and in fig. 4 (490 Å), it is seen that the trapping actually decreases for implantation energies above 20 keV. The change in these results with D_{ox} is due to the penetration of the Al into the Si. This is shown by fig. 5 where ΔV_{FB} is seen to be a function of D_{ox} and not independent of D_{ox} as predicted by eq. 4. This penetration occurs for D_{ox} = 730 Å at 30 keV.

The large increase in trapping with the implantation energy (V_I) shown by fig. 2 (D_{ox} = 1400 Å) is a surprising result. The average shift $(\Delta V_{FB})AVG$ taken from these data is plotted as a function of implantation energy (VI) on a log-log plot in fig. 6 and we see that the slope is 2 indicating that the trapping varies as V_I^2. The increase in the charge centroid ($\overline{X}$) has been shown by DiMaria to be proportional to V_I and our result can not be explained solely on this basis.

A summary of the measured trap densities and cross sections is given in Table I. The total effective trap concentration observed is 3.5×10^{12}. The charge centroid measurments of DiMaria et al. indicate the $\overline{X}/D_{ox}$ = .44 for this case. Using this correction results in an actual trap density of 8.33×19^{12} as compared with the implanted fluence of 1×10^{13}.

III. Discussion of Results

Our results for the thick SiO_2 (D_{ox} = 1400 Å) which does not allow penetration of the Al through the SiO_2 into the Si shows that the trapping varies as the square of the implantation energy. The charge centroid measurements suggest a first power dependence. As a result, we conclude that the number of traps is proportional to the implantation energy. This leads to the conclusion that the trapping we are observing is due to implantation damage in the SiO_2 even though we have annealed our samples at temperatures of 1050°C.

The trap cross sections associated with this damage have been characterized and the predominant cross sections observed are 1.26×10^{-16} and 1.40×10^{-17}.

TABLE I

Trap cross sections (σ) and effective densities (N_t) for the traps resulting from a 30 keV al implant with a fluence of 1×10^{13} At/cm^2 and $D_{ox} = 730$ Å.

σ(cm^2)	N_t(cm^{-2})
1.60×10^{-15}	4.60×10^{11}
1.26×10^{-16}	1.14×10^{12}
1.40×10^{-17}	1.40×10^{12}
1.26×10^{-18}	5.00×10^{11}

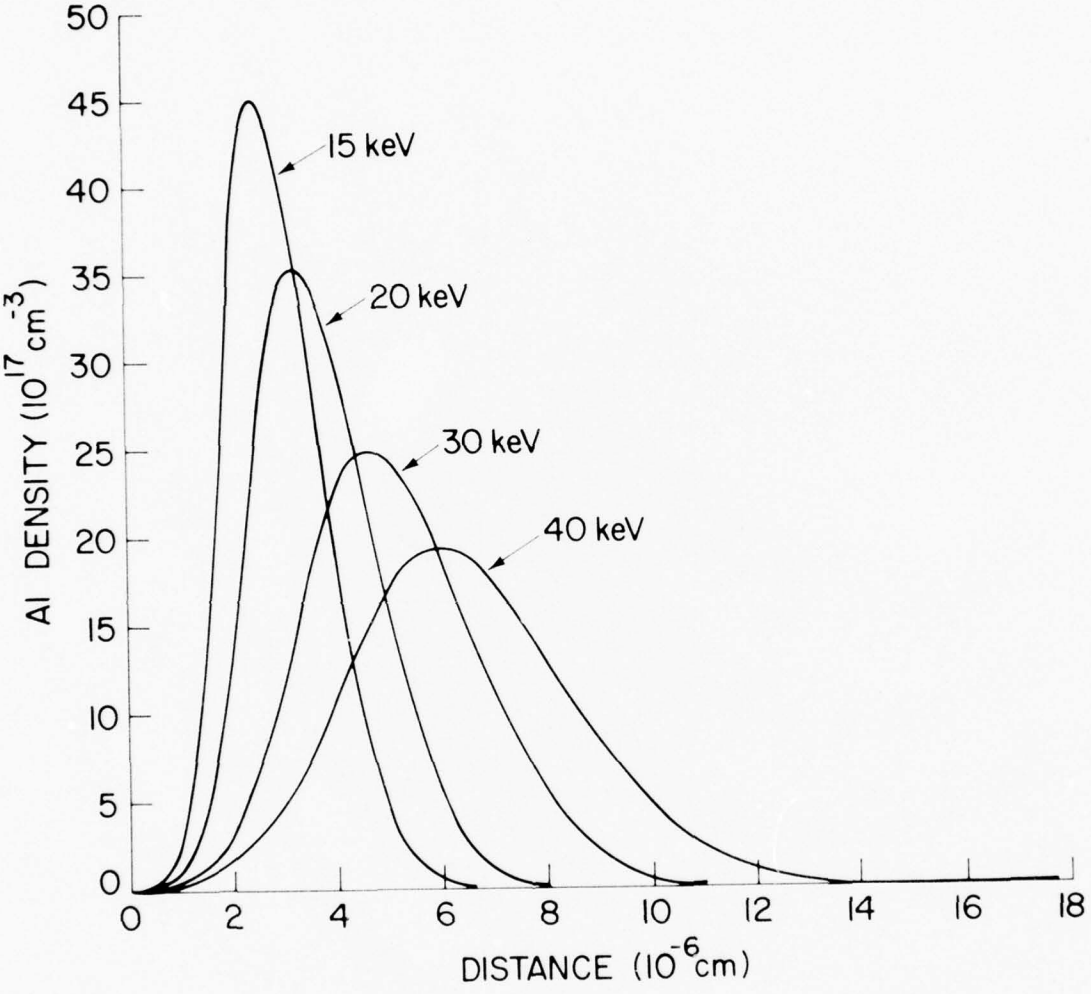

Figure 1 Aluminum concentration profiles calculated using LSS theory for various implantation energies. The fluence is 1×10^{13} at/cm^2.

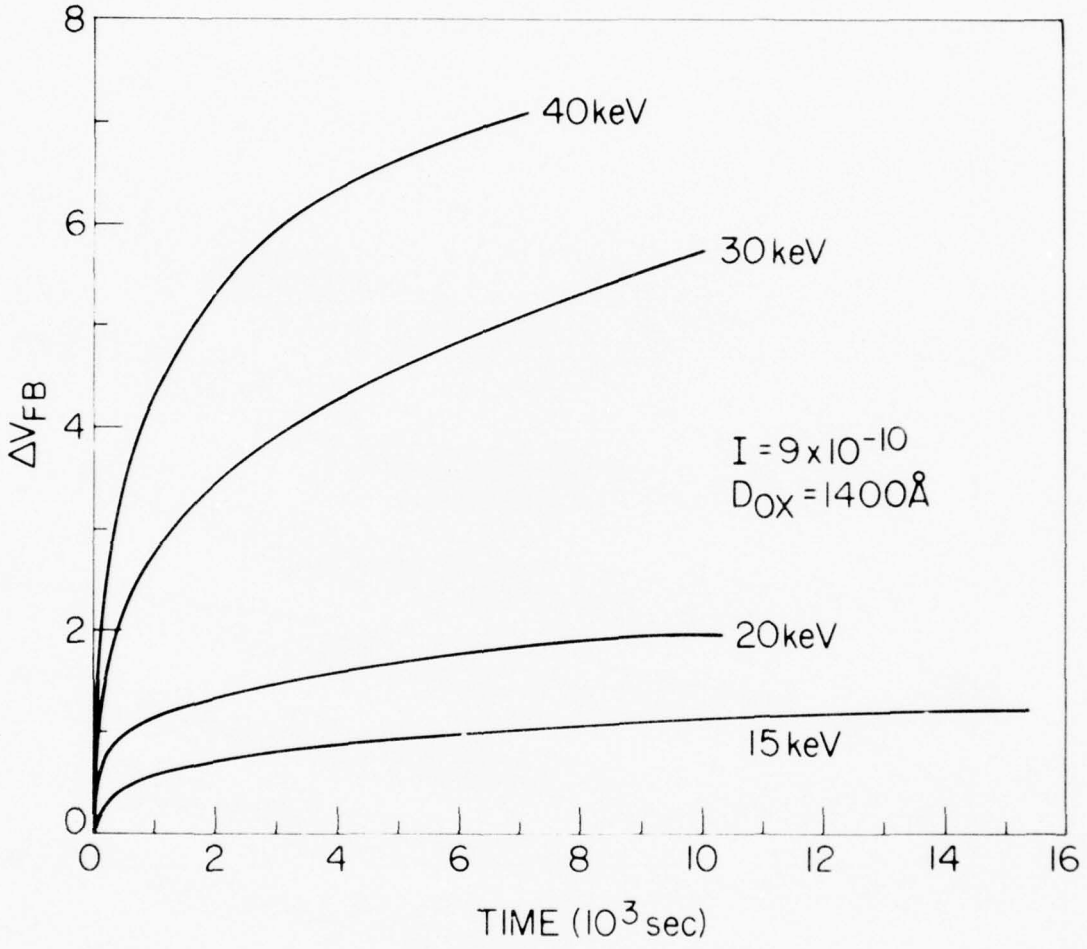

Figure 2 Flat band voltage shift as a function of time for various implantation energies.

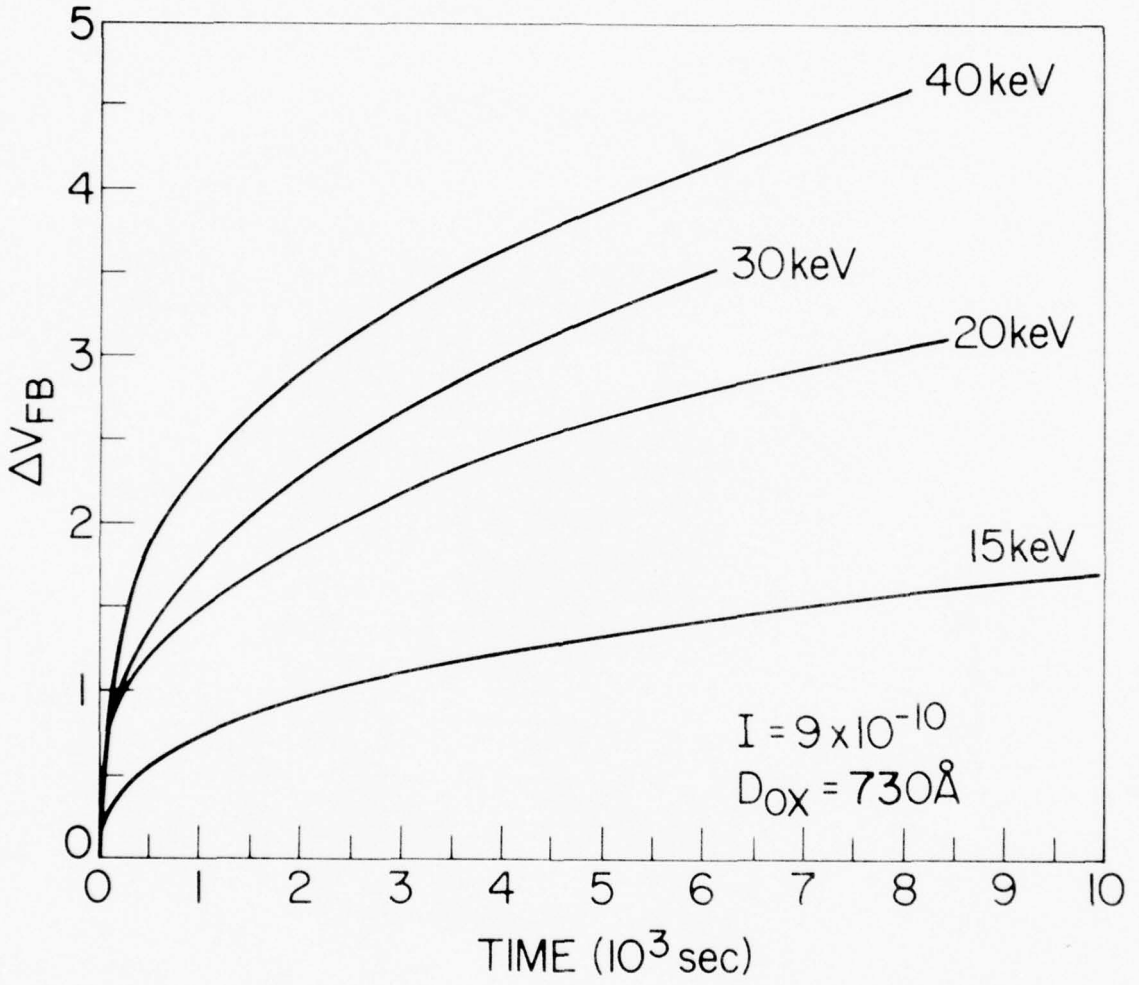

Figure 3 Flat band voltage shift as a function of time for various implantation energies.

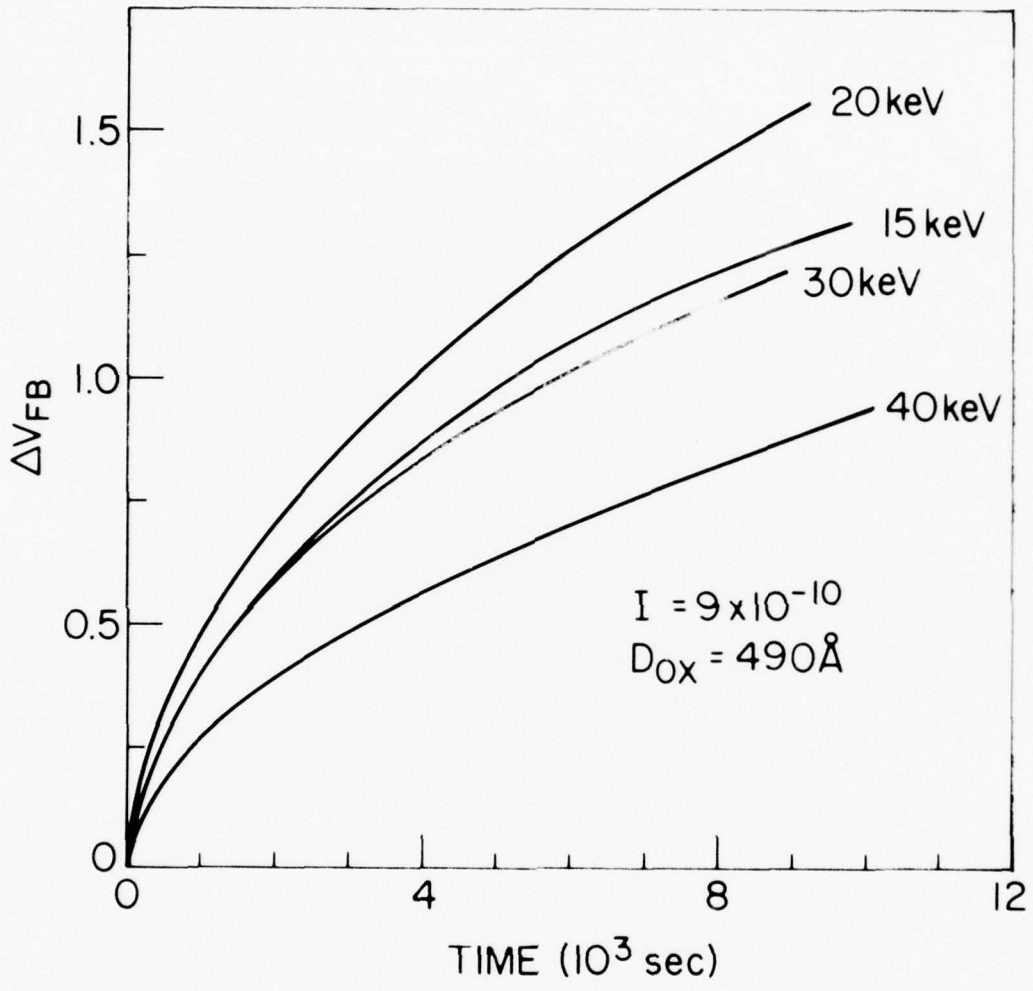

Figure 4 Flat band voltage shift as a function of time for various implantation energies.

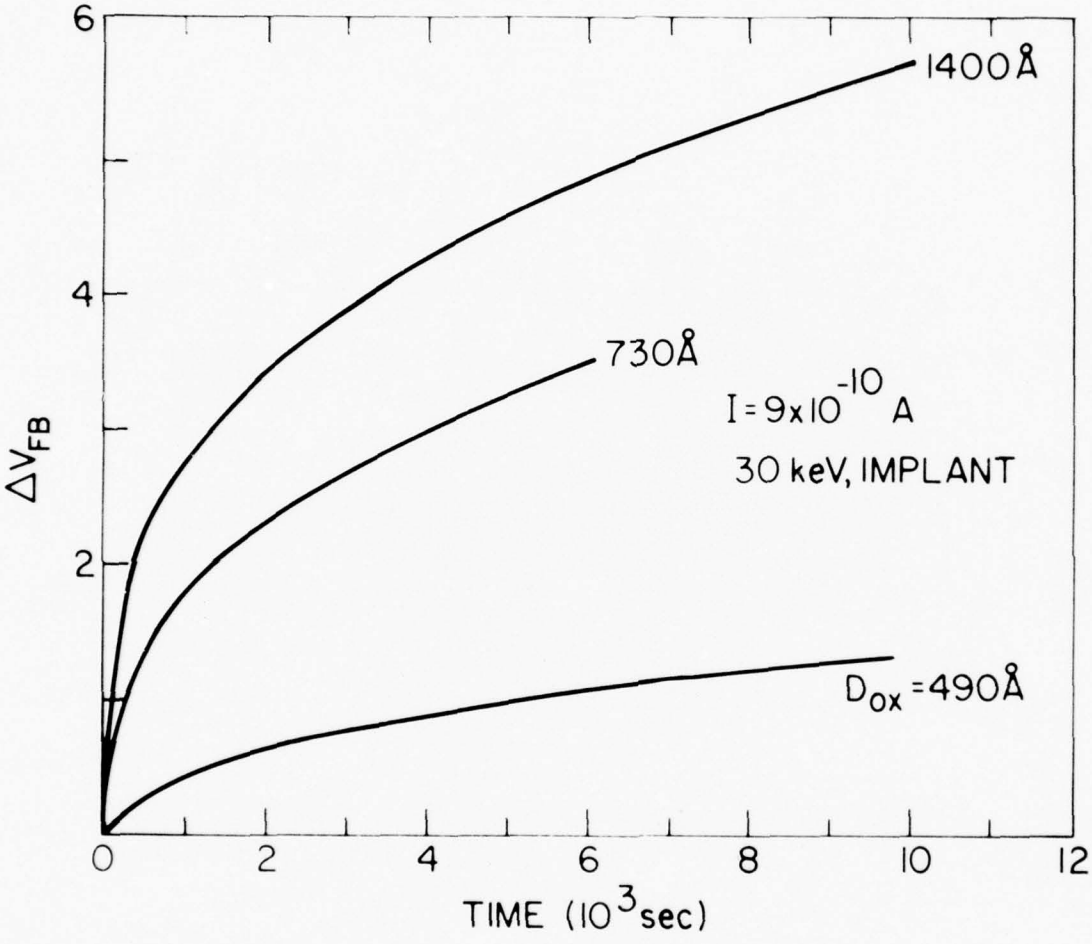

Figure 5 Flat band voltage shift as a function of time for various SiO_2 thicknesses.

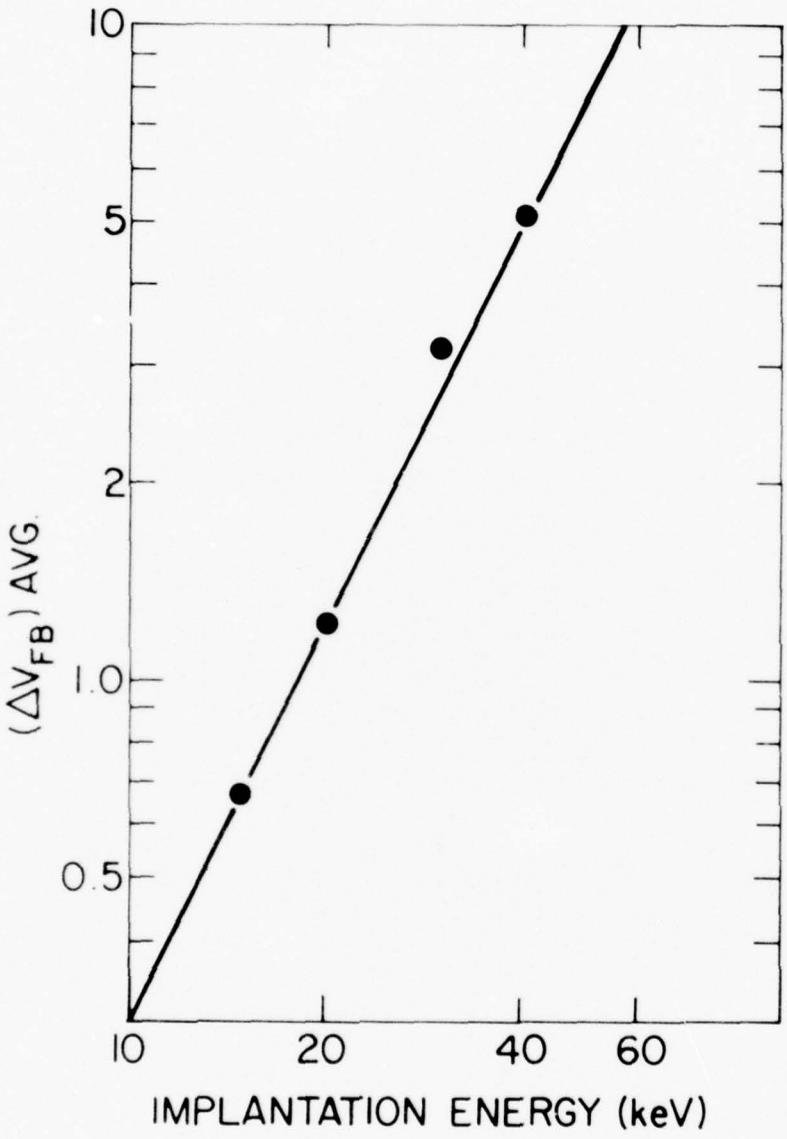

Figure 6 Log-Log plot of the average flat band voltage shift taken to 6500 sec as a function of implantation energy.

REFERENCES

1. N. M. Johnson, W. C. Johnson and M. A. Lampert, J. Appl. Phys. *46*, 1216 (1975).
2. Presented at the Electronic Materials Conference, June 1976, D. R. Young.
3. E. H. Nicollian, A. Goetzberger and C. N. Berglund, Appl. Phys. Lett. *15*, 174 (1969).
4. E. H. Nicollian and C. N. Berglund, J. Appl. Phys. *41*, 3052 (1970).
5. D. J. DiMaria, J. M. Aitken and D. R. Young, J. Appl. Phys. *47*, 2740 (1976).
6. T. H. Ning and H. N. Yu, J. Appl. Phys. *45*, 5373 (1974).
7. Projected Range Statistics Semiconductors and Related Materials, 2nd Edition, J. F. Gibbons, W. S. Johnson, and S. W. Mybroie, Halstead Press, John Wiley and Sons (1975).

ALUMINUM IMPLANTED INTO THE SiO_2 LAYER OF MOS STRUCTURES

D. J. DiMaria, D. R. Young, W. R. Hunter, and C. M. Serrano

The centroid of trapped electronic charge resulting from traps introduced by Al implanted into the SiO_2 layer of metal-oxide-semiconductor (MOS) structures has been investigated using the photo I-V technique developed by DiMaria (1). The technique has a sensitivity of less than 10^{11} charges/cm^2.

The Al implanted MOS structures are in a net neutral charge state after the processing described previously. To use the photo I-V technique which depends on the internal fields due to trapped insulator charge, the traps in the SiO_2 layer must be charged. This is accomplished by injecting electrons using avalanche of the Si substrate (2) or internal photoemission (3) from either the Si or semi-transparent metal contacts. As described previously, some of these electrons are trapped on sites related to the implanted Al. Without the implanted Al, no noticeable election trapping is seen under similar injection conditions.

In Figure 1, the centroid measured from the metal-oxide interface ($\bar{x}$) is plotted as a function of Al implant energy in the range of 15-40 keV for oxides with thickness of 490 Å, 730 Å, and 1400 Å. The points in the figures are deduced from the photo I-V experimental technique while the lines are calculated using LSS theory (4). Each experimental point in Figure 1 represents the average of $\bar{x}$ over many samples. For all samples in Figure 1, the fluence was 1×10^{13} Al/cm^2 and the post-implant annealing was carried out at 1050°C for 30 minutes in N_2. As seen in this figure there is fair agreement between the experimental results and LSS theory for all energies and oxide thicknesses (the photo I-V results show the centroid closer to the Al except for $\bar{x}$ at 15 keV on the 730 Å and 1400 Å samples). The roll-off of $\bar{x}$ at higher implantation energies on the thinner samples (730 Å and 490 Å) is due to significant amounts of Al penetrating into the Si substrate which are not sensed with the photo I-V

technique. On the 490 Å sample, a significant amount of Al is lost to the Si substrate for all energies from 15 - 40 keV.

The photo I-V experiments presumably sensed negative charge trapped on sites related to the implanted Al. SIMS measurements done in conjunction with F. W. Anderson (IBM - E. Fishkill) have shown that the centroid and distribution of the implanted Al and the negative trapped charge are identical within measurement error for a 20 keV Al implant into a 770 Å SiO_2 film at a fluence of $1 \times 10^{13} cm^{-2}$. This can be seen from values of $\bar{x}$ for the implanted Al deduced from the SIMS data of Fig. 2 which are 346 Å and 274 Å for 730 Å and 490 Å oxide thicknesses, respectively. These SIMS measurements also have shown that the profile of the implanted Al is not a measurable function of post-implant annealing conditions (unannealed as compared to a 1050°C anneal in N_2 for 30 min).

Figure 2 also shows a profile of the implanted Al predicted from LSS theory. As seen in this figure the SIMS profile is broader than the LSS calculation predicts even though the centroids are almost identical for a 770 Å thick oxide. This implies that more Al should be lost to the Si substrate on thinner SiO_2 samples and predicts that the measured values of $\bar{x}$ using the photo I-V technique should progressively deviate more with the LSS calculations as the oxide is made thinner. The former trend is consistent with the calculated (LSS) roll-off of $\bar{x}$ occurring at higher implantation energies than seen experimentally in Figure 1. The latter trend is consistent with the results of Figure 1 and Figure 2 where the largest deviations with theory for all energies are found on the MOS structure with the 490 Å thick SiO_2 layer.

The centroids of the negative trapped charge were found largely to be independent of the following experimental variables:

1. *Amount of Trapped Charge* - in the range from 10^{11} to 10^{12} electrons/cm^2.
2. *Injection Mechanism* - avalanche or internal photoemission from the Si substrate, or internal photoemission from the Al electrode; except for a small anomolous effect observed for the sample with a 40 keV implant into a 1400 Å oxide.

3. *Post-implant Annealing Conditions* - from 600°C to 1050°C for 1/2 hour in N_2.

4. *Fluence of Al* - from 5×10^{12} to 2×10^{13} Al/cm^2.

5. *Oxide Thickness* - in the range of 490 Å to 1400 Å if the Al does not penetrate into the Si substrate.

REFERENCES

1. D. J. DiMaria, J. Appl. Phys. *47*, 4073 (1976).

2. E. H. Nicollian, A. Goetzberger, and C. N. Bergland, Appl. Phys. Lett. *15*, 174 (1969); E. H. Nicollian and C. N. Bergland, J. Appl. Phys. *41*, 3052 (1970).

3. B. E. Deal, E. H. Snow, and C. A. Mead, J. Phys. Chem. Solids *27*, 1973 (1966).

4. J. F. Gibbons, W. S. Johnson, and S. W. Mylroie, *Projected Range Statistics of Semiconductors and Related Materials*, 2nd edition (Halstead Press, John Wiley and Sons, 1975). In our calculations (see lines in Fig. 1), we corrected for the difference in density between fused quartz (listed in the tables) and the thermal SiO_2 studied here. This ratio (thermal SiO_2 density to fused quartz density) was .84.

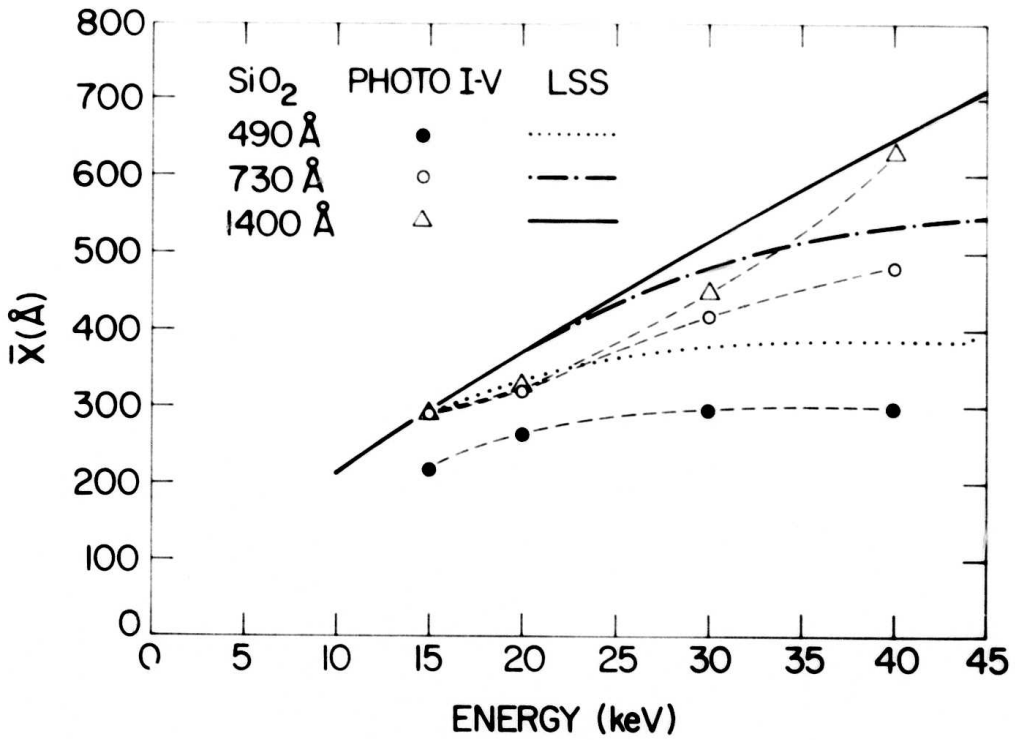

Figure 1 $\bar{x}$ as a function of Al implantation energy from 15-40 keV for 490 Å, 730 Å, and 1400 Å thick SiO_2 layers. The points •, o, and Δ are experimental values for the trapped negative charge distribution using the photo I-V technique and the lines ••••, •-•-•, and ——— are the values predicted by LSS theory for the implanted Al distribution. All samples were charged by avalanche injection of electrons from the Si substrate.

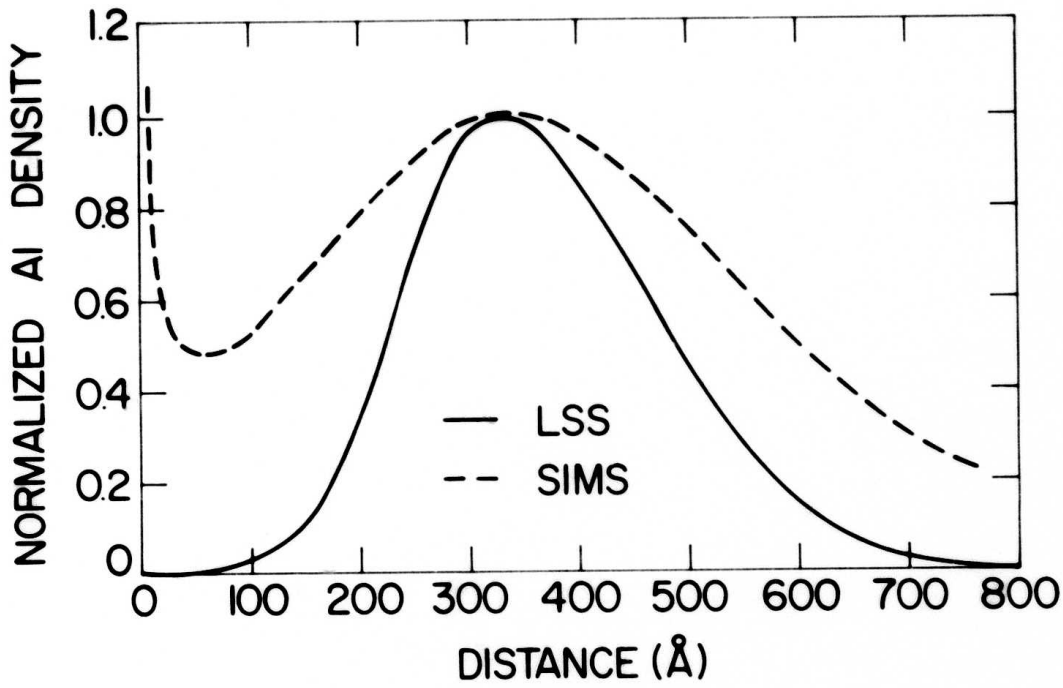

Figure 2 Normalized Al density for a 20 keV implant energy and 1 x 10^{13} cm^{-2} fluence as a function of distance from the air-oxide interface into a 770 Å thick SiO_2 film. The normalization factor was the peak value of the Al density in the film. The dashed and solid lines are the profiles determined from SIMS measurements and LSS theory with centroids of 353 Å and 368 Å respectively for an oxide thickness of 770 Å.

SILICON OXIDATION STUDIES: THE INITIAL OXIDATION REGIME

G. Irene

The thermal oxidation of single crystal silicon at high temperatures (800-1000°C) in pure dry 0_2 has been found to be represented adequately by a linear-parabolic film growth model (1), with an accuracy better than 10 percent, so long as the data fitted includes film thicknesses greater than a minimum value (d_0) of about 200Å.[2] However, for oxidations in H_20 containing ambients (3,4), the minimum thickness value, d_0, to be included for a good fit to the linear-parabolic model, decreases with increasing H_20 content of the oxidizing ambient. An examination of the regime of thicknesses less than d_0, shows that this thin $Si0_2$ region is characterized by a faster rate of oxidation than is anticipated from the rate constants for the linear-parabolic regime (1-5). One report (5) describes this region by another linear-parabolic equation while other authors (6,7) assume it is the linear part of the linear-parabolic rate law. The former analysis (5) does not consider the possible error associated with assuming a linear-parabolic initial regime and the latter authors have insufficient data to analyze for the determination of a best fit. The present study is concerned with an examination of the initial regime of oxidation ($Si0_2$ film thicknesses $\leq d_o$ to determine why the initial regime for dry 0_2 oxidation displays a more rapid oxidation mechanism while for H_20 oxidation $d_0 \approx 0$, and the oxidation data follows the linear parabolic model throughout.

In the present study, it was found that there was a decided difference between the linearity of the data for dry 0_2 oxidation and oxidation in a H_20 containing ambient for $Si0_2$ films up to 200 Å thickness. The dry 0_2 data were more linear. The linear-parabolic model (1) can be summarized by the integrated rate equation:

$$t-t_o = \frac{1}{k_{LIN}} (d-d_o) + \frac{1}{k_{PAR}} (d^2-d_o)$$

where t and d are the time of oxidation and $Si0_2$ film thickness respectively t_o and d_o represent the upper bound of the initial oxidation regime which does not conform to linear-parabolic kinetics and k_{LIN} and k_{PAR} are the linear and parabolic rate constants respectively. In this model, linear kinetics are the result of a surface controlled reaction while parabolic kinetics

demonstrate that the oxidation is diffusion controlled. This experimental finding suggested that wet grown SiO_2 films are more protective. Dielectric breakdown histograms support the contention that 150Å wet grown SiO_2 films have less defects than films grown in dry O_2. These results can be explained if micropores existed in the SiO_2 films. For the purpose of observing micropores in the films, transmission electron microscopy (TEM) studies were performed.

Experimental Procedures

Substrate Preparation and Oxidation

The oxidation experiments were performed using an automated ellipsometer capable of measuring the SiO_2 film thickness in-situ during oxidation. The instrument used for this study has been described in detail elsewhere (8). Basically, the ellipsometer uses a laser light source, polarizer, compensator, and a rotating analyzer-encoder. The light intensity measurement after the analyzer is automated. The ellipsometry measurements are made with the sample contained in a fused silica rf-heated reaction tube. Therefore, it is possible to collect and analyze ellipsometric data as the SiO_2 film grows without interrupting the oxidation run. The optical constants characteristic of the Si surface as a function of temperature were previously measured (8).

All substrates were <100> oriented chem-mechanically polished silicon wafers measuring 3.2 cm in diameter and 0.025 cm in thickness. All the wafers were p-type with a nominal resistivity of 2 ohm-cm. It was reported previously (3) that the resistivity type or value in the range 0.5-10 ohm-cm had no influence on the oxidation process. The wafers were cleaned as reported elsewhere (3) and an initial oxide thickness of 3 to 6Å SiO_2 was measured at room temperature.

The gases used in this study included Ar, N_2 and O_2. Both N_2 and O_2 were supplied from boil-off of liquid sources. As previously reported (2,3) the O_2 contained trace amounts of methane (17 ppm) which at the experimental oxidation temperature combusts to form H_2O. This trace H_2O substantially increases the rate of oxidation (3,4). For dry oxidations, the

methane was removed by preheating the oxygen to about 1000°C, in order to combust the methane to H_2O and CO_2, and then cold trapping at -80°C to reduce the H_2O concentration to less than 1ppm H_2O in the O_2. To add H_2O to N_2, the N_2 is flowed through a thoroughly cleaned fused silica vessel which contains deionized H_2O. By controlling the H_2O temperature with a variable temperature refrigeration unit the concentration of H_2O can be adjusted to any desired level from less than 1 ppm upwards. The Ar was purchased in pressurized cylinders and was the highest purity available. The moisture content was less than 0.5 ppm as measured at the furnace exit during the actual annealing experiments to be described.

In order to check on the charge levels in the SiO_2 film grown, capacitance-voltage (C-V) measurements were made on some oxides. Evaporated aluminum counter-electrodes were used as electrical contacts. The C-V measurements at (1MHz) revealed an average fixed positive charge level of 5×10^{10} charges/cm^2. Bias-temperature stressing (10^6V/cm at 200°C for 15 min and subsequent cooling under bias) revealed an average mobile positive charge level of 7×10^{10} charges/cm^2. These values are characteristic of MOS quality oxide.

Dielectric Breakdown Measurements

Dielectric breakdown measurements were made using a special triggering circuit configuration previously described by Osburn and Ormund (9). Essentially a linear voltage ramp is applied to the MOS sample. The voltage ramp was obtained by charging a fixed capacitor using a constant current generator; the ramp rate was then controlled by adjusting the output current from the generator. Triggering is obtained by a circuit which senses a voltage across a resistor in series with the MOS device. The series resistor must be kept at a reasonably low value (10-1000 ohms) to prevent a large error in the reading of the final breakdown voltage. The electrodes used were RF evaporated Al dots of 0.127 cm diameter yielding a dot area of 1.27×10^{-2}cm^2. These larger dot sizes were used to obtain more realistic breakdown histograms. The Al thickness was approximately 5000Å and this thickness plus the use of a small

sense resistor in the circuit configuration (9) insured that the measured breakdown voltage was the final destructive breakdown. The ramp rate was the same for all measurements and about 0.5 MV/cm-sec.

The breakdown measurements were done with the Al biased negatively, i.e., with the 2Ω-cm p-type Si in accumulation. At high fields electrons are injected from the Al into the SiO_2. If electrons were trapped at or near the Al-SiO_2 interface, the trapped charge would alter the field across the MOS device and possibly lead to erroneous conclusions concerning histograms of the number of breakdown events versus applied field. For the purpose of determining if there is sufficient trapping at or near the Al-SiO_2 (injecting) interface a recently described (10) technique using Fowler-Nordheim (FN) current is used. The FN technique consists of a measurement of current while applying a voltage ramp. The FN current regime is identified by the linearity of the plot of log I versus E. The fields at which the FN conduction mechanism dominates is usually greater than 6 MV/cm for SiO_2. If trapping occurs, the FN curve would be shifted to higher fields due to trapped negative charge. Trapped charge causes field reduction, F, at the cathode according to the equation (10):

$$F = \frac{q N_t \overline{X}}{\varepsilon_{ox} D_{ox}}$$

where q is the electronic charge, N_t is the total trap concentration, and ε_{ox} is the dielectric constant for SiO_2, X is the distance of the centroid of the charge from the anode and D_{ox} is the oxide thickness. This means that the effect of the charge on the field at the cathode increases as the distance to the cathode decreases. Experimentally the current through the MOS device is measured using a logarithmic picoammeter while the field is increased by means of a linear ramp. The FN regime is scanned in field from about 6 - 10 MV/cm and then held at 10 MV/cm for a few seconds to insure large current flow through the device; then the field is removed and the experiment repeated. If trapping occured the FN characteristic curve would be shifted to higher fields. Results of this experiment will be shown below.

Capacitance - voltage measurements (1 MHz) at room and LN_2 temperatures were made to determine whether charges were trapped, and/or surface states (11, 12) created, at or near the Si-SiO_2 interface due to the large currents which exist prior to dielectric breakdown.

Transmission Electron Microscopy (TEM)

Specimens of 150Å SiO_2 films were prepared by chemically etching away the Si from the Si-SiO_2 composites. The details of this procedure have been previously described (13). The preparation was done in four different ways, in order to eliminate possible artifacts due to a particular etchant, and to decorate features of interest. Type I samples were prepared by simply etching away Si with a mixture of HF and HNO_3. This etchant also vigorously attacks SiO_2 and the successful preparation of samples with this etchant is somewhat fortuitous. When the Si-SiO_2 interface is approached, the etchant mixture is changed to a solution more dilute in HF, in order to reduce the speed of attack on the SiO_2 film. Type II samples were prepared similarly to Type I except that when about 80 percent of the Si was removed with a HF-HNO_3 etchant, the etchant was changed to a mixture of pryocatechol-ethylenediamine-H_2O (14). This mixture attacks Si very vigorously (20μ/hr at 100°C) but SiO_2 very slowly (200Å/hr). Type III films were prepared exactly as Type II and when etching was finished were annealed in dry N_2 at 1000°C for 2 hs. This treatment was used to simulate an observed degradation in dielectric reliability to be reported later. Type IV samples were prepared as Type II samples but before etching they were either coated with 100Å of Au by evaporation or dipped in a solution of NaCl and annealed. The Au samples were annealed for 1/2 hr at 800°C and the NaCl contaminated samples were heated for 1 hr at 500°C. In some cases the Au coated samples were not annealed and in other cases the Au was removed after annealing with aqua-regia. It was hoped that the Au would decorate preferred diffusion paths and the NaCl would decorate weak areas by reaction.

EXPERIMENTAL RESULTS

Fig. 1 shows the experimental data for the oxidation of <100> Si in dry O_2 and H_2O-N_2 ambients for SiO_2 film thicknesses of 20 - 150Å. Visually these data appear to be linear. Table I shows the results of fitting the data to the linear equation:

$$t = k_1 d + k_2$$

by the method of least squares (15) where t is the oxidation time, and d is the SiO_2 thickness. The dry O_2 data is relatively more linear than the H_2O-N_2 data. Indeed it is known that for a 2000 ppm H_2O in N_2 ambient $d_0 \approx 0$, hence the data fits the linear-parabolic equation for all values of SiO_2 film thickness (4) while for dry O_2 a best fit is not obtained when film thicknesses less than ~200Å are included in the analysis. In keeping with the linear-parabolic model (1), the linear rate is associated with a surface controlled reaction. This plus the fact that the initial linear regime for dry O_2 displays a greater oxidation rate than the linear-parabolic mode, suggests that the SiO_2 films produced by ultra dry O_2 oxidation are less protective than films grown in an H_2O containing ambient. Enhanced protectivity for the H_2O grown 150Å films may be manifested in terms of reduced film defects. The results of dielectric breakdown measurements to be described can be interpreted in terms of film defects and will shed some light on this question of protectivity.

The difference in linearity of the oxidation data for wet and dry grown films is largest at the lower oxidation temperatures; and at the lower temperatures there is closer agreement between the slope of the straight line fitted to the data and the linear rate constant as obtained from the linear-parabolic model applied to film thicknesses up to 2000Å (2). For dry O_2 grown oxides this is understood by considering that the initial regime for dry O_2 films is not linear-parabolic and therefore agreement between k_{LIN} and k_1 is not to be expected except where d_o is close to zero at the lower temperatures. For the H_2O grown films the parabolic rate constant is important even for these thin films and therefore agreement between k_{LIN} and k_1 will depend on the importance of k_{PAR}.

The shape of the histogram of the number of dielectric breakdown events versus the field at which breakdown occurs yields information relative to the defects in the SiO_2 films (9, 16). Fig. 2 shows a comparison of the histograms for 150Å SiO_2 films grown in H_2O-N_2 (2a) and dry O_2 (2b). It is readily seen that the maximum breakdown field for both wet and dry SiO_2 are nearly equivalent at a value of 14 MV/cm yet the shapes of the distributions are decidedly different. Theoretically, the histogram for a defect free SiO_2 film would be a delta function at the maximum breakdown field. Thickness fluctuations as well as random measuring equipment imperfections would broaden the delta function slightly, but SiO_2 film defects would cause a larger tail toward the lower fields. This type of tailing is observed in the histograms for both wet and dry grown SiO_2. However, the broadening is more severe for the dry oxides where the peak in the distribution is shifted some 2-3 MV/cm further toward low fields than for wet grown oxides and results in a distribution with a nearly Gaussian shape. The wet grown SiO_2 films have 80 percent of the breakdowns at field $\geq$10MV/cm while only 30 percent for dry grown films. Therefore, in view of these dielectric breakdown results the previous assertion based on the film growth kinetics that wet grown oxides are more protective seems justified.

Previously, it was reported that the effect of H_2O on the SiO_2 film oxidation kinetics is reversible (4), i.e., the oxidation kinetics of an oxide growing in an H_2O containing ambient reverts to dry oxidation kinetics soon after the wet ambient is switched to a dry ambient. It is worthwhile to investigate whether the enhanced dielectric reliability of the wet grown thin SiO_2 films is coupled with the rather labile-OH in which case the enhanced dielectric integrity is easily lost or whether the enhanced reliability is due to a more stable form of OH in the SiO_2 network. Fig. 3a shows that the histogram for a wet grown oxide reverts to that for a dry grown oxide after 1/2 hr 1000°C anneal in dry N_2. However, Fig. 3b, c, and d show that compared with the control (3b) annealing at 1000°C in dry Ar for up to 18 hrs. caused only a small amount of degradation. In fact, the small amount of degradation could simply be due to

sample to sample variations. In any case, the degradation in dry N_2 is unambiguously larger. Therefore, since the films were stable to the 1000°C Ar anneal, the enhanced reliability of wet grown thin oxides appears to be related to a stable form of OH in the SiO_2. The fact that there exists several forms of OH having different lability in fused silica has been reported (17). Also the reactivity of N_2 in the SiO_2-Si system in a non-oxidizing atmosphere has been reported (18) as well as the detrimental affect that the reaction of N_2 has on the dielectric reliability (19, 20). Thus, the degradation of the H_2O grown thin films is accelerated by N_2 reaction and not by the out diffusion of labile OH.

Electron Trapping and Surface States

Representative results for the electron trapping measurements by the previously described Fowler-Nordheim (FN) technique are shown in Fig. 4. The samples were ramped up to 10.5 MV/cm and held there for 10 sec (i). Then the curve was retraced (re). The initial and retraced curves for a wet grown oxide (W104) differ at most by 0.5 MV/cm shift in the breakdown histogram peaks. Samples W104 and D113 displayed more than the average amount of trapping for wet and dry samples examined in this study; the average shift in the FN characteristic curve was found to be 0.2 - 0.3 MV/cm for both wet and dry samples with wet grown films usually exhibiting more trapping. It was sometimes difficult to find dots on dry grown SiO_2 samples which could withstand the high field for this experiment. Other than this problem, however, the trapping behavior at or near the cathode was observed to be similar for wet and dry films and in no case was the trapping sufficient to cause the degree of electric field change necessary to explain the histograms of Fig. 2.

Capacitance-Voltage (CV) measurements at room temperature and liquid nitrogen temperature have shown that about 7.5×10^{11} positive charges per cm^2 are created at or near the Si-SiO_2 interface and about the same number of surface states are created by virtue of the above described FN currents. These results were the same for both dry and wet grown oxides and are in qualitative agreement with previous studies (see, for example, Refs. 21 thru 24).

Fig. 5 shows representative results from Type I and II samples. The results from Type I, II, dry and wet samples were substantially the same. It is seen from Fig. 5 that the mode for the dissolution of the films is via attack by the etchant at selected small areas on the film surface. The differences seen between 5a and b is probably due to the time of exposure of the film to etchant. The time duration in which the sample was exposed to etchant would determine the size relationship between the final size of the hole and the original defect. This time was not controlled in this study. The nature of the defect, i.e., whether a void, micropore, impurity cluster, crystallite, etc. depends on the relative reactivity of the etchant to these type of possible defects. It is clear that a void or micropore could yield the final observation, but other defects cannot be ruled out. The maximum size of inhomogeneity must be as small or smaller than the hole found after etching. Holes which measured less than 100Å were observed, and therefore, considering the speed of the etchants, the inhomogeneities could be 50Å or less in diameter. No differences were seen upon annealing Type I and II samples. Therefore, no figure for Type III samples is shown.

By way of explaining these results, gas permeation studies (25) have led to the assertion that pores in SiO_2 of less than 50Å diameter would explain the measured permeabilities for different gases. Another model was proposed (26) in which a non-random distribution of bond angles in the SiO_2 network may result in chain-like defects where $d\pi$-$p\pi$ orbital overlap between Si and O is greater than in surrounding regions. Such higher density regions may be more violently attacked by etchant. This latter model (26) predicts higher conductivities for films which have this chain structure. However, the conduction measurements made in the present study do not show any systematic differences between wet and dry prepared 150Å SiO_2 films. Also, it is difficult to reconcile the oxidation kinetics results based on more dense localized regions.

Representative results from Type IV samples are shown in Fig. 6. Fig. 6a shows that less than a monolayer of Au forms rod shaped structures. A closer examination reveals that contained within the rod like structures are smaller darker regions. Presumably these are the nuclei for the growth of the Au islands. The area density of these nuclei ($\sim 10^{15}$ cm^{-2}) is much larger than the electrically active defect density ($<10^{3}$) as obtained by dielectric breakdown measurements. Fig. 6b shows the results from Au decoration. Au was evaporated into a 150Å SiO_2 film on Si. The Si was removed from a portion of the sample and then the Au was driven into the film at 800°C for 1/2 hr. The Au was then removed using aqua-regia. The darker transparent region of 6b was caused by a piece of the film folding back to the silicon edge and then breaking off. Therefore, there is 300Å SiO_2 in the darker region. All the Au has not been removed and is seen as the non-transparent dots and islands formed by coalescence and growth. The regions where the Au has been removed appear as tunnels. However, it is known that Au reacts with SiO_2 (27) and the shape of the tunnel like structures is similar to the shape of the Au islands. Therefore, it is believed that the tunnel-like structures are due to reaction of Au with SiO_2. Furthermore, if the Au is removed after a 300°C anneal or no anneal at all, the tunnel structures are less visible.

Fig. 6c shows the result of decoration with NaCl. The NaCl nuclei appear to be located preferentially on the perimeter of holes which were produced by the etchant. Also, around the NaCl nuclei and clusters is another dark band. This is probably a region in which reaction has taken place between Na and SiO_2. The holes may have been preceeded by areas which were the reaction product of NaCl and SiO_2 and this may be more vigorously attacked by the etchant. Sodium silicates are usually soluble in H_2O. The shapes of the holes are irregular as compared with the circular holes which occurred without attempts at decoration.

There are several things learned from the TEM experiments. The Type I and II samples strongly suggest that the films have inhomogeneities. The size of the inhomogeneities is certainly less than 100Å and probably less than 20Å which makes the resolution of the defects

within the present study doubtful. The number of these inhomogeneities, assuming that they are related to the etched holes in a one to one ratio, is of the order of $10^{15}cm^{-2}$ which is more than 10^{12} times too large compared with the number of defects obtained from dielectric breakdown statistics. This probably means that although the type of inhomogeneity observed is part of the SiO_2 thin film structure, only a small fraction are sufficiently electrically active to cause dielectric failure. The shape of defects was not obtained by decoration experiments because ambiguities arise from the reaction of the decorant with SiO_2. However, the number of nuclei of Au and NaCl is roughly the same as the number of holes observed from etching. This may mean that the decorants did indeed decorate the defects but also simultaneously obscured their shapes by reaction.

Summary and Discussion

The kinetic oxidation data suggest that the wet grown thin (~150Å) oxides are more protective than ultra dry O_2 grown films. The evidence for this is the greater linearity of the thickness-time data for the dry grown oxides as compared with wet grown films. The linearity suggests a surface reaction controlled mechanism for oxidation rather than diffusive transport of oxidant. In effect, for the case of ultra dry O_2 oxidation, the growing oxide film does not provide an effective barrier to the diffusion of oxidant. A comparison of the dielectric breakdown histograms for the wet and dry ~150Å SiO_2 films strongly supports the contention that the wet grown oxides are more protective. Annealing the wet grown oxides in dry Ar at 1009°C for long times does not cause degradation. Therefore, the enhanced dielectric reliability of the H_2O-grown films is due to a rather stabile OH species. The TEM experiments offer significant evidence that SiO_2 films are not homogenous and the size of the inhomogeneities is probably less than 50Å.

The experimental observations made in this study are consistent with the existence of micropores in the SiO_2 films, even though such small pores were not directly observed. Firstly, the presence of pores in solids is expected (28). The size and type of pore structure that a

material displays is dependent upon the material. Secondly, the pores would provide a "short circuit" path to the Si-SiO_2 interface for oxidant species which do not attack SiO_2 (such as O_2 related oxidant). Rapid lateral diffusion of these oxidant species would yield linear oxidation kinetics which is typical of surface controlled reactions. In addition, such pores could cause premature dielectric failure. For H_2O grown films the reactive OH attacks SiO_2 forming SiOH species. The micropores could then become partially clogged with OH groups thereby yielding parabolic oxidation kinetics and improved dielectric integrity. Thirdly, micropores are known to bind vapors tenaciously (28) in the interior of the pores thus explaining the irreversibility of the dielectric improvement even to 1000°C inert gas anneals. Further experiments would be necessary to prove the micropore model. Indirect measurements such as adsorbtion isotherm studies are usually performed to detect the existence and nature of pores (28), particularly micropores. Only a few studies have reported the direct observation of pores smaller than ~100Å and no studies have been found in the literature by this author which show the direct (TEM, SEM, etc.) observation of micropores.

TABLE I

Results of Fitting the Data from Fig. 1 to the Linear Equation, $t = k_1 d + k_2$ where t is the time (min) and d the SiO_2 film thickness (Å). D represents dry O_2 oxidation ambient and W represents 2000 ppm H_2O in N_2.

Temperature (°C)	Ambient	Std Dev of Fit	$1/k_1$ (Å/min)	k_{LIN}* (Å/min)
780	D	0.86	0.56	0.57
	W	4.0	0.1	0.10
893	D	0.40	2.8	2.2
	W	1.0	0.78	0.60
980	D	0.37	8.9	7.7
	W	1.1	3.3	4.6

* k_{LIN} from the linear - parabolic model (2)

REFERENCES

1. B. E. Deal and A. S. Grove, J. Appl. Phys., *36*, 3770 (1965).
2. E. A. Irene and Y. J. van der Meulen, J. Electrochem. Soc., *123*, 1380 (1976).
3. E. A. Irene, J. Electrochem. Soc., *121*, 1613 (1974).
4. E. A. Irene and R. Ghez, J. Electrochem. Soc., to be presented at 3rd International Silicon Symposium.
5. M. A. Hopper, R. A. Clarke, and L. Young, J. Electrochem. Soc., *122*, 1216 (1975).
6. A. G. Revesz and R. J. Evans, J. Phys. Chem. Solids, *30*, 551 (1969).
7. Y. J. van der Meulen, J. Electrochem. Soc., *119*, 530 (1972).
8. Y. J. van der Meulen and N. C. Hien, J. Opt. Soc. Am., *64*, 804 (a974).
9. C. M. Osburn and D. W. Ormond, J. Electrochem. Soc., *119*, 591 (1972).
10. P. Solomon, J. Appl. Phys., submitted for publication.
11. P. V. Gray and D. M. Brown, Appl. Phys. Letters, *8*, 31 (1966).
12. D. M. Brown and P. V. Gray, J. Electrochem. Soc., *115*, 760 (1968).
13. E. A. Irene, V. J. Silvestri and G. R. Woolhouse, J. Electronic Materials, *4*, 409 (1975).
14. R. M. Finne and D. L. Klein, J. Electrochem.Soc., *114*, 965 (1967).
15. H. D. Young, "Statistical Treatment of Experimental Data:, Chap. IV, McGraw-Hill Co., Inc., New York (1962).
16. N. J. Chou and J. M. Eldridge, J. Electrochem. Soc., *117*, 1287 (1970).
17. R. W. Lee, Phys. and Chem. of Glasses, *5*, 35 (1964).
18. S. I. Raider, R. A. Gdula and J. R. Petrak, Appl. Phys. Letters, *27*, 150 (1975).
19. B. H. Vromen, Appl. Phys. Letters, *27*, 152 (1975).
20. C. M. Osburn, D. W. Ormond, J. Electrochem. Soc., *119*, 603 (1972).
21. C. M. Osburn, and E. J. Weitzman, J. Electrochem. Soc., *119*, 603 (1972).
22. M. Shatzkes, M. Av-Ron, and R. M. Anderson, J. Appl. Phys., *45*, 2065 (1974).
23. M. Shatzkes and M. Av-Ron, J. Appl. Phys., *47*, 3192 (1976).

24. C. M. Osburn and N. J. Chou, J. Electrochem. Soc., *120*, 1377 (1973).

25. S. W. Ing, Jr., R. E. Morrison, and J. E. Sandor, J. Electrochem. Soc., *109*, 221 (1962).

26. A. G. Revesz, J. Non-Cryst. Solids, *4*, 347 (1970).

27. E. I. Alessandrini, D. R. Campbell and K. N. Tu, IBM Report RC-4844.

28. "Surface and Colloid Science", Vol. 9, Wiley, 1976, Ed. E. Matijevic Chap. 4 by S. J. Gregg and K. S. W. Sing.

29. I. U. P. A. C., Manual of Symbols and Terminology, Appendix 2, Part I, Colloid and Surface Chemistry, Pure and Applied Chem., *31*, 578 (1972).

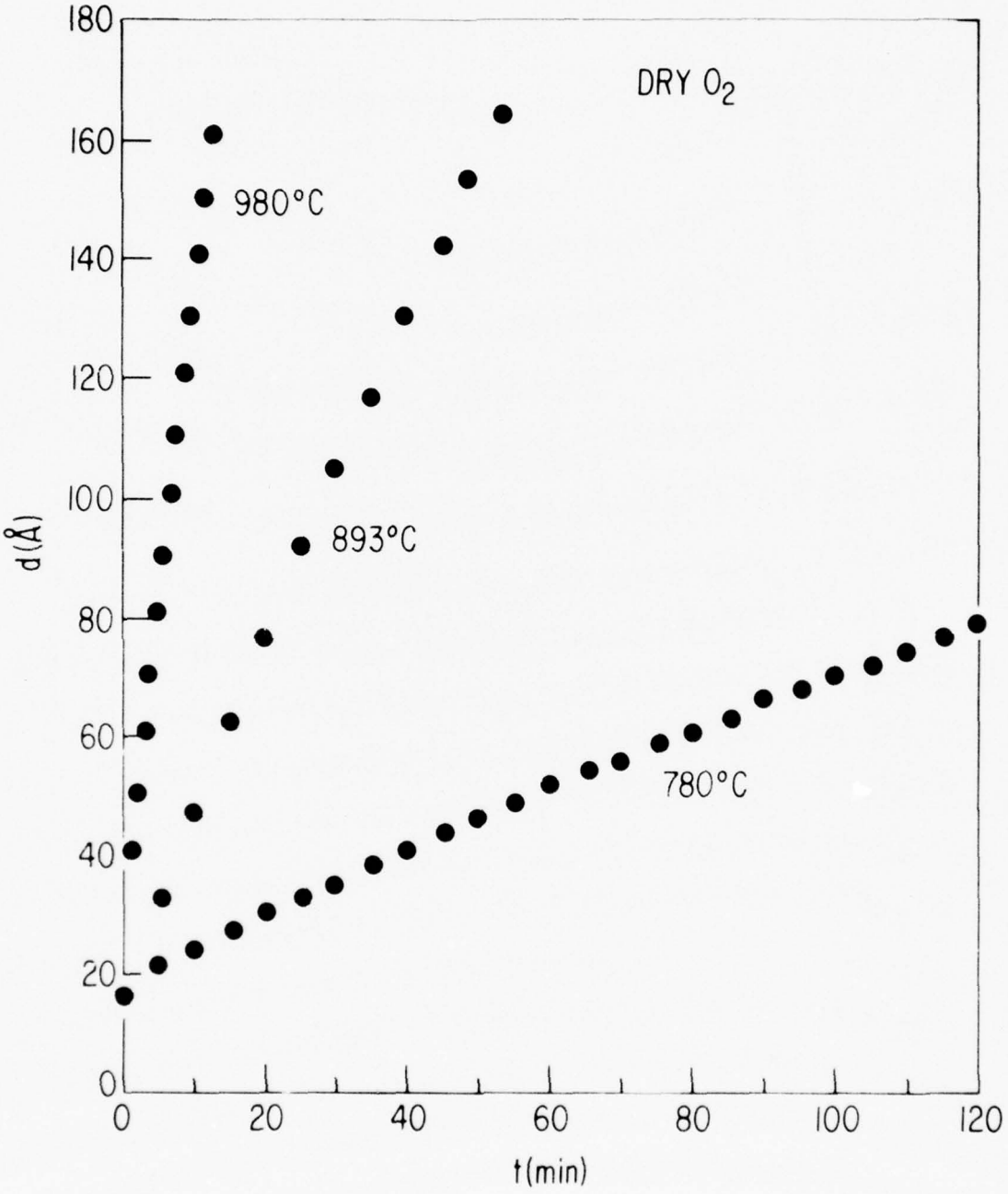
DRY O_2
980°C
893°C
780°C
d(Å)
t(min)
0
20
40
60
80
100
120
140
160
180

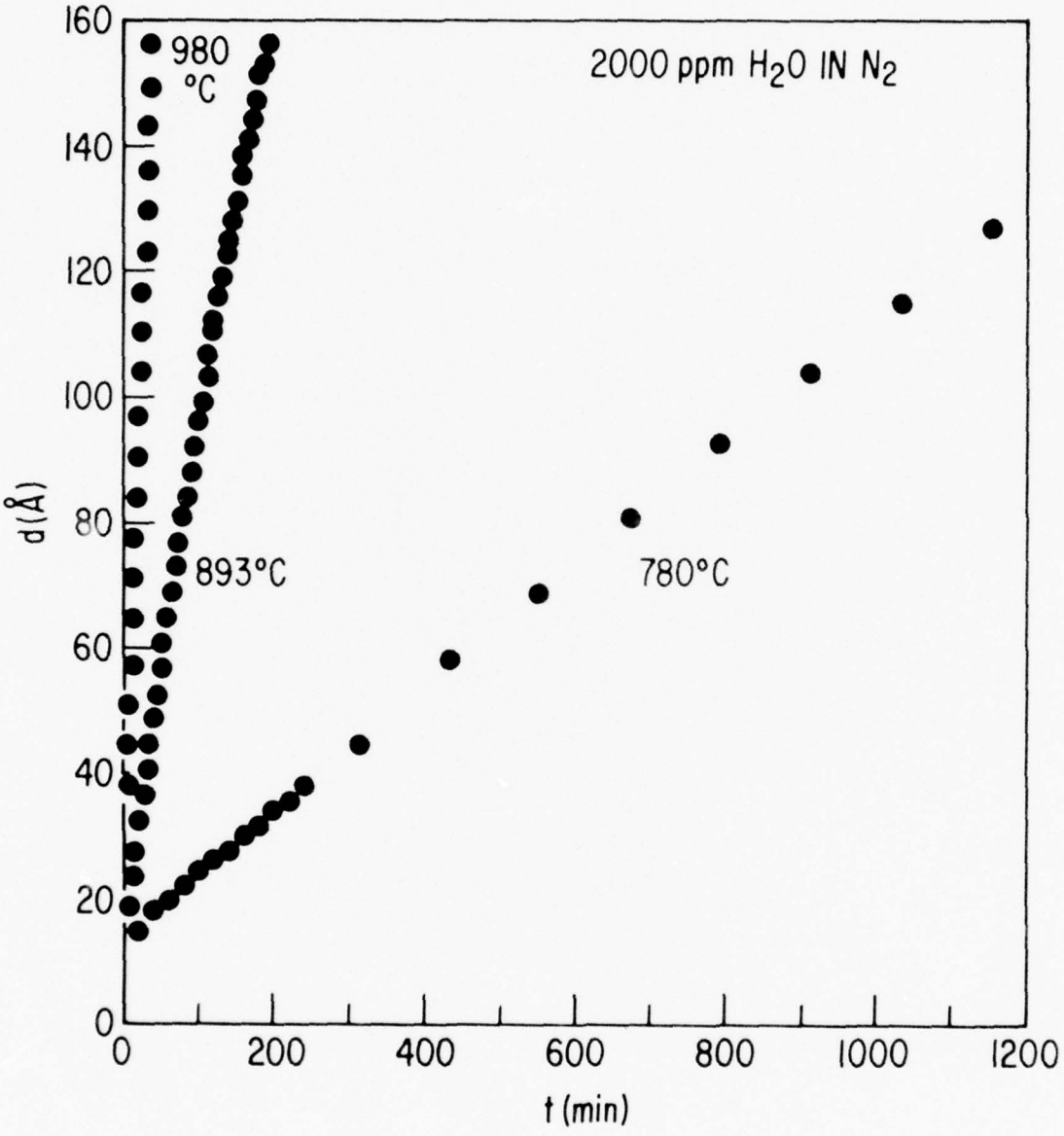
2000 ppm H_2O IN N_2
980 °C
893°C
780°C
d(Å)
t (min)
0
20
40
60
80
100
120
140
160
0
200
400
600
800
1000
1200

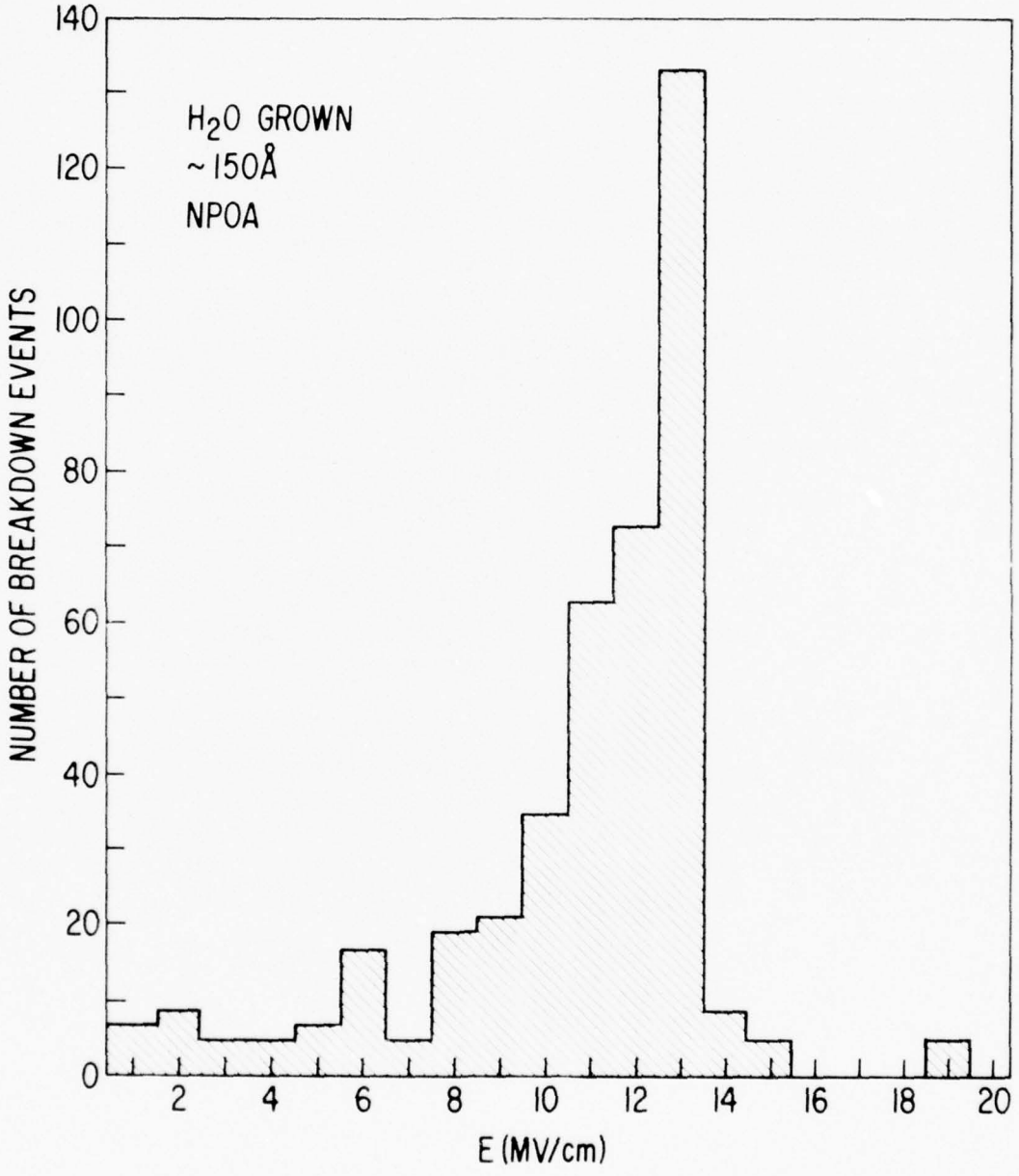
140
120
100
80
60
40
20
0
NUMBER OF BREAKDOWN EVENTS
H2O GROWN
~150Å
NPOA
2
4
6
8
10
12
14
16
18
20
E (MV/cm)

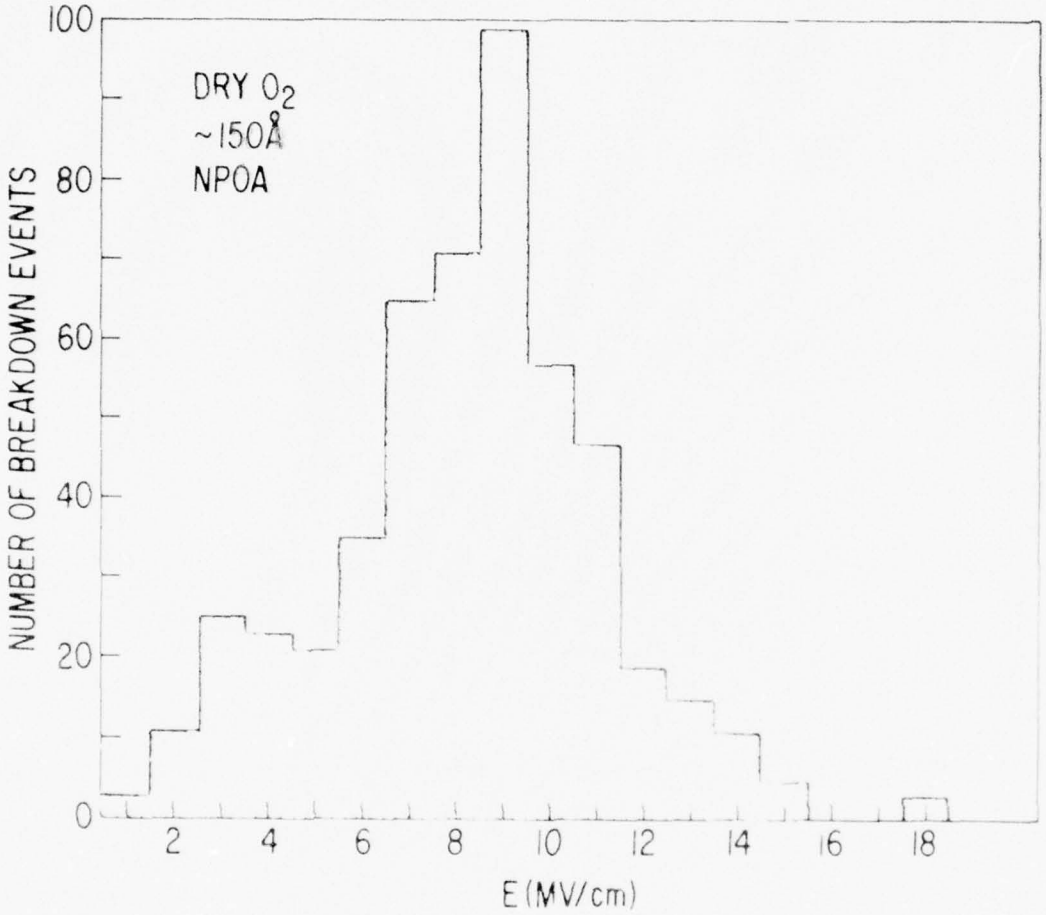
DRY O_2
~150Å
NPOA
NUMBER OF BREAKDOWN EVENTS
100
80
60
40
20
0
2
4
6
8
10
12
14
16
18
E(MV/cm)

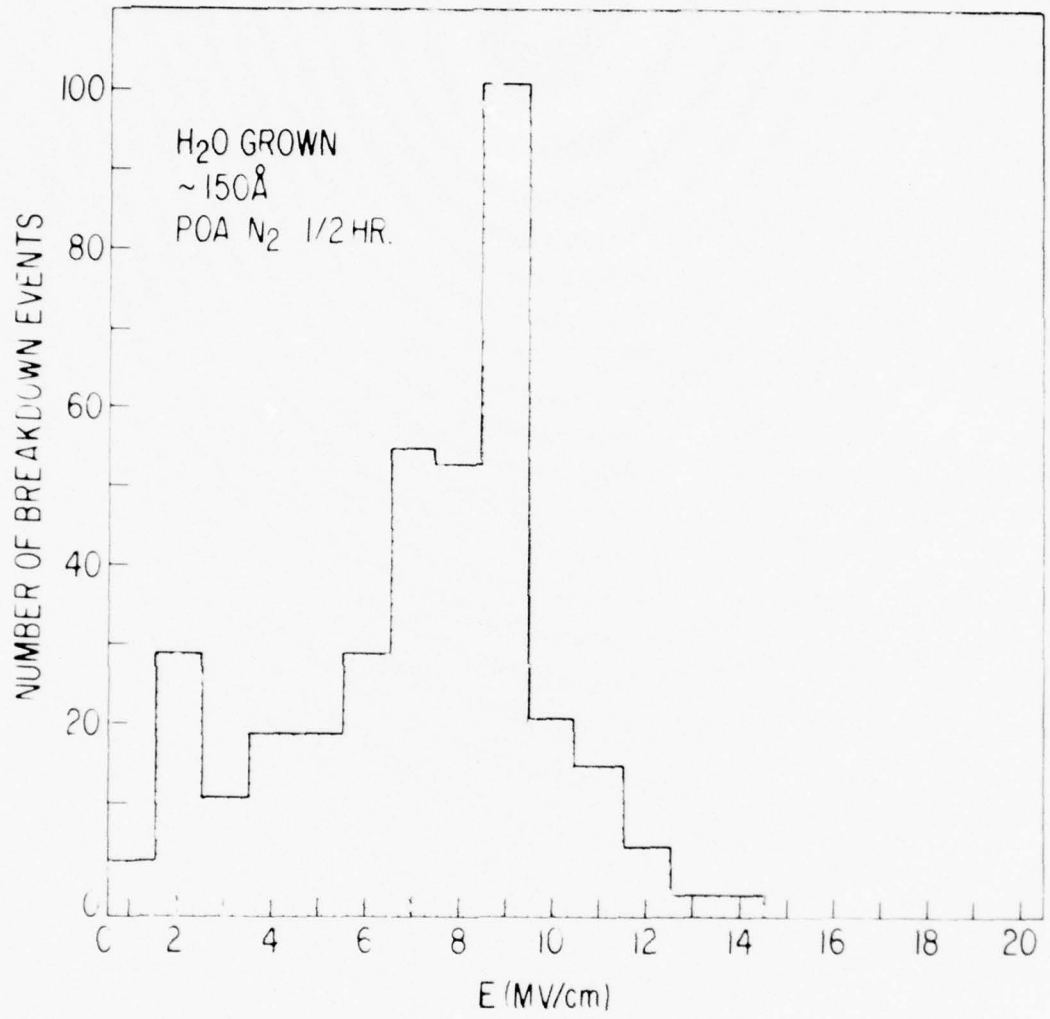
H_2O GROWN
~150Å
POA N_2 1/2 HR.
NUMBER OF BREAKDOWN EVENTS
100
80
60
40
20
0
0
2
4
6
8
10
12
14
16
18
20
E (MV/cm)

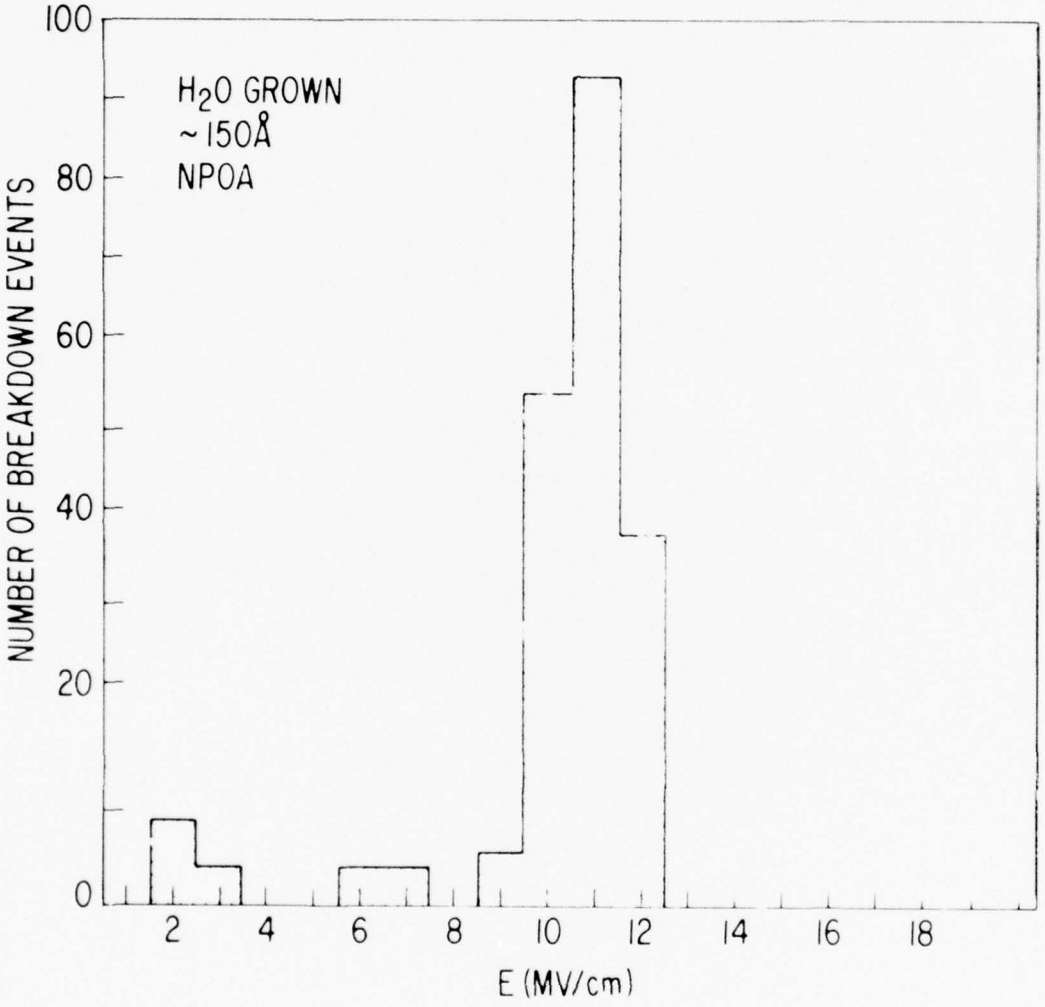
100
80
60
40
20
0
H_2O GROWN
~150Å
NPOA
NUMBER OF BREAKDOWN EVENTS
2
4
6
8
10
12
14
16
18
E (MV/cm)

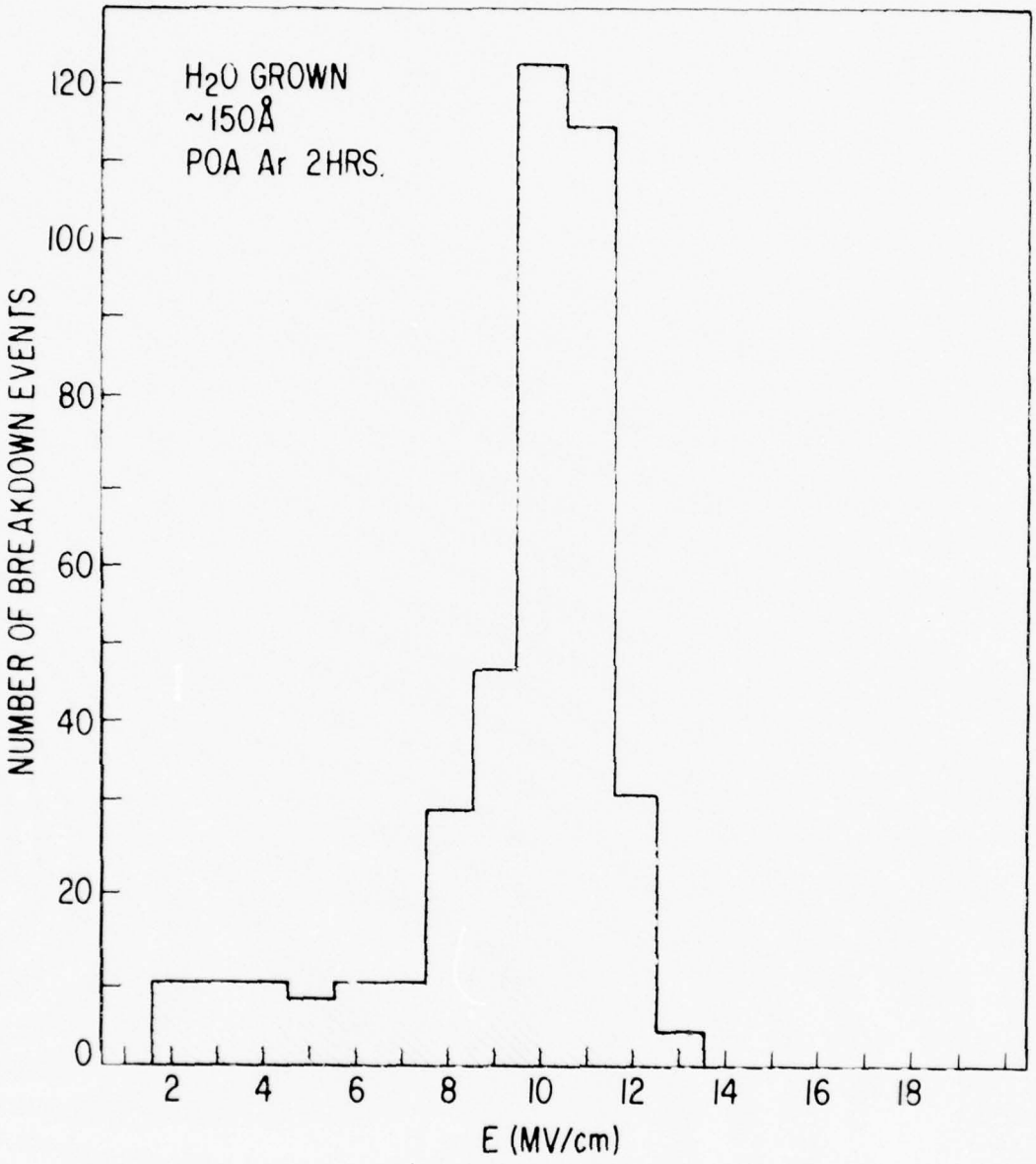
H_2O GROWN
~150Å
POA Ar 2HRS.
NUMBER OF BREAKDOWN EVENTS
0
20
40
60
80
100
120
2
4
6
8
10
12
14
16
18
E (MV/cm)

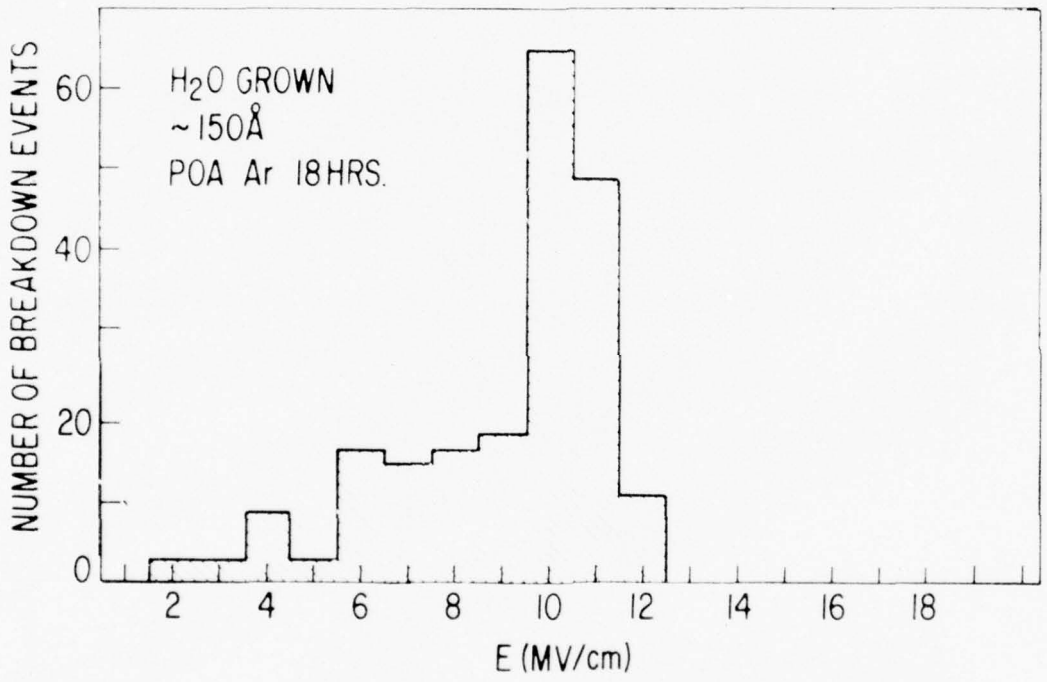
NUMBER OF BREAKDOWN EVENTS
60
40
20
0
H_2O GROWN
~150Å
POA Ar 18HRS.
2
4
6
8
10
12
14
16
18
E (MV/cm)

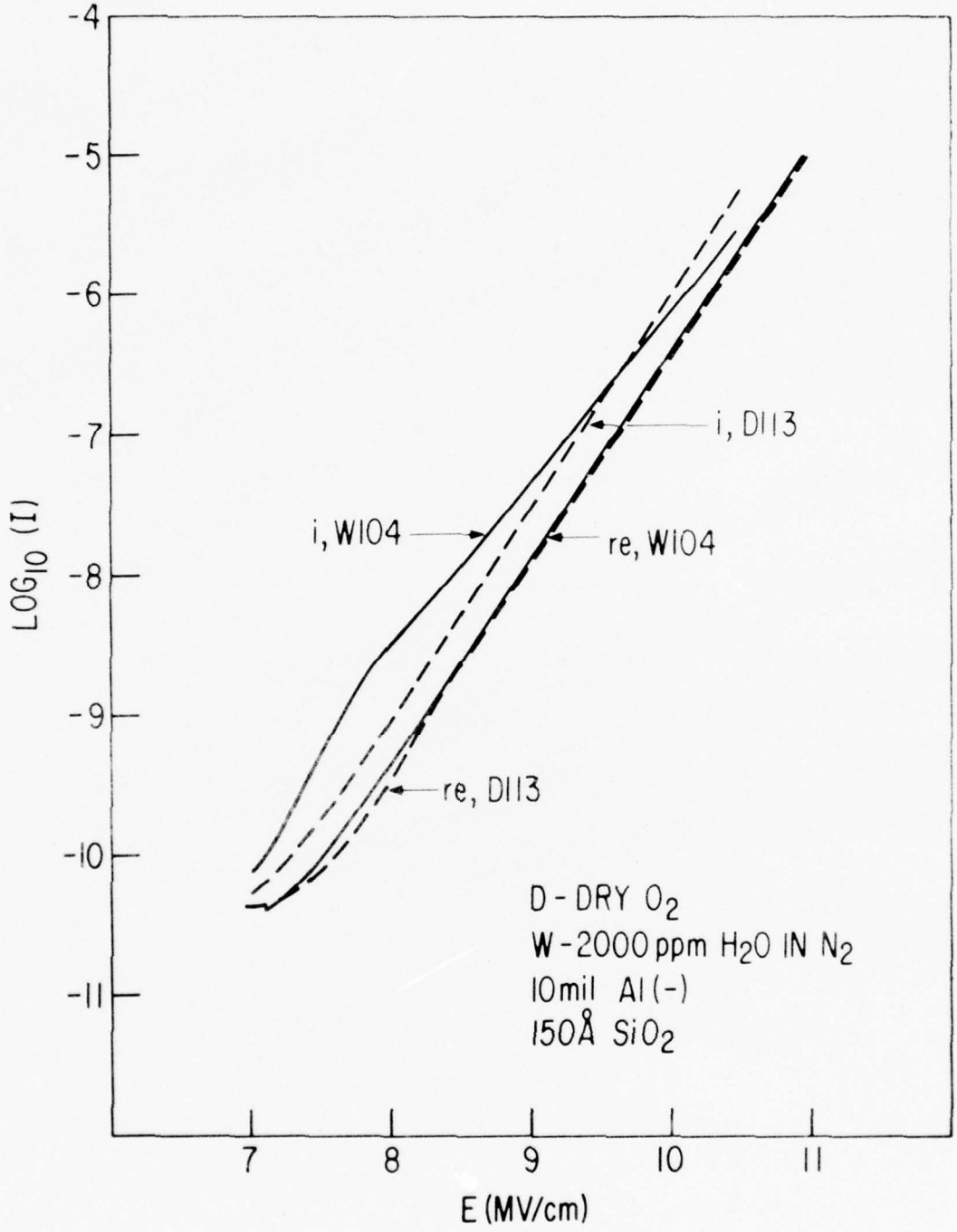
-4
-5
-6
-7
-8
-9
-10
-11
LOG10 (I)
i, W104
i, D113
re, W104
re, D113
D - DRY O2
W - 2000 ppm H2O IN N2
10mil Al(-)
150Å SiO2
7
8
9
10
11
E (MV/cm)

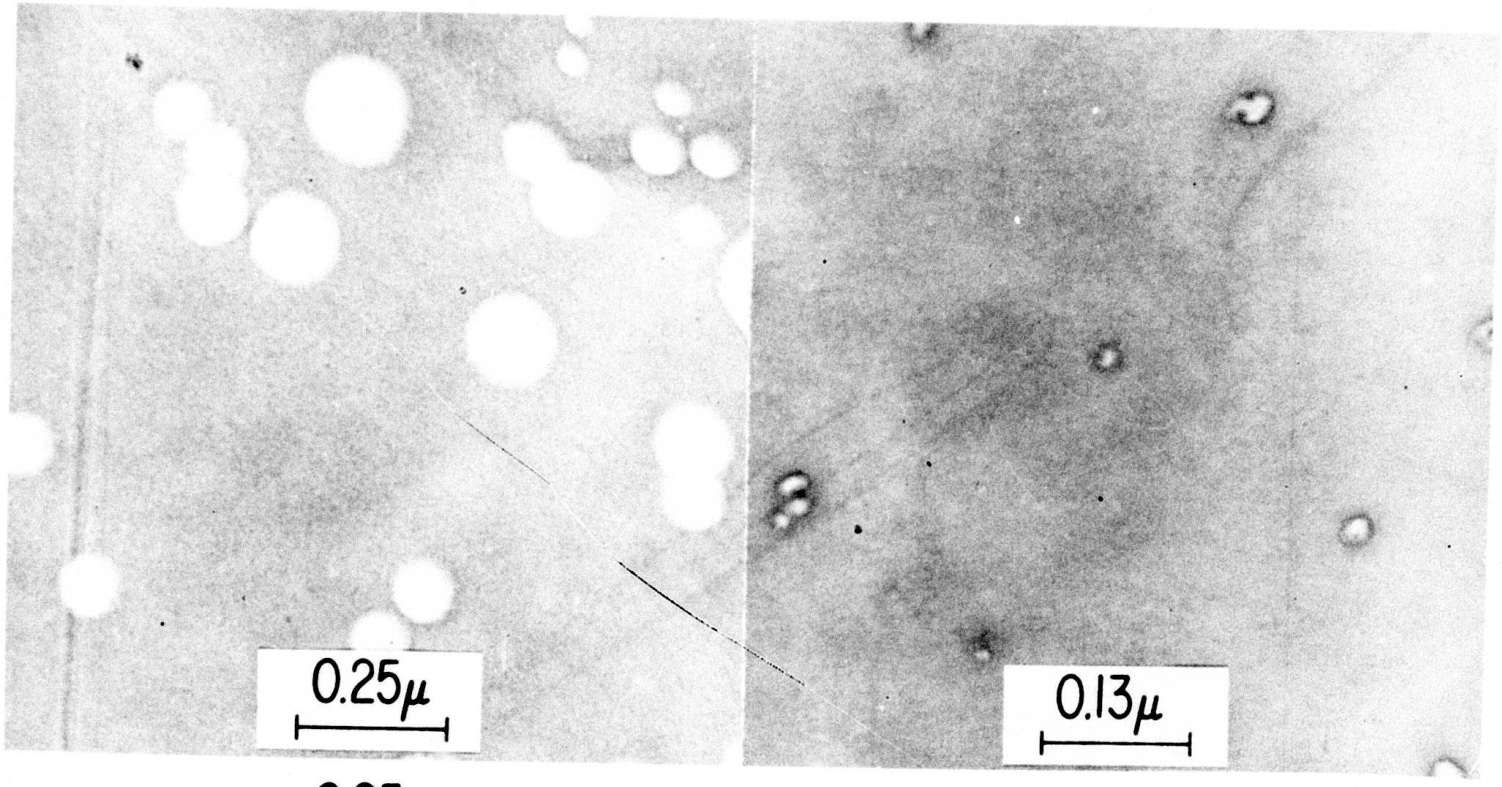

(a) (b)

(a)
0.25μ
(b)
0.13μ
(c)
0.13μ

LIST OF FIGURES

LIST OF TABLES

Results of Fitting the Data from Fig. 1 to the linear equation

$$t = k_1 d + k_2$$

where t and d are the time of oxidation and SiO_2 film thickness respectively. D represents a dry O_2 oxidation ambient and W represents 2000 ppm H_2O in N_2.

The Electronic Structure of SiO_2, $Si_xGe_{1-x}O_2$, and GeO_2 from Photoemission Spectroscopy*

B. Fischer†, R. A. Pollak, T. H. DiStefano and W. D. Grobman
IBM Thomas J. Watson Research Center
Yorktown Heights, New York 10598

ABSTRACT

The valence band structure of the mixed silicate $Si_xGe_{1-x}O_2$ was investigated for a range of compositions by X-ray and UV photoemission spectroscopy. Structure in the valence band, which is derived from the oxygen non-bonding orbitals and from the Si-O bonding orbital, is seen to move continuously in initial energy in going from SiO_2 to GeO_2. The width of the non-bonding bands at the top of the valence band decreases from about 3.3 eV in SiO_2 to 2.0 eV in GeO_2 in which separate peaks are no longer resolved. The decrease in width of the non-bonding bands is correlated with an increase in the average oxygen-oxygen separation from 2.62 Å to 2.85 Å. The results indicate that the width of the non-bonding bands is largely due to oxygen wavefunction overlap. The valence bands measured by photoemission from the mixed oxide are not a superposition of SiO_2 and GeO_2 valence bands. On the other hand bandgap excitations, as determined by energy loss satellites on the photoemission spectra, were found to be a superposition of those for SiO_2 and GeO_2, indicating local conduction band states centered about the Ge and Si sites.

* Supported in part by the Defense Advanced Research Projects Agency and monitored by AFCRL under contract No. F19628-76-C-0249.

I. INTRODUCTION

The general class of silicate materials, which has been studied extensively both in nature and in several materials of technological interest, is only recently being investigated from the point of view of electronic structure. The best understood member of the class is SiO_2, for which theoretical calculations[1-4] of the electronic structure are based on X-ray and UV photoemission[5,6] spectra, in combination with optical properties and X-ray emission spectra, and electron energy loss spectra. The picture which emerges for the electronic structure of SiO_2 is a collection of narrow, oxygen-like bands at the top of the valence band, with a broad Si-O bonding band lying more than 5 eV below the valence band edge. The character of the valence band edge of SiO_2 is dominated by the oxygen orbitals, and is only weakly sensitive to crystal structure as is seen in the similarity of the optical properties of amorphous and crystalline quartz[7]. Both the crystal structure[8] and electronic structure[9] of GeO_2 are similar to that of SiO_2. Nevertheless, the physical properties of these two materials are somewhat different; e.g. the amorphous and hexagonal forms of GeO_2 are water-soluble while all forms of SiO_2 are insoluble. The bandgap of amorphous SiO_2 is 9.0 eV[10] compared to about 5.6 eV for GeO_2[11]. Photoemission and differential photoyield spectra of SiO_2 and GeO_2, published recently by Rowe[6], are similar for both oxides, although there are some differences in the energy levels of the valence bands. Since both SiO_2 and GeO_2 have the same structure based on tetrahedra of oxygen atoms around Si or Ge centers (see Fig. 1), one can produce a mixed system $Si_xGe_{1-x}O_2$ in which each of the tetrahedra may be centered about either Si or Ge. By studying variations in the photoemission spectra of the mixed systems of different compositions, it is possible to examine details of the oxygen derived bands.

In this paper we study systematically the trends in the features of the photoemission spectra for the mixed system $Si_xGe_{1-x}O_2$ with $0 \leq x \leq 1$. The parameter which changes most dramatically in this series is the O-O distance. This occurs because GeO_4 tetrahedra with a central Ge atom have an O-O separation which is about 9% greater than that in SiO_4 tetrahe-

dra. More specifically, for some intermediate mixtures, there are three nearest neighbor possibilities for an oxygen ion: it can be shared by (1) two SiO_4 tetrahedra, (2) one SiO_4 and one GeO_4 tetrahedron, or (3) two GeO_4 tetrahedra. The average O-O separation is increased as the GeO_2 concentration is increased. Other parameters such as the small variation in the Si(Ge)-O-Si(Ge) bond angle or in the ionicity are not thought to influence appreciably the valence band structure of the $Si_xGe_{1-x}O_2$. Thus, by studying the electronic structure of $Si_xGe_{1-x}O_2$ we are able to determine the influence of the O-O wavefunction overlap interaction on the electronic structure of silicates. The nonbonding O 2p orbitals comprise the top of the valence band, and therefore these studies aid our understanding of fundamental electronic properties[12] such as hole-conduction, radiation damage, and dielectric breakdown in silicate glasses.

II. EXPERIMENTAL

Si_xGe_{1-x} films several thousand Angstroms thick were prepared by DC sputtering onto sapphire substrates. The sputtering target was prepared by melting a mixture of high purity polycrystalline silicon and germanium onto a molybdenum substrate in an argon arc furnace. The films studied with UPS were oxidized in the spectrometer by heating at 450°C in 10^{-5} torr of oxygen for 15 min. The films studied with XPS were oxidized by heating at 650°C in a tube furnace for 3 hours while flowing oxygen over the sample and then immediately transferring the sample to the spectrometer vacuum. The compositions of the films used in the UPS experiments were determined by electron microprobe analysis and the compositions of the films used in the XPS experiments were estimated from the relative intensities of the Ge 3d, Si 2p, and O 1s core-levels.

The UPS measurements were performed using a cylindrical mirror electrostatic-deflection type electron energy analyzer (resolution 0.25 eV) and 21.2 or 40.8 eV photons from a He-discharge lamp. The residual chamber pressure during measurement was between 5×10^{-10} torr and 2×10^{-8} torr. The XPS measurements were performed with a Hewlett-Packard ESCA

spectrometer which has a monochromated $AlK\alpha_{1,2}$ X-ray source (1486.6 eV) and a resolution of 0.5 eV. The pressure in the measurement chamber was 10^{-9} torr.

During the photoemission measurements, the surfaces of the oxidized Si_xGe_{1-x} films were in contact with the grounded sample holder. Only the $Si_{.9}Ge_{.1}O_2$ sample exhibited substantial charging during the XPS experiment. Charging was neutralized by flooding the sample with 10 mA of electrons of 10 eV kinetic energy. The spectrum of crystalline α-quartz (Fig. 8) which we discuss later required a neutralizing current of 10 mA at 2 eV. All binding energies are reported with respect to the top of the valence band which was determined by extrapolation of the leading edge of the valence bands to the background level.

III. RESULTS

A. X-Ray Photoemission Spectroscopy

Six amorphous $Si_xGe_{1-x}O_2$ films with compositions x = 0.0, 0.03, 0.37, 0.78, 0.90, and 1.0 were studied by X-ray photoemission spectroscopy. Typically, a 1000 eV wide overall scan, the Ge 3s, Ge 3p, Ge 3d, Si 2s, Si 2p, O 1s core-levels, and the valence bands were sequentially scanned and computer time averaged for a total of 15 to 20 hours. Fig. 2a. is a 1000 eV overview spectrum of the $Si_{.37}Ge_{.63}O_2$ sample. The first 200 eV of this spectrum is plotted on an expanded scale in Fig. 2b. The small C 1s peak near 280 eV is from carbon contamination by adsorption of residual gases during the course of the experiment. The large variation of photoelectric cross-section among different energy levels is exemplified by the difference in intensity between the O 1s level with 4 electrons and the Ge 3d level with $10 \times 0.63 = 6.3$ electrons per average molecular unit (see Fig. 2a.). The low photoelectric cross-section of the valence orbitals (0 to 12 eV) necessitates a relatively long counting time in order to reduce the effect of noise in the data. Germanium (LMM) and oxygen (KLL) Auger peaks are also present in Fig. 2.

The X-ray photoemission spectra of orbitals within 40 eV of the top of the valence band are shown in Figs. 3a, 3b, and 3c for GeO_2, $Si_{.37}Ge_{.63}O_2$ and SiO_2 respectively. The main features are the Ge 3d level at 29 eV and valence orbitals between 0 and 25 eV. The peak at 20 eV is derived mainly from the O 2s orbital, and the structure between 0 and 12 eV is derived from the O 2p, Ge 4s, Ge 4p, Si 3s, and Si 3p orbitals. Spectra of the outermost orbitals of the $Si_xGe_{1-x}O_2$ films which were studied are compared in Fig. 4.

Inelastic energy loss structure is observed on the low kinetic energy side of every photoemission peak. This is most clearly seen for the O 1s peak in Fig. 2a. A higher resolution scan of the O 1s energy loss region is shown in Fig. 5a. The regions of onset of the O 1s inelastic energy loss structure of the six films studied are compared in Fig. 5b, where the O 1s (not shown) peaks are aligned at 0 eV. Both interband transitions and plasmon excitations contribute to the loss structure on the high binding energy side of the core level peaks. The loss at 10 eV in SiO_2 (peak 1 in Fig. 5b) and 7.2 eV in GeO_2 (peak 2 in Fig. 5b) correspond to the first interband transition[6]. It is interesting to note that this transition energy does not smoothly vary across the solid solution series as one adds Ge, but instead the 7.2 eV excitation at position 2 appears at low concentrations of Ge and increases with the amount of Ge present. This indicates that the conduction band edge is dependent upon local position in the material. An optical excitation from an non-bonding oxygen derived orbital with a Ge nearest neighbor can occur at an energy about 2.8 eV less than an excitation of an orbital with Si nearest neighbors.

B. UV Photoemission Spectroscopy

Five amorphous $Si_xGe_{1-x}O_2$ films with compositions x = 0.0, 0.24, 0.46, 0.73, 1.0 were studied UV photoemission spectroscopy. Spectra ($h\nu$ = 40.8eV) of the valence band orbitals between 0 and 12 eV are shown in Fig. 6. The variations of the positions and widths of the three main peaks of the spectra are plotted in Fig. 7 for the mixed material. The major features of the valence bands are seen to change continuously in going across the series from

SiO_2 to GeO_2. This continuity allows us to identify corresponding features in SiO_2 and GeO_2 on a one-to-one basis.

UPS spectra obtained at $h\nu$ = 21.2eV show an enhancement of the inelastic electron emission at low kinetic energies, particularly for x near 0. Excited electrons with less crystal kinetic energy than the optical gap E_g have an extremely long inelastic scattering length since they are energetically forbidden to decay by electron-electron scattering processes.[13] Thus, the secondary yield observed at low kinetic energies increases with a decreasing E_g in going through the series toward x=0. The UPS spectra measured at $h\nu$ = 21.2 eV are not distorted by the threshold for electron-electron scattering since all of the electrons excited from the valence band lie at energies greater than E_g above the conduction band minimum.

IV. DISCUSSION

We will first describe the nature of the main features of the photoemission density of states for SiO_2 by comparing the X-ray emission spectra and photoemission spectrum of crystalline α-quartz. We will then describe how the change in the photoemission density of states of $Si_xGe_{1-x}O_2$ adds to the overall understanding of the electronic structure of silicates.

Klein and Chun's O Kα [14], Wiech's Si $L_{2,3}$ [15] and Lauger's Si Kβ [16] X-ray emission spectra of SiO_2 are drawn on the same energy scale with the X-ray photoemission spectrum of α-quartz[17] in Fig. 8. The relationship between the X-ray emission and X-ray photoemission spectra is illustrated in the energy level diagram shown in Fig. 9. Since the final state of the X-ray photoemission process is essentially the initial state of the X-ray emission process, it was possible to accurately align all spectra with respect to the top of the valence band by subtracting the XPS O 1s and Si 2p binding energies of quartz from the O Kα and Si $L_{2,3}$ X-ray emission spectra respectively. The Si 1s binding energy of quartz was determined by adding the quartz Si $K\alpha_{1,2}$ X-ray energy (1740.3)[14] to the quartz Si 2p XPS binding energy and this

value was subtracted from the Si Kβ X-ray emission spectrum in order to align it in fig. 8. This empirical method of aligning the X-ray and photoemission spectra eliminates the errors of interpretation previously introduced into the literature by arbitrarily aligning the O Kα and the Si $L_{2,3}$ spectra.

It is immediately obvious that there is a close correspondence between structure in the photoemission and X-ray emission spectra in fig. 8. Photoemission from all orbitals across the valence bands is allowed, although it is modulated in intensity by the photoelectric cross section. The X-ray emission process is governed by two factors: 1) the dipole selection rule which only allows X-ray transitions from valence orbitals with angular momentum quantum numbers which are ±1 different from that of the initial hole state and 2) wavefunction overlap between the initial and final state one-electron orbitals. The dipole selection rule effectively allows only X-ray transitions from orbitals with p-like symmetry about the appropriate atomic center in the O Kα and Si Kβ spectra and with s- or d-like symmetry in the Si $L_{2,3}$ spectrum. The overlap requirement makes the X-ray emission process a local probe which samples only valence orbitals with amplitude near the core of the atom with the initial state hole; that is, near the oxygen nucleus for the O Kα and near the silicon nucleus for the Si Kβ and Si $L_{2,3}$ X-ray spectra.

To understand the electronic structure of silica it is useful to use the molecular orbitals of the cluster SiO_4^{4-} for which the point group is T_d and the molecular orbitals are described in terms of the tetrahedral irreducible representations.[2,4] The energy eigenvalues of the molecular orbitals of the SiO_4^{4-} cluster have been calculated by various methods.[2] Tossell, Vaughan, and Johnson, using the results of their SCF Xα scattered wave calculation, have correlated the molecular orbitals of the SiO_4^{-4} cluster with the features in the X-ray emission spectra of quartz.[4] Yip and Fowler have made a similar comparison between photoemission and X-ray emission data, and the results of their LCAO-MO calculation.[2]

We now compare the X-ray photoemission spectrum of quartz with the empirically aligned

valence band X-ray emission spectra. From the nature of the molecular orbitals of the SiO_4^{-4} cluster, we can deduce the character of the bands which occur near the corresponding energy in the photoemission spectrum. Our band picture to a large extent follows the assignments made by Tossel, Vaughan, and Johnson[4], with some exceptions. The $4a_1$ and $3t_2$ molecular orbitals associated with binding energies 1 and 2 in Fig. 8 are mainly derived from O 2s with a small amount of Si 3s and Si 3p respectively. The $4a_1$ level is observed selectively as peak 1 in the Si $L_{2,3}$ emission spectrum, while the $3t_2$ level is seen as peak 2 in the Si Kβ emission spectrum. The $4a_1$ and $3t_2$ bands are not resolved separately in the photoemission spectrum. The $5a_1$ and $4t_2$ orbitals associated with peaks 3 and 4 are σ-bonding orbitals between the O 2p and the Si 3s and Si 3p orbitals respectively. Peak 3 in the Si $L_{2,3}$ X-ray emission spectrum and the XPS spectrum appears to be due to bands largely derived from the $5a_1$ molecular orbital, while peak 4 in the Si Kβ emission spectrum, in the O K spectrum and in the XPS spectrum is due to bands derived from the $4t_2$ molecular orbitals. It is interesting to note that structure in peak 3 is lost on going from crystalline α-quartz shown in Fig. 8 to amorphous SiO_2 in Fig. 4f. A similar effect is observed on going from crystalline to amorphous silicon.[20] The 1e, $5t_2$ and the $1t_1$ molecular orbitals loosely associated with peaks 5 and 6 essentially comprise nonbonding O 2p orbitals with little Si orbital mixture. Bands derived from these molecular orbitals comprise the group of nonbonding bands at the top of the valence band. Following Tossell, Vaughan, and Johnson we identify peak 5 with transitions from the 1e and $5t_2$ levels; the prominent peak 5 in the Si $L_{2,3}$ spectrum is ascribed to a crossover transition[21] from a wavefunction largely centered on the O to the Si 2p core hole. Of these three nonbonding orbitals, $1t_1$ has the smallest component of Si orbitals and lies at the top of the valence band at peak 6.

The width of the set of nonbonding bands derived from the 1e, $5t_2$, , $1t_1$ orbitals results from several factors, including the splitting of the oxygen orbitals due to the deviation of the Si(Ge)-O-Si(Ge) bond angle from colinearity, and that due to an overlap of the O 2p wave functions centered on adjacent oxygen sites (see Fig. 1). The relative importance of the bond

angle and of the oxygen orbital overlap in determining the width of the set of nonbonding bands is open to question. In the alloy series $Si_xGe_{1-x}O_2$ from SiO_2 to GeO_2, both the oxygen bonding angle and the average O-O nearest neighbor separation are changed significantly. The average O-O separation increases from 2.62Å in SiO_2[22] to about 2.85Å in GeO_2[8]. The variation in the Si(Ge)-O-Si(Ge) angle, on the other hand, is less well known. The bond angle in a-SiO_2 is ~150°, on the average, while that in a-GeO_2 is thought to be near the 130° angle found in hexagonal GeO_2. However, the variation in bond angle is thought, for several reasons, to have a relatively minor effect on the set of nonbonding bands. First, it has been found for various polymorphs of SiO_2, that a variation of the Si-O-Si bond angle of ~14° induces no singificant change in the width of the nonbonding bands[17]. Secondly, cluster calculations[2] on Si_2O by Yip and Fowler predict an increase of only 0.1 eV in the width of the nonbonding orbitals in going from a bond angle of 180° to 144°. And third, if the angle dependence of the width of the nonbonding oxygen band were dominant, then the top valence band in GeO_2 would be broader than that in SiO_2 which was not found to be the case experimentally. Overall the dominant parameter in the $Si_xGe_{1-x}O_2$ series is the O-O nearest neighbor separation.

The full-widths-at-half-maximum (FWHM) of the nonbonding bands from the $Si_xGe_{1-x}O_2$ UV photoemission spectra in figure 6 are shown in Fig. 7. For both the UPS and XPS results the FWHM is observed to decrease by about 1.3 eV on going from SiO_2 to GeO_2. The bandwidth is uniformly about 0.4 eV narrower in the UV photoemission spectra than the X-ray photoemission spectra. This difference most likely results from different relative photoelectric cross-sections across the band ($1e$, $5t_2$ and $1t_1$) when using 40.8 eV or 1486.6 eV photons. We also observe that the bandwidth decreases to a nearly constant intermediate value between 75% and 25% silicon. Also in the UPS spectra, a shoulder develops on the low binding energy side of the nonbonding O 2p band at high concentrations of silicon.

We interpret the results on the width of the set of nonbonding oxygen bands in the following manner. Since the germanium atom is larger than the silicon atom, substituting Ge for Si in a SiO_4 tetrahedron effectively separates the oxygen atoms, increasing the O-O nearest neighbor separation. The orbital overlap interaction between neighboring nonbonding O 2p orbitals is then smaller for the larger GeO_4 tetrahedra in which the average nearest neighbor O-O distance is about 2.85Å [8,23] compared to about 2.62Å in SiO_2[22]. It is this separation of the oxygen atoms that is responsible for the narrowing of the O 2p nonbonding band. Intermediate values of bandwidth occur in the concentration region from x = 0.25 to x = 0.75 where the probability is large that an oxygen atom is shared between a silicon tetrahedron and germanium tetrahedron. Within this interpretation, the nonbonding band is more band-like in SiO_2 and more molecular in GeO_2.

The spectra of an intermediate $Si_xGe_{1-x}O_2$ composition cannot be simulated by superposition of the spectra of pure GeO_2 and SiO_2 with x and (1-x) respectively as weight factors. The spectra cannot, therefore, be viewed as resulting from separate local regions of SiO_2 and GeO_2. There is also the question of whether adding GeO_2 to SiO_2 affects the potentials at the O and Si sites appreciably. The separations among the O 2p, Si 2p, and Ge 3d X-ray photoemission core levels do not vary by more than 0.2 eV for the sample compositions studied, indicating that the local potentials do not vary appreciably with composition, and that the ionicities of the SiO_2 and GeO_2 components are comparable.

V. CONCLUSION

The shape of the valence band structure in the mixed system $Si_xGe_{1-x}O_2$ changes continuously across a series of compositions from SiO_2 to GeO_2. The non-bonding oxygen 2p derived bands at the top of the valence bands decreases from 3.3 eV to 2.0 eV in going from SiO_2 to GeO_2, apparently due to the increase in the average O-O bond length from 2.62Å to about 2.85Å.

The sensitivity of the width of the non-bonding band to O-O separation indicates that oxygen-oxygen wavefunction overlap is largely responsible for the bandwidth which, in turn, determines the effective mobility of holes near the valence band edge. The bonding band lies at a binding energy, well below the valence band edge, which decreases continuously in going toward GeO_2 as one might expect from the smaller chemical binding energy of GeO_2.

Electron energy loss satellites on the X-ray photoemission spectra indicate an excitation bandgap for $Si_xGe_{1-x}O_2$ which is local. It appears that the conduction levels around Si are about 2.8 eV higher in energy than those around Ge, independent of composition. From this picture of local conduction levels, one would expect that electron conduction occurs by site hopping in the mixed system.

References

† Present address: Max-Planck-Institut für Festkörperforschung, Stuttgart, Federal Republic of Germany.

1. L. M. Roth and A. J. Bennett, "Electronic Structure of SiO_2", (in Proc. 10th Int. Conf. on Semicond. Physics, Cambridge, Mass., 1970), p. 619.

   S. J. Louisnathan and G. V. Gibbs, Am. Mineral **57**, 1614 (1972).

   J. A. Tossell, J. Chem. Phys. Solids **34**, 307 (1973).

   T. L. Gilbert, et al., Phys. Rev. **B8**, 5977 (1973).

   A. R. Ruffa, Phys. Stat. Sol. **29**, 605 (1968).

   Socrates T. Pantelides and W. A. Harrison, Phys. Rev. **B13**, 2667 (1976).

   P. M. Schneider and W. B. Fowler, Phys. Rev. Lett. **36**, 425 (1976).

2. K. L. Yip and W. B. Fowler, Phys. Rev. **B10**, 1391 (1974); and Phys. Rev. **B10**, 1400 (1974), and references therein.

3. M. H. Reilly, J. Phys. Chem. Sol. **31**, 1041 (1970).

4. J. A. Tossell, D. J. Vaughan, and K. H. Johnson, Chem,. Phys. Letters **20**, 329 (1973); J. A. Tossell, J. Am. Chem. Soc. **97**, 4840 (1975).

5. T. H. DiStefano and D. E. Eastman, Phys. Rev. Letters **27**, 1560 (1971).

6. J. Rowe, Appl. Phys. Letters **25**, 576 (1974).

7. H. R. Philipp, Sol. State Comm. **4**, 73 (1966).

   Eugene Loh, Sol. State Comm **2**, 269 (1964).

   K. Platzöder, Phys. Stat. Sol. **29**, K63 (1968).

   H. R. Philipp, J. Phys. Chem. Sol. **32**, 1935 (1971).

   S. H. Wemple, Sol. State Comm. **12**, 701 (1973).

   Yu P. Zakis, A. N. Trukhin, and V. P. Khimon, Soviet Physics - Sol. State **15**, 149 (1973).

8. G. S. Smith and P. B. Isaacs, Acta Cryst. **17**, 842 (1964).

9. S. T. Pantelides and W. A. Harrison, Phys. Rev. **B13**, 2667 (1976).

10. T. H. DiStefano and D. E. Eastman, Sol. State Commun. **9**. 2259 (1971).

11. L. Pajasova, Czech. J. Phys. **B19**, 1265 (1969); H. F. Bohm J. Non-Crist. Sol. **7**, 192 (1972).

12. H. L. Hughs and R. R. Giroux, Electronics **37**, 58 (1964).

J. P. Mitchell, IEEE Trans. Electron. Dev. **ED-14**, 764 (1967).

E. Kooi, Philips Res. Rept. **20**, 595 (1965).

A. S. Grove and E. H. Snow, Proc. IEEE **54**, 894 (1966).

E. H. Snow, A. S. Grove, and D. J. Fitzgerald, Proc. IEEE **55**, 1168 (1967).

K. H. Zaininger and A. G. Holmes-Siedle, RCA Rev. **28**, 208 (1968).

T. H. DiStefano and M. Shatzkes, Appl. Phys. Lett. **25**, 685 (1974).

13. D. E. Eastman, Phys. Rev. **B8**, 6027 (1973).

14. G. Klein and H.U. Chun. Phys. Stat. Sol. (b) **49**, 167 (1972).

15. G. Wiech, "Soft X-Ray Emission Spectra and the Valence Band Structure of Beryllium, Aluminum, Silicon, and Some Silicon Compounds", (in **Soft X-Ray Band Spectra**, D. J. Fabian, ed., Academic Press, New York, 1968), p. 59.

16. K. Lauger, Dissertation Univ. Munchen, (1960); quoted in ref. 14.

17. P. K. Roy, R. A. Pollak, and T. H. DiStefano, Bull. Am. Phys. Soc. **20**, 475 (1975).

18. C. G. Dodd and G. L. Glen, J. Appl. Phys. **39**, 5377 (1968).

19. D. S. Urch, J. Chem. Soc. (A) **19**, 3026 (1969).

20. L. Ley, S. Kowalczyk, R. Pollak, and D. A. Shirley, Phys. Rev. Letters **29**, 1088 (1972).

21. D.W. Fischer, Adv. X-Ray Anal. **13**, 159 (1970).

22. R. L. Mozzi and B. E. Warren, J. Appl. Cryst. **2**, 164 (1969).

23. E. Lorch, J. Phys. C. **2**, 229 (1969).

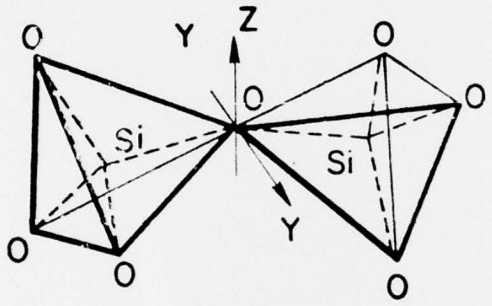

Figure 1 Two SiO_4 tetrahedra in SiO_2.

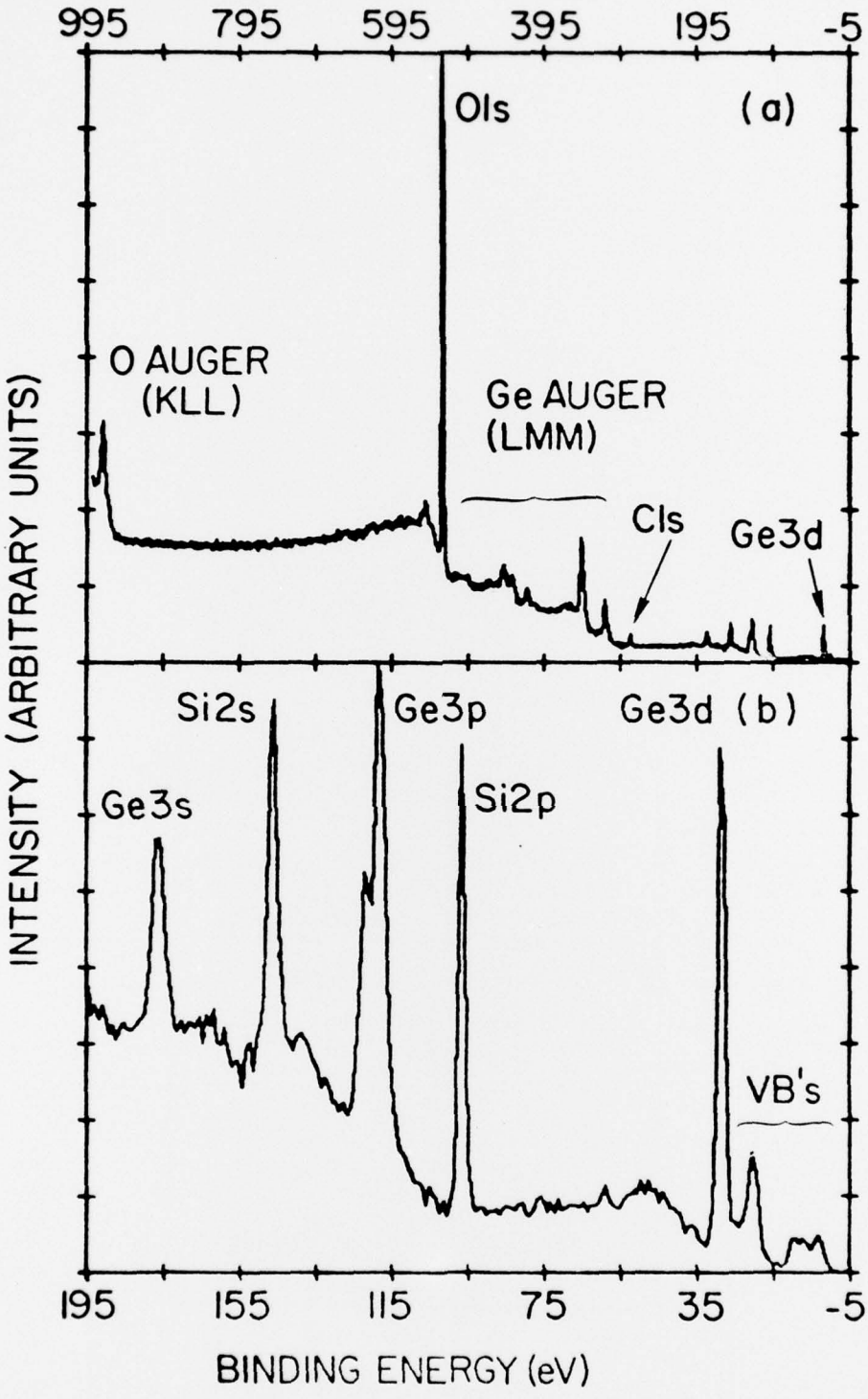

Figure 2 (a). Overview of the XPS-spectrum (AlKα) of amorphous $Si_{.37}O_{.63}O_2$.

(b). The first 200 eV of Figure 1a on an expanded scale.

Figure 3 XPS spectrum of the valence bands of amorphous :

(a). GeO_2,

(b). $Si_{.37}Ge_{.63}O_2$, and

(c). SiO_2.

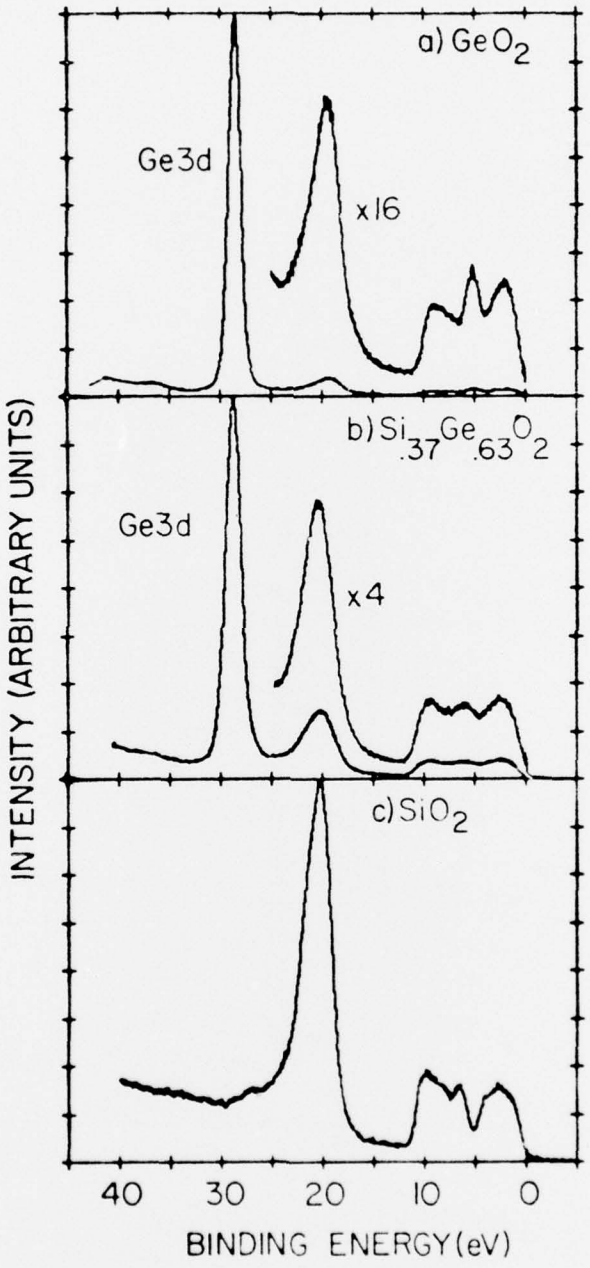

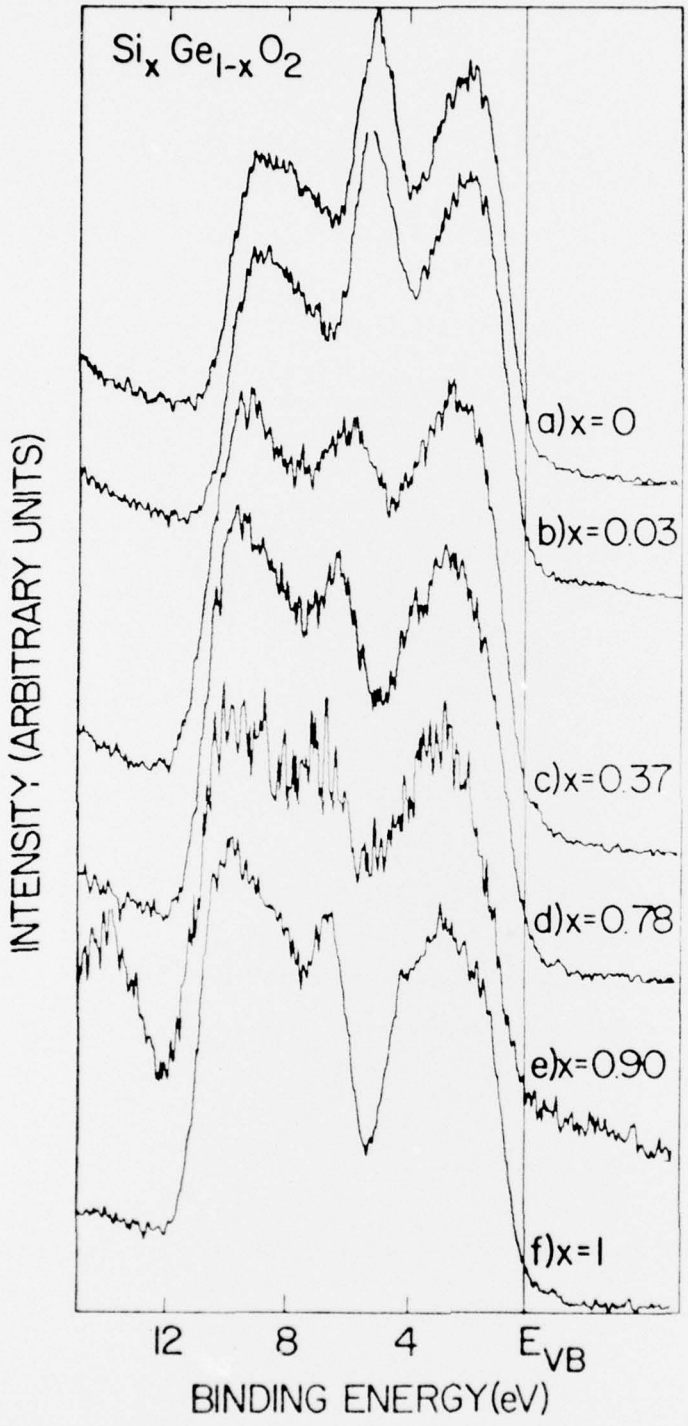

Figure 4 Comparison of the XPS valence band spectra of $Si_xGe_{1-x}O_2$ of six different compositions x: (a) 0, (b) 0.03, (c) 0.37, (d) 0.78, (e) 0.90 and (f) 1.0

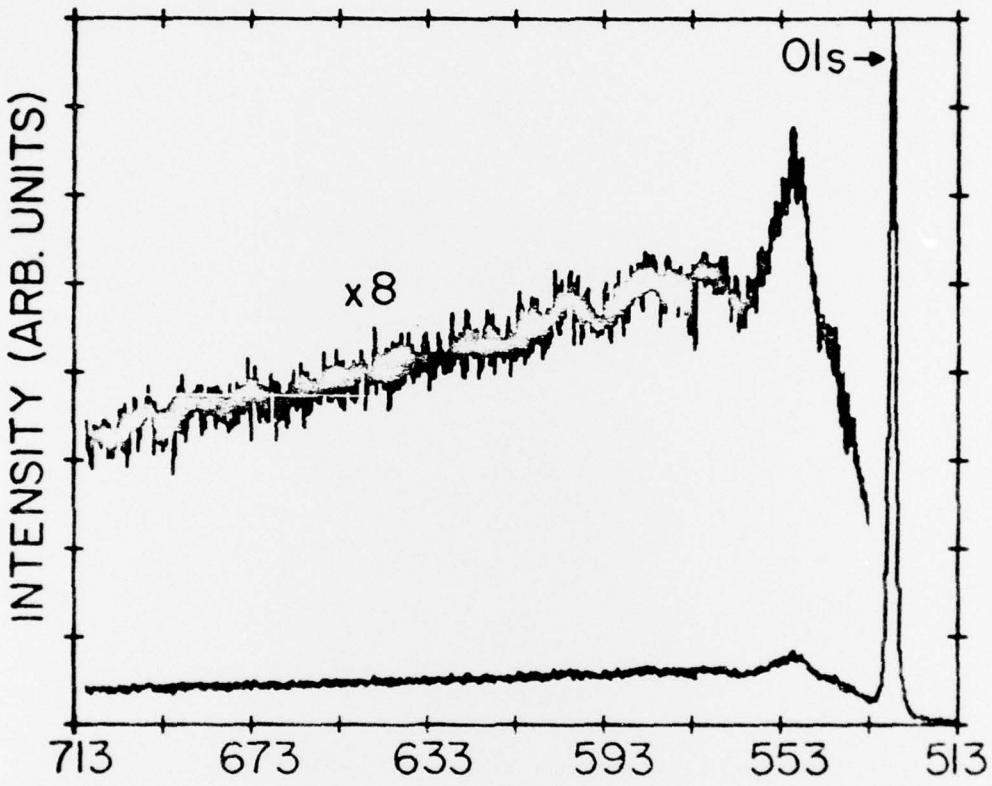

Figure 5a Inelastic energy loss structure on the low kinetic energy side of the O 1s peak for $Si_{.37}O_{.63}O_2$.

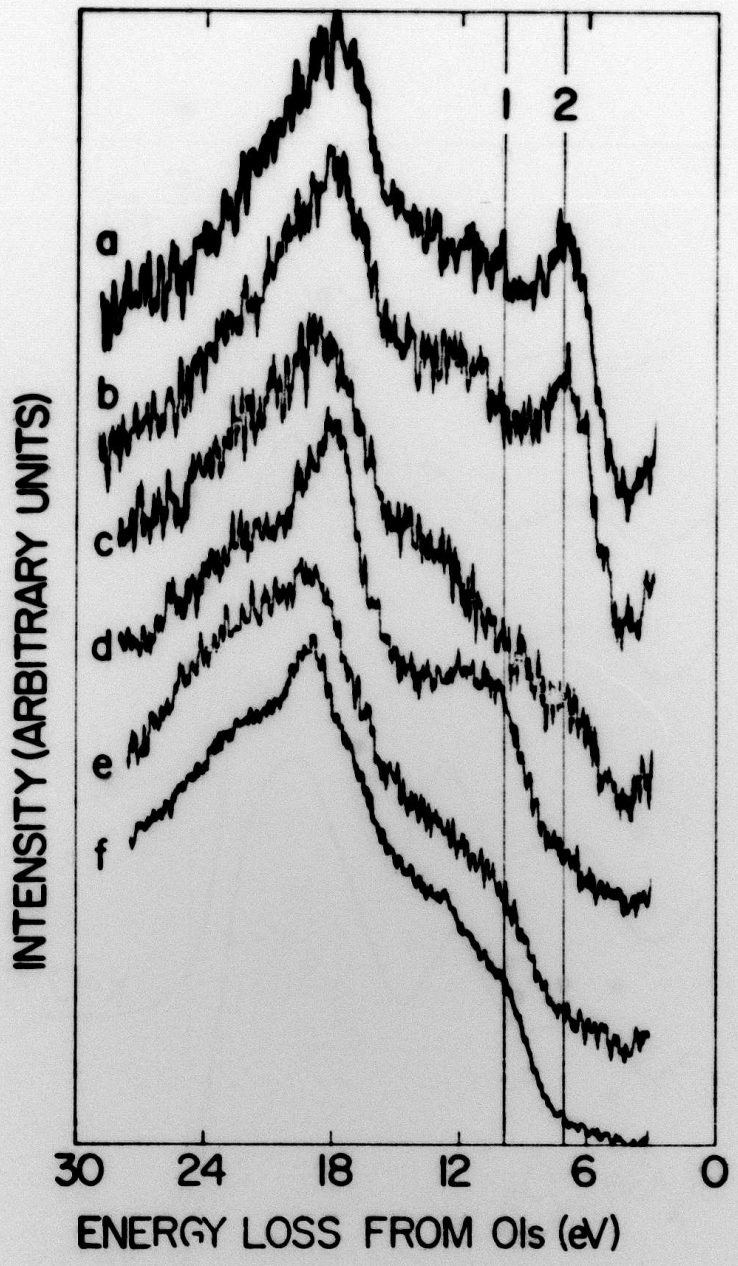

Figure 5b

Comparison of the inelastic energy loss structures from the O 1s core-level for the corresponding compositions x of $Si_xGe_{1-x}O_2$ shown in Figure 4 (where x is: (a) 0, (b) 0.03, (c) 0.37, (d) 0.78 (e) 0.90, and (f) 1.0). The zero of the energy scale denotes the position of the O 1s peak. The vertical lines 1 and 2 indicate the positions of the first loss structure of SiO_2 and GeO_2, respectively.

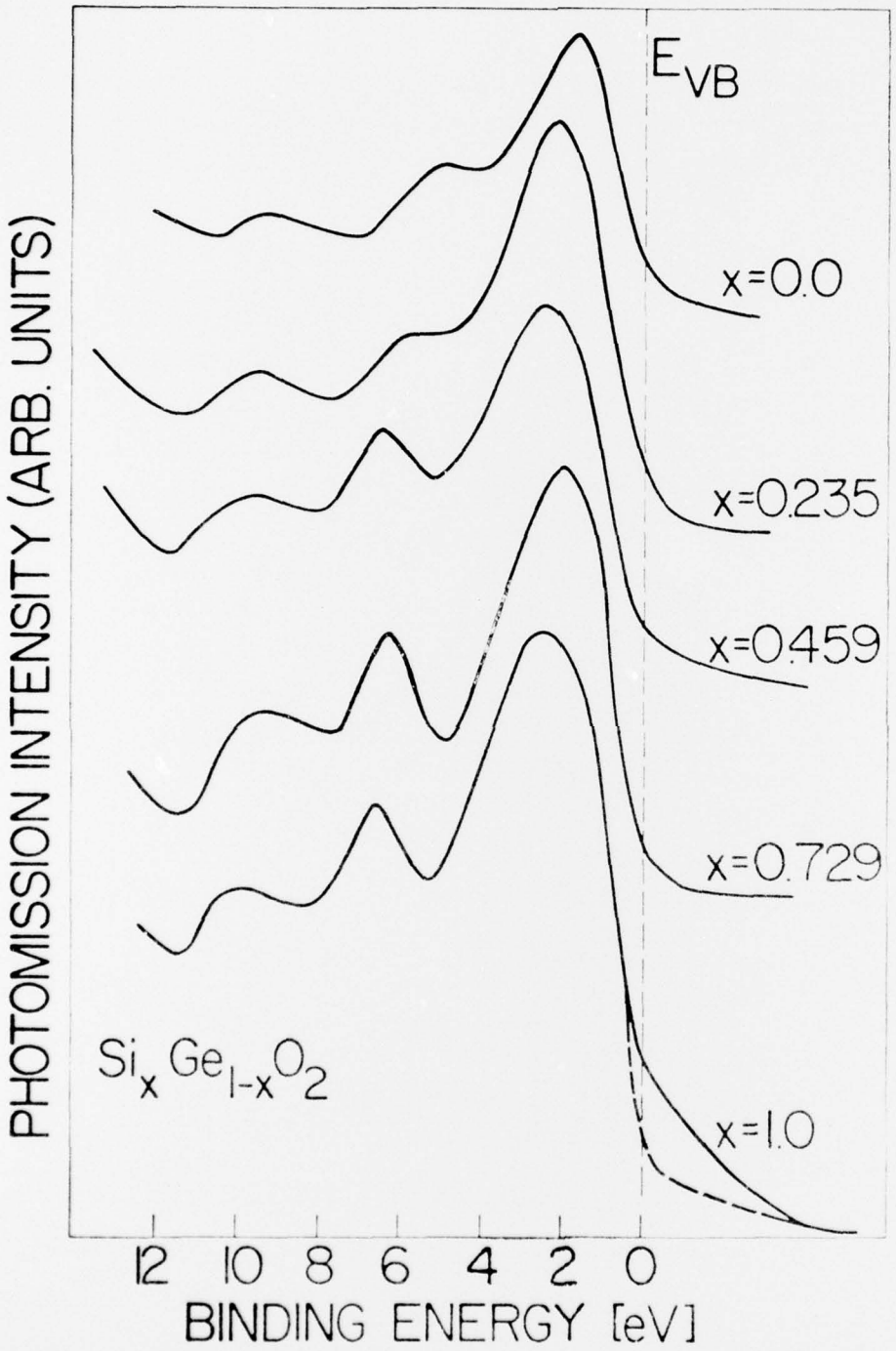

Figure 6 UPS spectra for five films of $Si_xGe_{1-x}O_2$ with different compositions x: (a) 0, (b) 0.235, (c) 0.459, (d) 0.729, and (e) 1.0. The energy of the incident photons is 40.8 eV.

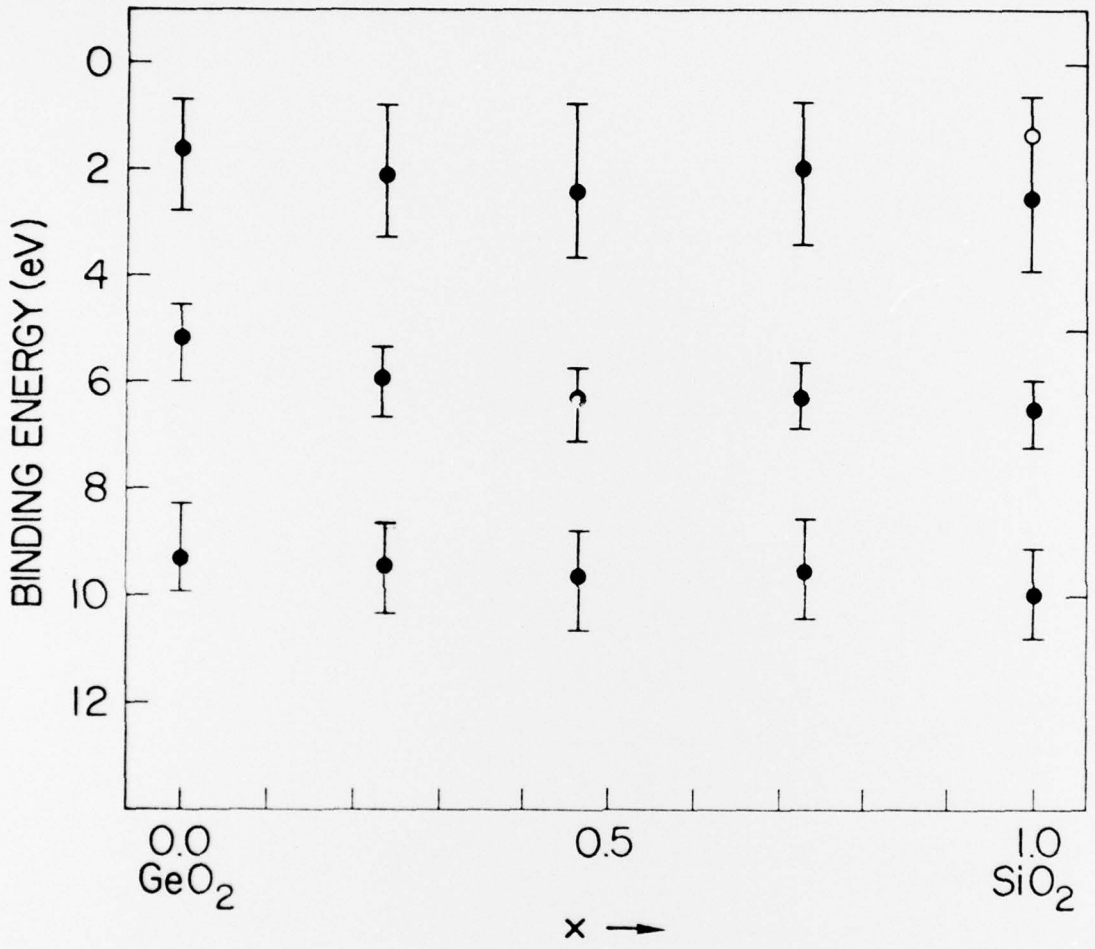

Figure 7 Variation of the position and width of the three main peaks of the spectra in Figure 6. The top peak for SiO_2 develops a small shoulder as indicated by the open circle.

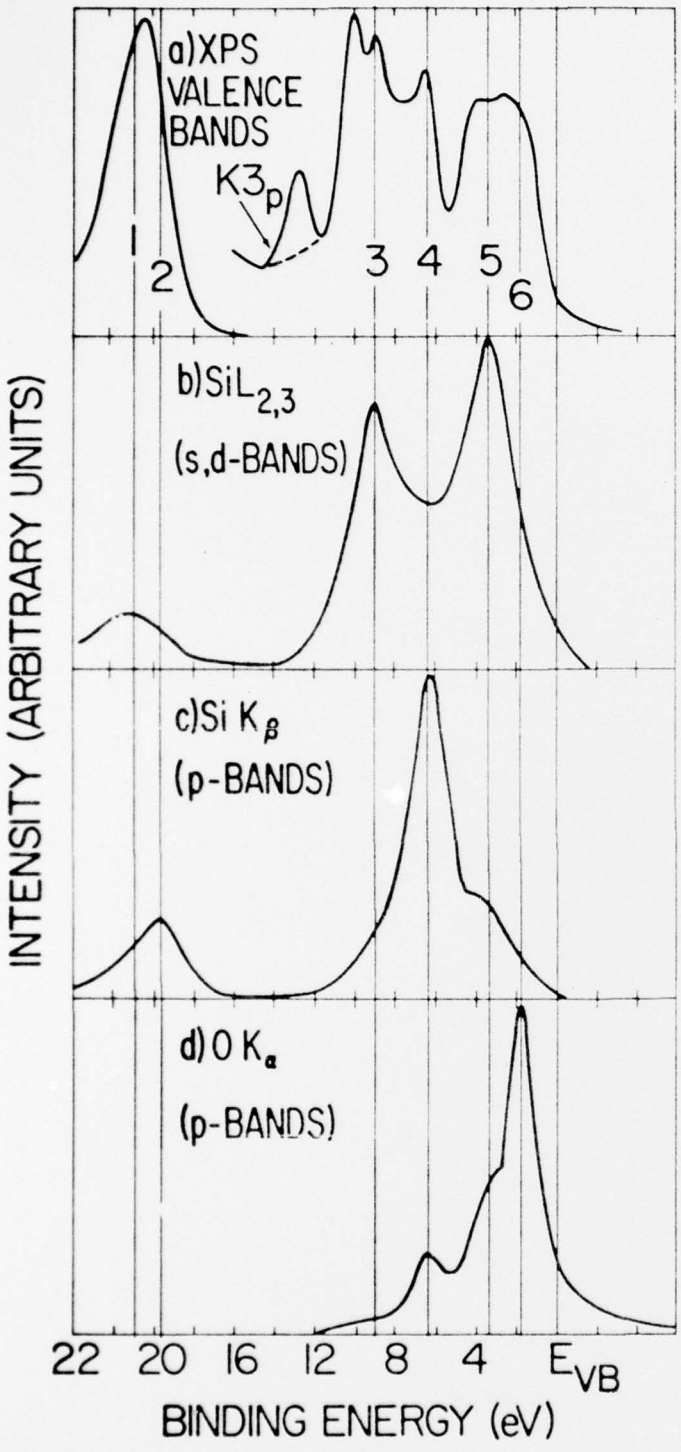

Figure 8 Comparison of the XPS spectrum of α-quartz with X-ray emission spectra from the literature.

(a). α-quartz X-ray photoemission spectrum,

(b). Weich's Si $L_{2,3}$ spectrum,[15]

(c). Lauger's Si Kβ spectrum,[16]

(d). Klein and Chun's O Kα spectrum.[14]

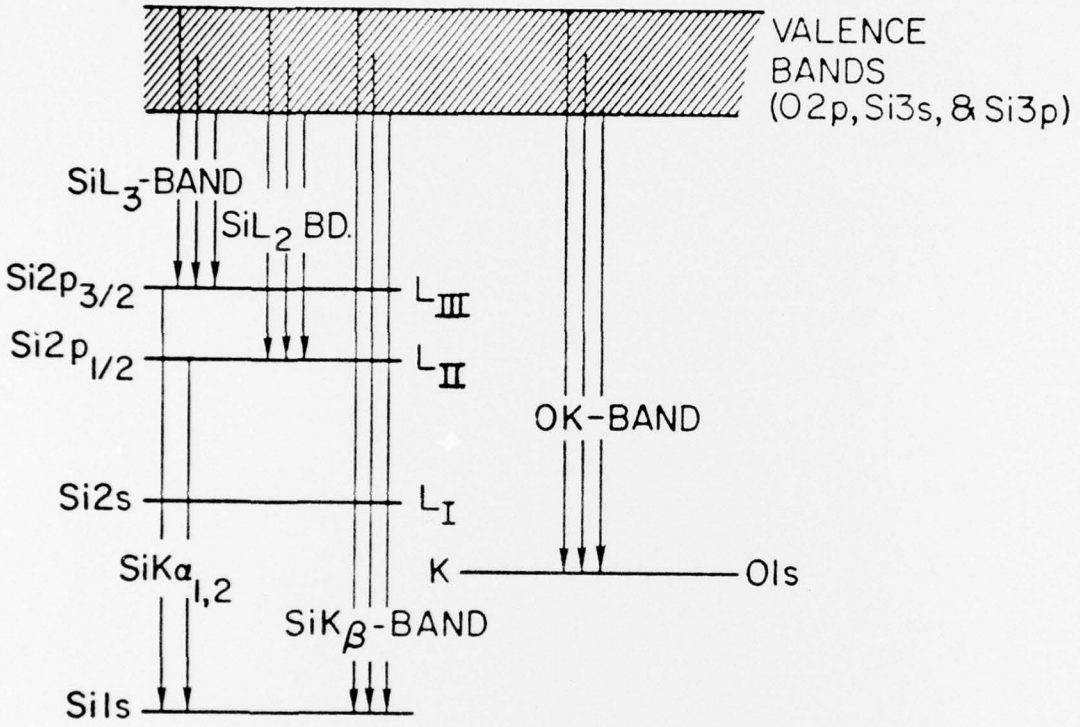

Figure 9 Schematic energy level diagram of SiO_2 showing relevant X-ray emission transitions.

METRIC SYSTEM

BASE UNITS:

Quantity	Unit	SI Symbol	Formula
length	metre	m	...
mass	kilogram	kg	...
time	second	s	...
electric current	ampere	A	...
thermodynamic temperature	kelvin	K	...
amount of substance	mole	mol	...
luminous intensity	candela	cd	...

SUPPLEMENTARY UNITS:

plane angle	radian	rad	...
solid angle	steradian	sr	...

DERIVED UNITS:

Acceleration	metre per second squared	...	m/s
activity (of a radioactive source)	disintegration per second	...	(disintegration)/s
angular acceleration	radian per second squared	...	rad/s
angular velocity	radian per second	...	rad/s
area	square metre	...	m
density	kilogram per cubic metre	...	kg/m
electric capacitance	farad	F	A-s/V
electrical conductance	siemens	S	A/V
electric field strength	volt per metre	...	V/m
electric inductance	henry	H	V-s/A
electric potential difference	volt	V	W/A
electric resistance	ohm		V/A
electromotive force	volt	V	W/A
energy	joule	J	N-m
entropy	joule per kelvin	...	J/K
force	newton	N	kg-m/s
frequency	hertz	Hz	(cycle)/s
illuminance	lux	lx	lm/m
luminance	candela per square metre	...	cd/m
luminous flux	lumen	lm	cd-sr
magnetic field strength	ampere per metre	...	A/m
magnetic flux	weber	Wb	V-s
magnetic flux density	tesla	T	Wb/m
magnetomotive force	ampere	A	...
power	watt	W	J/s
pressure	pascal	Pa	N/m
quantity of electricity	coulomb	C	A-s
quantity of heat	joule	J	N-m
radiant intensity	watt per steradian	...	W/sr
specific heat	joule per kilogram-kelvin	...	J/kg-K
stress	pascal	Pa	N/m
thermal conductivity	watt per metre-kelvin	...	W/m-K
velocity	metre per second	...	m/s
viscosity, dynamic	pascal-second	...	Pa-s
viscosity, kinematic	square metre per second	...	m/s
voltage	volt	V	W/A
volume	cubic metre	...	m
wavenumber	reciprocal metre	...	(wave)/m
work	joule	J	N-m

SI PREFIXES:

Multiplication Factors	Prefix	SI Symbol
1 000 000 000 000 = 10^{12}	tera	T
1 000 000 000 = 10^{9}	giga	G
1 000 000 = 10^{6}	mega	M
1 000 = 10^{3}	kilo	k
100 = 10^{2}	hecto*	h
10 = 10^{1}	deka*	da
0.1 = 10^{-1}	deci*	d
0.01 = 10^{-2}	centi*	c
0.001 = 10^{-3}	milli	m
0.000 001 = 10^{-6}	micro	μ
0.000 000 001 = 10^{-9}	nano	n
0.000 000 000 001 = 10^{-12}	pico	p
0.000 000 000 000 001 = 10^{-15}	femto	f
0.000 000 000 000 000 001 = 10^{-18}	atto	a

* To be avoided where possible

MISSION
of
Rome Air Development Center

RADC plans and conducts research, exploratory and advanced development programs in command, control, and communications (C^3) activities, and in the C^3 areas of information sciences and intelligence. The principal technical mission areas are communications, electromagnetic guidance and control, surveillance of ground and aerospace objects, intelligence data collection and handling, information system technology, ionospheric propagation, solid state sciences, microwave physics and electronic reliability, maintainability and compatibility.

Printed by
United States Air Force
Hanscom AFB, Mass. 01731